Universidade de São Paulo
Instituto de Astronomia, Geofísica e Ciências Atmosféricas
Departamento de Astronomia

Lívia Silva Rocha

The masses of Neutron Stars

São Paulo
2023

Lívia Silva Rocha

The masses of Neutron Stars

Thesis presented to the Departament of Astronomy of the Instituto de Astronomia, Geofísica e Ciências Atmosféricas from São Paulo University to get the title of PhD in Science.

Corrected version. The original is available at the Unit.

Concentration area: Astronomy

Advisor: Prof. Dr. Jorge Ernesto Horvath

São Paulo

2023

To my grandparents - in memoriam

Acknowledgements

Firstly, I thank my family who has always been my greatest influencer and never spared efforts to support me. To my parents Manoel and Lêda, who have always welcomed me and provided me with the necessary support so that I could pursue my paths, whether in graduate school or in personal life. To my siblings Leandro and Camila, for being my companions and cheering for my achievements. You are my safe haven.

To my advisor Jorge Horvath, for welcoming me since 2015 when I was still an undergraduate student and guiding me on this professional journey. Without your guidance and the necessary scoldings, I would not be able to write and present this Thesis.

To my boyfriend Maurício Usatai, who has always supported me since the moment we met and especially in the months leading up to the defense, where anxiety exacerbates. To you who have shown yourself to be a great life partner, willing to conquer the world by my side. We are better together.

To the colleagues of Gardel group: Antônio, Lucas de Sá, Lucas Barão, Riis Rhavia, Pedro Moraes, and Marcio de Avellar for all the enriching discussions over the last few years and also for the good times we spent together, whether at IAG or outside of it.

To the colleagues and friends Jullian, Larissa, Heitor, Christiano, Pedro, Lory, Stella, Catarina and Gê with whom I had the pleasure of living with over these years attending IAG and who were important figures in making workdays less tedious, in addition to providing me with diverse discussions, whether deep or not.

To the Max Planck Institute for Radio Astronomy, and especially to Dr. Paulo Freire, for welcoming me for a period of 6 months in my last year of PhD. This was certainly the most enriching experience I had in my brief academic career, which is actually just beginning. I will never forget the friendly and welcoming environment that I found in this

institute.

To the friends that I had the opportunity to make during the period I was in Germany, whose names I will not mention because the list is long. Know that each of you has a space in my memory and heart, and that you made my days in Bonn much more special.

To my longtime friends who are always by my side.

To the CAPES agency for the financial support provided in the form of a regular scholarship, as well as through the partnership with DAAD in Germany, with which I was able to carry out an internship at MPIfR in Bonn.

To IAG and USP for providing the necessary structure for us graduate students to perform our work.

"*There are in fact two things, science and opinion: the former begets knowldge, the latter ignorance*"

Hippocrates

"*The truth does not change because it is or is not believed by most people*"

Giordano Bruno

Resumo

Após quase 60 anos desde a descoberta do primeiro pulsar, a física das Estrelas de Nêutrons (ENs) ainda apresenta questões não respondidas que podem dar início a uma nova era na Ciência. Sendo as estrelas mais densas e pequenas observadas no Universo, com densidades médias acima da densidade de saturação nuclear ($\rho_{sat} = 2.8 \times 10^{14}$ g/cm^3), a reprodução de sua matéria em laboratórios terrestres se torna extremamente difícil.

A amostra de ENs com massas medidas vem crescendo graças aos avanços tecnológicos e observacionais. A medição de propriedades macroscópicas destes objetos permite traçar suas origens e entender como são formados. As massas observadas nos Ãºltimos anos colocaram à prova a existência de um valor canônico impresso no nascimento. O intervalo de massas, bem maior do que antes era considerado possível, evidencia a existência de diferentes caminhos evolutivos. Além disso, a observação de ENs extremamente massivas, como o PSR J0952-0607 com $m = 2.35 \pm 0.17\ M_\odot$ entre outros que iremos comentar ao longo desta Tese, também tem testado o problema da massa máxima prevista pela Relatividade Geral (RG) combinada com a teoria da matéria supranuclear.

Esta Tese tem como objetivo principal aplicar métodos computacionais de análise bayesiana à distribuição de massa das ENs para realizar inferências sobre a sua forma e o comportamento na região de altas massas. Em concordância com trabalhos anteriores, encontramos que a distribuição apresenta um caráter bimodal que se reflete na existência de ao menos duas populações de ENs distintas. No entanto, contrário a resultados prévios, mostramos que estes objetos podem atingir massas tão altas quanto 2.6 $M_\odot$, dando suporte para classificar a componente menos massiva do evento GW190814, com massa $m = 2.59^{+0.08}_{-0.09}\ M_\odot$, como uma EN.

Dado o cenário promissor das deteções de ondas gravitacionais (OGs), que pode auxi-

liar na resolução de diversos problemas relacionados à física das ENs, parte desta Tese foi dedicada à criação de um catálogo online de sistemas duplos de estrelas de nêutrons (eventuais fontes de OGs quando coalescerem), com o intuito de estudar como estes sistemas são formados, o que distingue os sistemas que vão coalescer daqueles que não irão, pelo menos no tempo de Hubble, e quais as "marcas" desta coalescencia podem ser traduzidas em grandezas observáveis.

Por último, visando contribuir para o problema da natureza da matéria encontrada no interior destas estrelas, esta Tese também apresenta um modelo de equação de estado (EE) baseado na "hipótese da matéria estranha" para descrever a composição interna de ENs através de um gás de quarks no estado conhecido como *color-flavor-locking* (CFL). Os resultados obtidos dão suporte à existência de ENs extremamente massivas, em concordância com os resultados estatísticos sobre a amostra inferidos a partir da amostra observada.

Abstract

After almost 60 years since the discovery of the first pulsar, the physics of Neutron Stars (NSs) still present unanswered questions that could lead to a new era in Science. Being the densest and smallest stars observed in the Universe, with average densities above the nuclear saturation density ($\rho_{sat} = 2.8 \times 10^{14}$ g/cm^3), reproducing their matter in terrestrial laboratories is an extremely difficult challenge.

The sample of NSs with measured masses is growing thanks to technological and observational advances. The measurement of macroscopic properties of these objects allows us to trace their origins and understand how they are formed. The observed masses reverted the idea of the existence of a canonical value imprinted at birth. The range of masses, much larger than what was previously considered possible, indicates the existence of different evolutionary paths and histories leading to the formation of NSs. In addition, the observation of extremely massive NSs, such as PSR J0952-0607 ($m = 2.35 \pm 0.17\ M_\odot$) and many other we will comment through this Thesis, has also raised the problem of the maximum mass predicted by General Relativity (GR) combined with a theory of supranuclear matter.

The main objective of this Thesis is to study the mass distribution of NSs applying computational methods of Bayesian analysis to make inferences about its shape and the behavior at the high-mass region. In agreement with previous work, we find that the distribution has a bimodal character, that reflects the existence of at least two different populations of NSs. However, contrary to previous results, we show that these objects can reach masses as high as 2.6 $M_\odot$, supporting, for instance, the classification of the less massive component of the GW190814 event, with a mass $m = 2.59^{+0.08}_{-0.09}\ M_\odot$, as a NS.

Given the promising scenario of gravitational wave (GW) detection, that can help

solving several problems related to the physics of NSs, part of this Thesis was dedicated to create an online catalog of neutron star binary systems (potential sources of GWs when they coalesce), with the aim of studying how these systems are formed, what distinguish those systems that will coalesce from those that will not, at least on a Hubble time, and which are the "fingerprints" from these coalescence that can be translated into observable quantities.

Finally, in order to contribute to the problem of the nature of matter found in the interior of these stars, this Thesis also presents an equation of state (EOS) model based on the "strange matter hypothesis" to describe the internal composition of NSs through a gas of quarks in the state known as *color-flavor-locking* (CFL). The results obtained support the existence of extremely massive NSs, in agreement with statistical results directly inferred from the observed sample.

List of Figures

List of Tables

Contents

Chapter 1

Introduction

The physics of Neutron Stars (NSs) is one of the most challenging topics of high energy physics under debate in the current century. The extreme conditions found inside these objects are, until now, impossible to be achieved in laboratories and explains why, after almost a century of the first studies about the subject and more then 60 years after the first observation, the picture stills incomplete. Improvements in the understanding of matter at ultrahigh densities can change the way we understand the Universe and provide a new era in Science.

Interdisciplinary efforts are necessary to understand how and in which conditions these Compact Stars are formed, how is the formation imprinted in their observational properties, how they continue to evolve and all related phenomena, like the physics of supernovae (SNe), chemical enrichment of interstellar medium, gamma-ray bursts, gravitational wave emissions and many others. Observations of such phenomenons helps to set reliable constraints in theoretical physics describing these extreme objects, as well as in their main properties, like masses and radii.

For a long time, mass measurements of NSs seemed to corroborate with the paradigm of an unique formation scenario through the core collapse supernova (CCSN) of an iron (^{56}Fe) core, marking the end of life of a progenitor star with mass above $\sim 8\ M_{\odot}$. Technological and observational improvements allowed us to break with this idea and expand the window of possibilities for NS formation, a reflect of the broader range of masses detected nowadays, between $1.17 - 2.74\ M_{\odot}$. Despite of an electron capture supernova (ECSN) of a degenerate *OMgNe* core, they can also be formed from an Accretion Induced Collapse (AIC) of a white dwarf (WD) approaching its maximum mass, or the double degenerate AIC from the merger of two WDs.

General relativity (GR) predicts the existence of an upper threshold for NS masses, but the exact value still cause discussions between astrophysicists. Although a theoretical limit of 3.2 $M_\odot$ was found by Rhoades Jr and Ruffini (1974), astronomers defended over many years that the true maximum could not be beyond 2 $M_\odot$, for evolutionary reasons. The discovery of the true limit is important to distinguish between NSs and black holes (BHs), since every object exceding it will collapse into a BH. Furthermore, it also plays a key role in setting reliable constraints to the validity of equation of state (EoS) models. More then 10 years past since the first measurements contradicting a maximum mass below two solar masses appeared (Demorest et al., 2010) . The latest measurement reveals a NS in a *black-widow system* with $m = 2.35 \pm 0.17$ $M_\odot$ (Romani et al., 2022), the largest well-measured mass to date. A few other systems are also indicated to have even larger masses, as we will discuss later, but they are subject to larger uncertainties.

Furthermore, the recent detection of gravitational waves (GW) with the LIGO/Virgo interferometers opened up a new era in Astronomy. It raised the possibility of combining and comparing electromagnetic observations with a new source of information, the GWs, to constrain the EoS of matter at densities above twice the nuclear saturation density. This new advance placed the Double Neutron Star (DNS) systems in a privileged stage, and triggered the interest to understand how the systems with two NSs that will merge within the Hubble time are formed. The event GW190814 was identified as originated from the merger of a BH with $m_1 = 23$ $M_\odot$ and a companion, yet unidentified, with $m_2 = 2.60$ $M_\odot$ (Abbott et al., 2020). An analysis implemented by the LIGO team placed this event as an outlier of the merging binary black hole (BBH) population (Abbott et al., 2021). If confirmed to be a NS, this discovery can help to determine the maximum mass they can achieve.

The threshold for NS masses is intimately related with the equation of state governing the matter inside the star, and is predicted by the equation of hydrostatic equilibrium under GR theory. A vast number of models are proposed to describe the EoS inside NSs, subject to the scrutiny of observational data like masses, radii and tidal deformabilities. A deeply discussed model is based on the *strange matter hypothesis*, under which a matter made of up, down and strange quarks is believed to be more stable than nuclear matter. This model is shown to allow the existence of heavier stars in comparison with nuclear matter, easily accommodating masses compatible with the one observed from gravitational waves.

This Thesis has the purpose of discussing the problems we mentioned before associated with NS physics, and is structured in the following way. In Chapter 1 we start with a historical overview of the development of Science which corroborated with the discovery and characterization of NSs, and introduce some of the main topics necessary to understand their nature. In Chapter 2 we focus on the statistical analysis of the mass distribution of observed NSs, comparing our results with previous works and arguing in favor of the existence of ultra-massive NSs. In Chapter 3 we introduce the standard scenario for DNS formation and the catalogue created to help boost the study about these systems. Chapter 4 presents the exact solutions we found for the Einstein Field Equations (EFE) describing a strange matter in the CFL phase. Finally, in Chapter 5 we present a summary and main conclusions of our work.

Chapter 2

Neutron star physics and some of its problems

2.1 From celestial spheres to compact stars

The mysteries of the Universe have fascinated humanity since prehistoric times. Although it is difficult to determine the exact date of the earliest astronomical records of humanity, it is possible that the cave paintings of Lascaux, dating back over 17.000 years and depicting various animals and abstract forms, are actually connected to star constellations visible in the Paleolithic sky. This suggests that these paintings not only depict animals and abstract shapes but also serve as visual markers for the passage of time and even significant celestial events such as comet passages (Sweatman, 2017). At that time, stars allowed civilizations to orient themselves on their journeys, mark the passage of time, and make predictions about the best time for planting and harvesting.

Babylonians, Egyptians, Greeks, and Mayans imbued stars with divine attributes, associating them with gods, heroes and cosmic forces. These mythologies provided cultural narratives, guiding celestial observations and shaping early cosmological frameworks. It was only in anciente Greece that our modern scientific view of the cosmos started, when Greek philosophers started looking for a fundamental relationship between numbers and nature, instead of attributing natural phenomena to deities. (Carroll and Ostlie, 2017). At that time, many models emerged to describe the cosmos, and one of the first was that of Anaximander (610 - 546 BCE), who was also the first philosopher known to wonder about the nature of stars. The Earth was believed to be the center of the Universe and, according to Anaximander's model, the cosmos was enclosed in a celestial sphere, and the stars were nothing more than holes in this dome through which it was possible to see a "universal flame" (Paulucci et al., 2022).

Eudoxus of Cnidus (408 - 355 BCE) constructed a planetary model, under request of Plato, in which the distance to the celestial sphere was believed to be comparable with the distance to the Sun, considered a planet at that time. Aristotle (384 - 322 BCE) later proposed that stars are composed of a *quintessence* and therefore would not be subject to physical laws. Aristarchus of Samos (310 - 230 BCE) was the first philosopher forward-thinking. He believed that was the Earth that revolved around the Sun, not the contrary, and found a good estimate for the distance to the Sun and its radii. The absence of annual parallaxes in heliocentric models required the distance to the celestial sphere to be orders of magnitude higher than was believed to be possible. His ideas did not find support. With the calculus of Earth's circumference made by Eratosthenes (276 - 194 BCE), Ptolemy (100 - 170 CE) defined the distance until the celestial sphere to be around 2000 times the distance to the Sun, a scale that was maintained until the Renascence.

The Greek astronomer and mathematician Hipparchus (190 - 120 BCE) made groundbreaking advancements in the study of stars. He developed a catalog of stars, known as the "Hipparchus Catalog", which listed the positions and brightness of around 850 stars. Hipparchus also devised a magnitude system to classify stars based on their brightness and distance, with first-magnitude stars being the brightest and closest.

The Islamic Golden Age, spanning from the 8th to the 14th centuries, saw significant progress in astronomy and the understanding of stars. Muslim astronomers built upon the knowledge of earlier civilizations, including the Greeks and Babylonians. Astronomers such as Al-Battani (858 - 929 CE) and Al-Farghani (800 - 870 CE) made important contributions, accurately measuring the positions of stars and describing their motions.

During the Renaissance in Europe, between the 14th and 17th centuries, the study of stars became more refined and detailed. Nicolaus Copernicus (1473 - 1543) proposed the heliocentric model of the solar system, which placed the Sun at the center and explained the apparent motion of stars. His work laid the foundation for further advancements in astronomy. Names as Tycho Brahe (1546 - 1601) , who observed a supernova in 1572, and Johannes Kepler (1571 - 1630) also contributed to the field. The invention of the telescope in the early 17th century revolutionized the study of stars. Galileo Galilei (1564-1642) used the the instrument to observe celestial bodies, including stars, planets, and the Moon. His observations challenged the prevailing understanding of the heavens and provided evidence to support the heliocentric model.

In 1814, Fraunhofer (1787 - 1826) invented a modern spectroscope that allowed him to discover dark lines in the solar spectrum, now recognized as absorption lines. At that time distance determinations were one of the biggest problems in astronomy. The concept of parallax, the apparent shift in the position of a star due to the Earth's orbit around the Sun, was proposed as a method to calculate stellar distances. Friedrich Bessel (1784 - 1846) successfully measured the parallax of the star 61 Cygni in 1838, marking the first direct measurement of a star's distance. The result was a factor hundreds of times greater than predicted by the Ptolemaic model, revealing an immense universe to be explored.

In the 19th and 20th centuries, advancements in technology and the development of astrophysics propelled our understanding of stars to new heights. Scientists, such as William Herschel (1738-1822), discovered new stars and began classifying them based on their spectral characteristics. Henrietta Swan Leavitt (1868 - 1921) made important contributions by discovering the relationship between the brightness and period of pulsating stars, which later allowed astronomers to measure astronomical distances. Cecilia Payne-Gaposchkin (1900 - 1979) and Hans Bethe (1906 - 2005) played pivotal roles in determining that stars, including the Sun, are primarily composed of hydrogen and helium. Spectroscopy, the study of electromagnetic radiation emitted or absorbed by matter, provided detailed information about the chemical elements present in stars. Scientists could then discover that stars have a wide range of compositions, with varying amounts of elements beyond hydrogen and helium, such as carbon, nitrogen, oxygen, and iron.

E. Hertzsprung (1873 - 1967) and H. N. Russell created independently (1877 - 1957), in 1911 and 1913, what is now called the *Hertzsprung-Russell diagram*, which relates the luminosity and temperature of stars (Figure 2.1). They observed that stars were not all the same and proposed that they undergo different evolutionary stages, which were later clarified. This diagram allowed for a better classification and understanding of the physical characteristics of stars, providing insights into their internal structure.

In 1911, in parallel with astronomical developments, Rutherford discovered the existence of the atomic nucleus, which he named *proton*. Around 1925, physicists had already postulated the existence of spin, and this discovery led Wolfgang Pauli, in the same year, to enunciate his *exclusion principle* which states that no two fermions can occupy the same quantum state simultaneously. At the same time, Einstein was generalizing the Bose distribution for the case of a fixed number of particles. Pauli's theory triggered, in 1926,

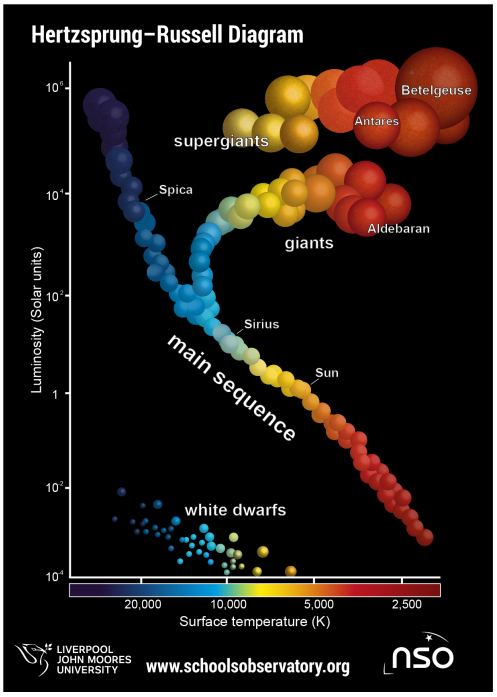

Figure 2.1: The Hertzsprung-Russel diagram shows the relation between luminosity and temperature of stars. Its construction helped to better classify stars and comprehend their evolution.

the development of a quantum statistics that could be applied to a set of identical particles obeying the mentioned principle (Bonolis, 2017). This theory was independently developed by Enrico Fermi and Paul Dirac, and for this reason it is named as *Fermi-Dirac statistics*, which Pauli demonstrated to be the correct treatment to describe a gas of degenerate electrons.

Previously, in 1844, Bessel had already concluded that the star Sirius should have a "dark companion", observed for the first time in 1862 by Alvan Graham Clark (Welther, 1987). The theoretical development and technological advancements led to classify the companion of Sirius as a *white dwarf* (WD), a hot and extremely dense object compared to other known stars. It took a long time until Fowler (1926) was able to explain the physics of WD's, applying the problem to the formulation of quantum statistical mechanics. As Eddington wrote: "The white dwarfs appeared to be a happy hunting ground for the most revolutionary developments of theoretical physics"(Eddington, 1927). It was only the beginning of the development of studies about compact stars.

2.2 Electron degeneracy pressure

The life of a "normal" star, like our Sun, is based on thermonuclear reactions which provides thermal pressure to balance the stellar structure against a gravitational collapse. The reactions starts with proton-proton reactions where hydrogen is burned into helium. This process increases the temperature and density at the center of the star, which is around 160 times larger than the surface density, as illustrated in Figure 2.2. The central density is initially of 10^3 g cm^{-3}, and increases as long as the fuel is burned. The Schönberg-Chandrasekhar establishes a limit for the mass of an isothermic helium core to maintain the hydrostatic equilibrium. When this limit is achieved, the core contracts increasing even more the central density. As a consequence, electrons enters in a *quantum regime* since the inter-nucleus distance reduces to the order of electronic orbitals. The *Pauli exclusion principle* take action ensuring that each quantum state is occupied by only one electron.

In a simplistic way, the treatment employed by Fowler is as follows. Lets consider a sphere with N electron confined in a volume V. The "available" space for each particle is $\Delta x \sim \left(\frac{V}{N}\right)^{1/3}$. If we assume the electrons enters in a quantum regime, they need to obey the Uncertainty Principle, with $\Delta x \Delta p \geq \hbar$. Consequently:

$$\Delta p \gtrsim \frac{\hbar N^{1/3}}{V^{1/3}}. \tag{2.1}$$

In a non-relativistic domain, the average kinetic energy is:

$$\langle E_k \rangle = \frac{\Delta p^2}{2m} \sim \frac{\hbar^2 N^{2/3}}{V^{2/3} m} \tag{2.2}$$

The internal energy of the sphere is $U = N \langle E_k \rangle$. Under thermodynamics, the pressure inside the system, for a constant entropy, can be obtained by:

$$P_e = -\frac{\partial U}{\partial V}|_{S=cte} \sim k \frac{\hbar^2 N^{5/3}}{V^{5/3} m} \sim k n^{5/3}. \tag{2.3}$$

In terms of density, $\rho = nm$, the Equation 2.3 gives us the equation of state (EoS) for a non-relativistic degenerate gas of electrons, $P = K\rho^{5/3}$. An equation of state describes the state of matter under specific conditions. In the relativistic domain, $\langle E_k \rangle = pc$, and the EoS $P_e = K\rho^{4/3}$. The most important is to note that now, the temperature of the star has no influence on the pressure. It is only the electron degeneracy pressure which opposes the gravity. Furthermore, the proportionality to $\hbar^2$ unveil that the existence of compact stars is completely dependent on Quantum Mechanics.

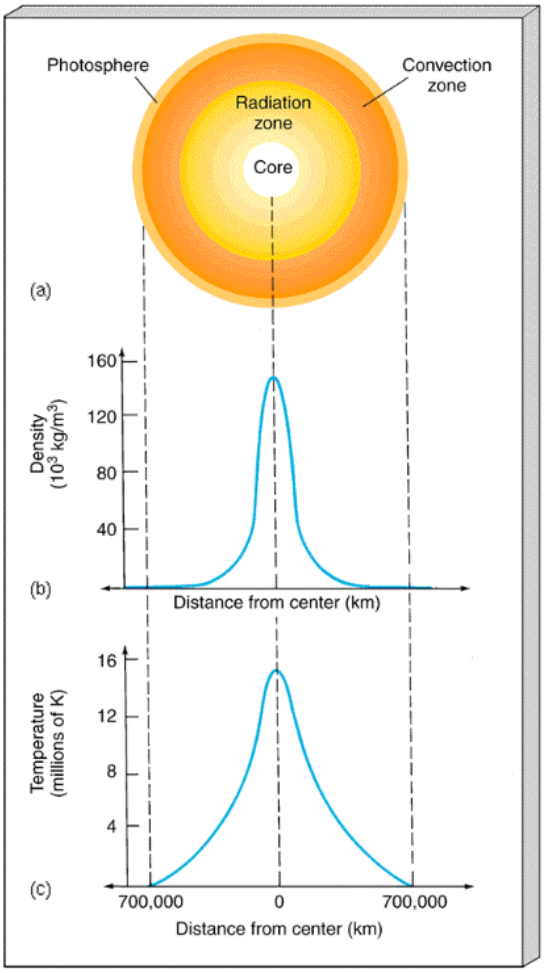

Figure 2.2: Theoretical model of density profile and temperature inside the Sun. Central density is around 160 times larger the surface density. (Extracted from Chaisson et al. (2005))

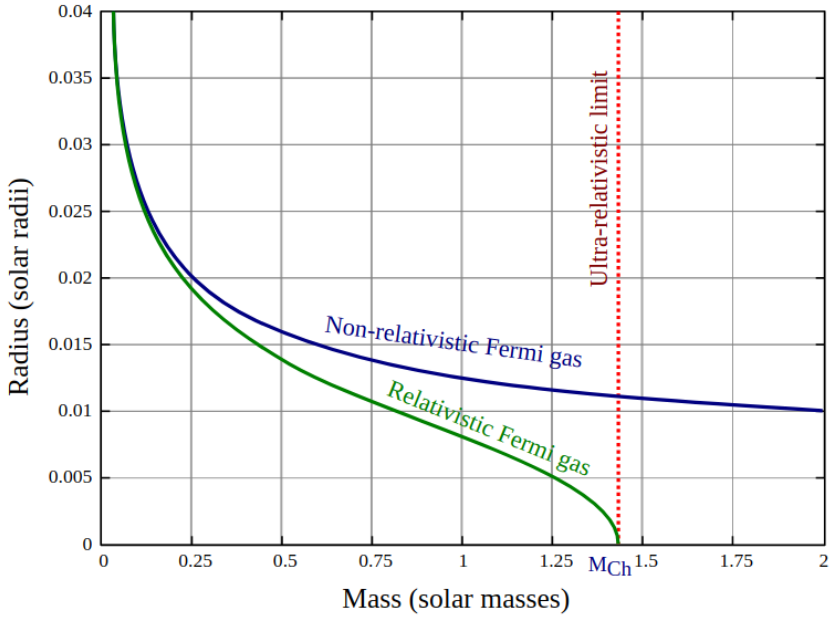

Figure 2.3: Mass-radius relation for a Fermi gas. The blue curve is the solution for non-relativistic electrons, while the green curve is the solution for a relativistic gas. The dotted red line marks the Chandrasekhar mass limit, above which the structure collapses.

Figure 2.3 shows the mass-radius relation constructed from solutions of hydrostatic equilibrium for a gas of degenerate electrons. The blue curve is the solution for a non-relativistic gas, and can describe the structure until $\sim 0.5\ M_\odot$. Above this value the density is high enough for electrons to become relativistic (green curve). The dotted red line represents the *Chandrasekhar* limit, above which the structure collapses, and represents the mass limit for White Dwarfs, about $\sim 1.4\ M_\odot$.

The degenerate electrons become fully relativistic at $\sim 10^7$ g cm^{-3}. For densities of this order of magnitude the *inverse β-decay*:

$$e^- + p \rightarrow n + \nu_e, \tag{2.4}$$

starts to take place. From this moment on, the abundance of neutrons in matter will begin to increase, but their contribution to the pressure is still very low.

2.3 Neutron Stars

2.3.1 Neutron degeneracy pressure

As the density increases, above $\sim 10^7$ g cm^{-3}, the neutron density also increases. From this point to the *neutron drip*, $\rho_{drip} = 4.3 \times 10^{11}$ g cm^{-3}, matter can be described by the

Baym-Pethick-Sutherland (BPS) equation of state, which we will not discuss in detail here. At the neutron drip density, it is favorable for neutrons to leak out from the nuclei, marking the beginning of the presence of a free neutron gas, such that they starts to contribute to the equation of state. The pressure of free neutrons become significant at $\rho > 10^{12}$ g cm^{-3}, and dominates for $\rho > 10^{13}$ g cm^{-3}. The Baym-Bethe-Pethick (BBP) equation of state describes matter at these densities, based on the liquid drop model described below.

Starting with a semi-empirical mass function for the nuclei, based on a liquid drop model of the type:

$$Mc^2 \equiv E = -\epsilon_0 A + \epsilon_S A^{2/3} + \epsilon_C Z^2 A^{-1/3}, \tag{2.5}$$

where Z is the atomic number, A the mass number. The nucleus is treated as a "little drop" of matter and its energy is assumed to be composed of a volume term (first term), a surface term (second term) and a Coulomb correction. The task is to adjust the expression to reproduce masses of known nuclei and then obtain the coefficients $\epsilon_0, \epsilon_S, \epsilon_C$. The EoS is obtained by minimizing with respect to A and Z, and imposing chemical and mechanical equilibrium between the gas of neutrons and the nuclei. Consequently, it is possible to write the total energy density (ϵ) as a function of the baryon density, n_B, only, from where the total pressure results:

$$P = n_B^2 \frac{\partial}{\partial n_B}\left(\frac{\epsilon}{n_B}\right) = P_n + P_e + P_L, \tag{2.6}$$

where P_n is the pressure component for neutrons, P_e for electrons and P_L for the lattice.

The above EoS is valid until the nuclear saturation density is reached, $\rho_{sat} = 2.8 \times 10^{14}$ g cm^{-3}. At this point, the nuclei begin to dissolve and merge together, and matter is now composed in a first approximation of fluids of neutrons, protons and electrons. Below this state no stable configuration is found to describe a compact object. Is about the saturation point that neutrons will begin to become degenerate and provide balance to a star. The treatment to derive the neutron degeneracy pressure follows exactly in the same way as we described for electrons at Sec. 2.2, with the difference that now is only the mass and fraction of neutrons that matters.

From the *Virial theorem*, a mass M of a classical gas in equilibrium, with a radius R, has an average temperature of:

$$\langle T \rangle \propto \frac{M}{R}, \tag{2.7}$$

so the temperature increases as R decreases. The average density of this Maxwell-Boltzmann gas is $\langle\rho\rangle \propto M/R^3$, so it increases even more rapidly than T.

The typical momentum difference between electrons in this gas is:

$$\Delta p_e \sim (6 m_e k \langle T \rangle)^{1/2} \propto \left(\frac{M}{R}\right)^{1/2}. \tag{2.8}$$

The typical separation between electrons is:

$$\Delta x_e \sim (n_e)^{-1/3} \propto \left(\frac{R^3}{M}\right)^{1/3}. \tag{2.9}$$

Finally, the volume occupied by an electron in phase space is:

$$(\Delta p_e \Delta x_e)^3 \sim 180 h^3 \left(\frac{M}{M_\odot}\right)^{1/2} \left(\frac{R}{R_\odot}\right)^{3/2}. \tag{2.10}$$

If a star of 1 $M_\odot$ contracts until $R \sim 3 \times 10^{-2}\ R_\odot$, the phase space volume will be $\sim h^3$. These mass and radii are characteristic of WDs. For NSs, with densities above ρ_{sat} and masses in the range of $1 - 3\ M_\odot$, the degeneracy pressure of neutrons will be responsible for establishing the equilibrium when the radii contracts to $10 - 12$ km.

2.3.1.1 Nucleon-nucleon interactions

The assumption of a free gas of neutrons lead to maximum masses at the order of $\sim 0.7\ M_\odot$. Above $\sim 3\rho_{sat}$ nucleon-nucleon interactions become important, but makes it difficult to determine the EoS. The potential has to be attractive for a small number of nucleons, and repulsive for a large number. One of the approaches was constructed by Bethe and Johnson (BJ), and provides a softer equation os state, with a repulsive potential for $\sim 10^{15}$ g cm^{-3}. This effect has a great impact in the stellar structure and provide support to higher masses.

The BJ approach generalizes the Yukawa potential in the form:

$$V_{BJ} = \sum_j C_j \frac{e^{-j\mu r}}{\mu r} + V_T, \tag{2.11}$$

where μ is related to the reciprocal of the mass of the particle exchanged between nucleons, r is the distance and V_T is a tensor interaction.

They considered the exchange of vector meson ω to be largely responsible for the repulsive core and contribute with a term $V_\omega = g_\omega^2 e^{-\mu_\omega r}/r$. Their EoS follows from:

$$\begin{aligned} &\frac{\epsilon}{n} \equiv W(k,0) + mc^2, \qquad && W(k,0) = 236 n^a MeV/particle, \\ &P = 364 n^{a+1} MeV/fm^3, \end{aligned} \tag{2.12}$$

with $a = 1.54$ and $1 \leq n \leq 3$ fm^{-3}. This EoS supports NSs with masses up to 1.9 $M_{\odot}$. As we will discuss specially in Chapter 5, there are equations of state which supports even higher masses.

2.3.2 A remarkable discovery

In 1054, Chinese astronomers registered a supernova (SN) explosion, the death of a star that could be as twice as massive as the Sun. Records says that it was so bright that it could be seen during day light for almost a month. The "guest star", as it was called at that time, remained visible in night sky for more than a year. Since then, only two other cataclysmic events of such magnitude where observed, one in 1572 by Tycho and another in 1604 by Kepler (Weber, 1999). It took hundreds of years to recognize the nature of such phenomena.

The neutrons were discovered by J. Chadwick in 1932, a few months after Lev. D. Landau hypothesized the existence of an ultra dense star behaving like a giant nucleus, although his work was just published after the discovery became public (Landau, 1932). In 1934, the existence of NSs was theorised by Baade and Zwicky (1934a,b,c), where they proposed that supernova explosions should be related with the transition of the core of a massive star to an extremely dense star, releasing an enormous amount of energy. Four years later, Landau proposed that even though the neutronic state of matter is usually endothermic and much less energetically favoured than the electronic state, a massive star can still generate conditions to from neutrons in stable reactions. Hence, it was proposed that the end product of a SN should be a cold, dense and compact NS mostly made of neutrons (Landau, 1938).

Given the extreme conditions presented in NSs and the impossibility to reproduce them in laboratory, as well as the lack of technologies able to detect such objects, the subject remained purely speculative until the discovery of the first *pulsar*, in 1967, by Jocelyn Bell (Hewish et al., 1968). At that time it was named as CP1919, but is now recognized as PSR B1919+21. The discovery intrigued the scientific community due to the small and extremely regular period of pulses. Several theories emerged, but Pacini (1967) and Gold (1968) were responsible to show that pulsars are nothing more then rapidly rotating and highly magnetized NSs. Efforts to identify more pulsars were intensified since then, and continues until today.

The pioneer work of Baade and Zwicky and the association of pulsars with supernova remnants, as the Crab pulsar, strengthen the association of NS births with explosions of massive stars. However, as we already mentioned, contributions from different channels also play a role in their birth mechanisms, as depicted in the mass distribution we will discuss through this Thesis.

2.3.3 The birth of Neutron Stars

Although a standard formation scenario emerged and strong evidence pointed to the birth of NSs from the supernova explosion of massive stars, as the association of pulsars with several supernova remnants (Tian and Leahy, 2004), alternative scenarios are also proposed and accumulate evidences in their favor (van den Heuvel, 2004). The old picture of $8 - 20\ M_{\odot}$ for progenitor stars collapsing to NSs is put in a jeopardy. For example, the CXOU J164710.2-455216 is a magnetar[1] found in the cluster Westerlund 1. This cluster has Main Sequence (MS) stars with masses of 40 $M_{\odot}$, a hint for NS formation from extremely high mass progenitors.

Binary interactions are proven to be of fundamental importance and responsible for changing the range of progenitor star masses forming NSs (Podsiadlowski et al., 2004; Iaconi et al., 2016), despite of the possibility of long accretion periods after the NS birth (Benvenuto et al., 2012). As a consequence, binary pulsars can experience different properties of those born isolated. Furthermore, accreting WDs in binary systems reaching their Chandrasekhar limit, as well as the merger of two WDs, can possibly form NSs (Dessart et al., 2006; Ruiter et al., 2019). In the following sections we discuss these alternative scenarios and comment on the current evidences.

2.3.3.1 Isolated stars

Isolated stars spend approximately 90% of their lifetime at the Main Sequence (MS) stage, transforming Hydrogen in Helium through the proton-proton chain reaction. A stable equilibrium between gravitational force pulling inwards and radiation and thermal pressure pushing outwards is what keeps them "alive". Although several ingredients can exert an influence on final configurations, initial masses at the Zero-Age MS (ZAMS) and

[1] Magnetars are a class of NSs with extremely high magnetic fields, $10 - 10^3$ times higher than for regular NSs.

the metallicity (Z) play a fundamental role to determine when will the cycle of thermonuclear reactions end, and how much will the stars survive. Massive stars, for example, will exert higher pressures on their cores, increasing the temperature and the rate of fusion reactions. Subsequently, they will spend less time at the MS stage.

Figure 2.4 depicts the broad-brush picture of single star evolution. Atop the axis, the numbers indicate the masses of the stars at the ZAMS which produce the features indicated below the axis. For solar metallicity, assumed to be $Z = 0.01$, stars above $\sim 7.5 M_{\odot}$ are the ones believed to be heavy enough to ignite carbon at their center. This threshold is referred as $M_{\rm up}$ (or alternatively $M_{\rm CO}$) in the literature. The minimum mass for the production of a neutron star after an explosive event is though to be slightly higher, at $M_n \sim 8 M_{\odot}$ but with a higher uncertainty denoted with a question mark ($M_{\rm EC}$ is an alternative name for this quantity, stemming from "electron capture"). Finally, above $M_{\rm mass} \geq 9 M_{\odot}$ or so, depending on metallicity and input physics, all possible nuclear reactions up to the iron are ignited [2] and we enter the regime of "true" massive stars, developing an iron core (note the alternative names $M_{\rm crit}$ and $M_{\rm ccsn}$ also found in the literature for the same quantity [Doherty et al., 2017]). When the silicon is exhausted the star loses the nuclear resources and the core starts to contract, becoming denser and hotter. The photons achieve sufficiently high energy and the *photodesintegration* process, $\gamma + {}^{56}Fe \rightarrow 13\,{}^{4}He + 4n$, takes place consuming energy of the star. The contraction is accelerated until electron captures become energetically favourable, and a *neutronization* process starts through the inverse beta decay reaction, $p + e^{-} \rightarrow n + \nu_e$. The electron degeneracy pressure inside the core can no longer sustain the star against the gravitational force, giving start to a *core-collapse supernova* (CCSN) at the same time as the neutron abundance increases and the proto-NS is balanced by the neutron degeneracy pressure. There are two main reasons that prevent us to precisely determine these thresholds: the uncertainties in the mass loss rate in advanced stages of the stellar evolution, and the true nature of convection inside the progenitors. As mentioned, the metallicity is important for the location of the boundaries, and as a general trend we know that the figures are lower for lower metallicities, and even so a substantial spread in the calculations still exist (Doherty et al., 2017), as we can see in Figures 2.5 and 2.6.

[2] The fusion of ${}^{56}Fe$ is an endothermic process and requires an enormous amount of energy. Thermonuclear reactions in the interior of stars cease at the iron peak.

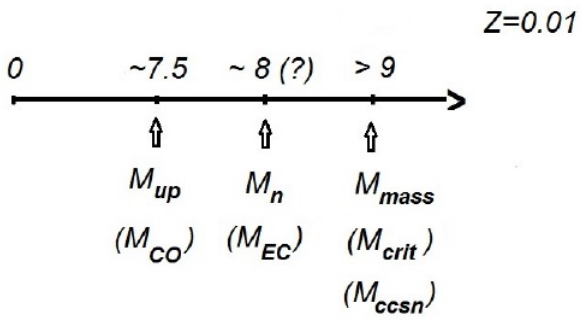

Figure 2.4: The boundaries of mass (ZAMS) separating the different regimes for solar metallicity. The numbers above the axis denote the approximate locations of the separation between regimes, with their names and alternatives indicated below. Extracted from Horvath et al. (2023).

While the actual problems above $M_{\rm mass}$ are mainly related to the collapse-implosion and launch of the supernova explosion, the fate of massive stars below $M_{\rm mass}$ presents a series of difficulties even before their final fate. The latest stage of these objects, characterized by the off-center ignition of degenerate carbon before the thermal pulses (TPs), is known as the "super-AGB" phase. Stars just below the $M_{\rm n}$ limit are thought to leave *ONeMg* WDs, and those slightly less massive a *CONe* WD, without any explosion. However, super-AGB stars have never been identified observationally with confidence, and indeed they do not stand out clearly from neighbours at nearby positions in the HR diagram. Consequently, we must rely on the accurateness of theoretical calculations for the determination of $M_{\rm up}$ and related quantities.

A second important mass scale starts at a value M_n, above which the cores may undergo electron captures and explode as a class of supernovae, forming NSs (Nomoto, 1984). The ignition of carbon leaves a strongly degenerate *ONeMg* core. The penetration of the surface convection zone into helium layer occurs during the carbon burning phase, dredging up the *He* layer and in a core growth through hydrogen-helium double-shell burning. As the mass inside the helium-burning shell increases, an electron capture onto *Mg* and *Ne* start and induce a rapid contraction of the core. The degeneracy pressure of electrons reduces, as the electron fraction per baryon Y_e is reduced, and the core explodes with a quite *fixed value* mass, $1.375 M_\odot$, in what is called an *electron-capture supernova* (ECSN). The explosion receives a massive contribution from the energy released by oxygen burning in nuclear statistical equilibrium, and therefore the event is actually close to a Type Ia thermonuclear event (a recent claim of the identification of an ECSN showing all the

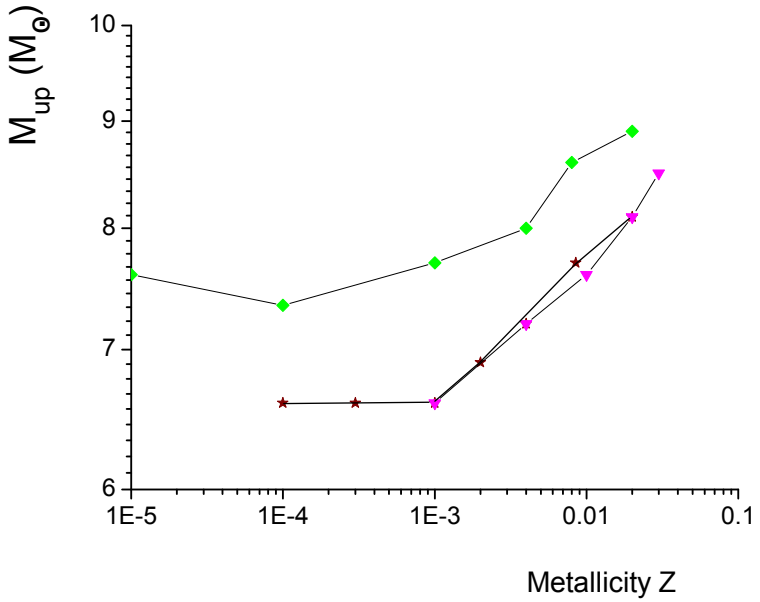

Figure 2.5: Sample calculations of the quantities M_{up} as a function of the metallicity Z. The three curves correspond to the calculations of Siess (2007) (diamonds, upper), Doherty et al. (2015) (stars, middle) and Suwa et al. (2018) (triangles, lower). Extracted from Horvath et al. (2023).

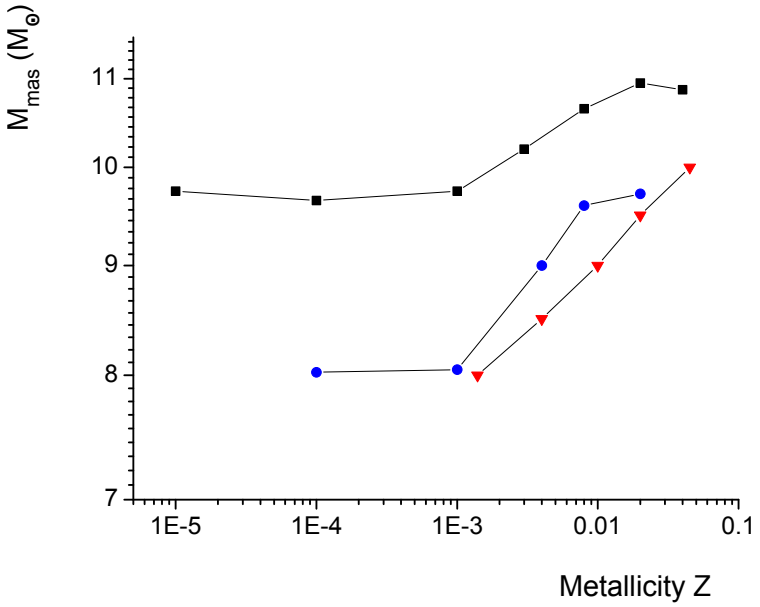

Figure 2.6: Sample calculations of the quantities M_{mass} as a function of the metallicity Z.The curves are due to Siess (2007) (squares, upper), Doherty et al. (2015) (dots, middle) and Eldridge and Tout (2004) (triangles, lower). Extracted from Horvath et al. (2023).

expected features has been presented [Hiramatsu et al.]). Because of these features, it is believed that an almost-fixed mass NS emerges, with $m \sim 1.25 M_\odot$ resulting from the emission of the binding energy of the fixed core. Since mass range in which this scenario occurs is the most abundant among the exploding progenitors, it is expected that they compose a large fraction of the full supernova rate, as it is easily seen from the form of the IMF function. A "light" group of NSs is expected to exist. The work in Schwab et al. (2010) found evidence to the presence of this group by analyzing the mass distribution of 14 well measured NSs (uncertainties below 0.025 $M_\odot$). All analysis considering the whole sample of NS masses found no evidence for the distinction between NSs formed from ECSNe and those formed from light iron cores. A large sample of NSs in this range is necessary to set firm conclusions (Rocha et al., 2019).

The discussion above implicitly requires that if even *lighter* ($< 1.25 M_\odot$) NSs exist, they must be formed in the explosion of small *iron* cores, not the ones undergoing the ECSNe. In other words, it is important to determine both the smallest neutron star mass and the lightest iron core resulting from the evolution of a $M \sim M_{mass}$ star. The lightest precisely measured NS mass up today is of PSR J1453+1559 companion, with $1.174 \pm 0.004 M_\odot$. Other sources, such as 4U1538-522 and Her X-1 may also be considered, but their error bars are larger and measurement methods must be refined, as we will comment further. With this figure for the gravitational mass M_G, the iron core progenitor of this low-mass neutron star should have been no heavier than $\sim 1.28 M_\odot$. Generally speaking, it is easier to find the baryonic masses of the remnants M_B than the gravitational mass M_G in the literature. The difference of both quantities, related to the binding energy, has to be calculated for each underlying theory of gravitation. However, a simple approximate expression for the latter quantity has been found by Lattimer and Prakash (2001) in terms of the quantity $\beta = GM_G/c^2 R_0$, where G is Newton's constant, c the speed of light and R_0 a fiducial radius (safely set to $12km$) to relate both quantities quite accurately:

$$\frac{M_B - M_G}{M_G} = 0.6 \frac{\beta}{1 - 0.5\beta} \tag{2.13}$$

and can be used quite safely if an extreme accuracy is not required.

The simulations of explosions of single stars have found confronting results for the minimum iron core forming the lightest neutron stars. For instance, Timmes et al. (1996) found a small number of progenitors that can produce a $M_G \leq 1.2 M_\odot$. A more recent work

by Sukhbold et al. (2016), calibrated for two progenitors, does not produce any neutron star below $M_G = 1.2M_\odot$. A dedicated study of the iron core at the onset of collapse (Suwa et al., 2018), formed by low-mass CO cores has obtained "light" neutron stars in the mass range of the observed sources, and even close to $\sim 1M_\odot$. This is consistent with the results of Ugliano et al. (2012), in which a minimum baryonic mass of $\sim 1.2M_\odot$ would render suitable gravitational mass after applying Eq. 2.13 (although for a quite narrow mass range of the progenitors). It is difficult to compare these and other works on the same subject, since they make use of different prescriptions for the stellar physics, different pre-supernova models and different numerical codes. In any case, it is entirely possible that a single star explosion does not constitute a valid evaluation for this lower limit, since the systems we mentioned are found in binaries and binary stellar evolution is likely important.

As we will see in Chapter 3, theoretical model explosions are not at odds with the observed mass distribution of NSs. All the simulations we cited are able to produce stellar remnants with masses around $1.8M_\odot$. However, they fall short of explaining the higher masses detected in actual systems ($> 2\ M_\odot$), as seen in Figure 2.7. Naively, one could have expected that the jump in the size of iron cores above $\sim 19M_\odot$ could be the reason behind production of heavy neutron stars, and even if this is true, the final values of the neutron stars M_G does not go above $1.9M_\odot$. The reason for these large iron cores, often overlooked in general works, is that there is a finite entropy inside them, making the "effective" Chandrasekhar mass $M_{\rm Ch,eff}$ to grow from its cold value $M_{\rm Ch,0}$ according to Timmes et al. (1996):

$$M_{\rm Ch,eff} \simeq M_{Ch,0}\left(1 + \left(\frac{s_e}{\pi Y_e}\right)^2\right) \tag{2.14}$$

where, inserting a rough average for the electronic entropy per baryon $\langle s_e \rangle = 1$ and given that $Y_e \geq 0.4$ in general, produces collapsing cores of $\sim 1.8M_\odot$. However, in spite of this growth, the iron cores never reach values well above $2M_\odot$, necessary to reproduce the highest observed neutron star masses. A contrasting view has been recently presented by Burrows and Vartanyan (2021), which in a summary of their present and former simulations were able to obtain not only explosions, but also gravitational masses up to $\sim 2M_\odot$ for remnant neutron stars. There is some important factor(s) not yet understood in the systematics of collapse simulations obtained by different groups to firmly assert whether

high masses above $\sim 2M_{\odot}$ can be produced by this formation channel at birth, or and/or subsequent accretion is needed to reach this mass range. This statement is also important for massive pulsars with $\geq 2M_{\odot}$, which have been suggested to be born "as is" (Deng et al., 2020), without suffering substantial accretion: if this happens to be true, current models of the explosions should obtain them.

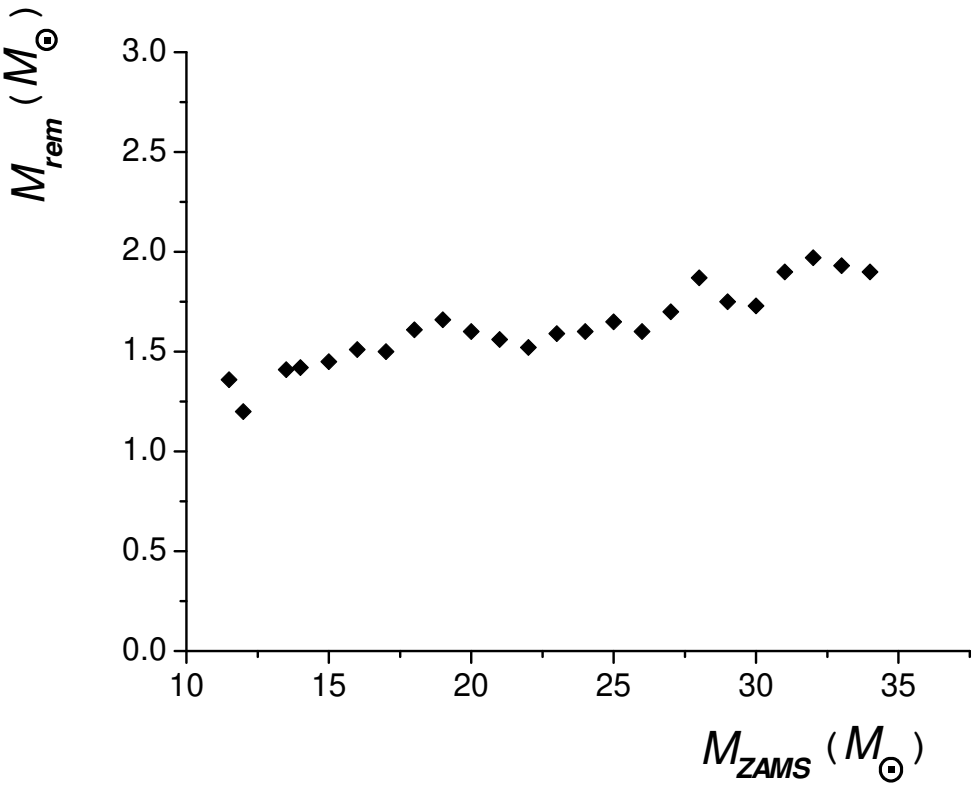

Figure 2.7: The compact remnants of single star explosions (baryonic mass) obtained by as a function of the ZAMS progenitor mass (Ugliano et al., 2012).

As a general trend we see that the simulations do well to reproduce a population of NSs with masses clustered around $1.35-1.4M_{\odot}$, and can populate a "second peak" around 1.8 $M_{\odot}$ as well. It is the high-mass tail definitely present in the distribution that does not match with simulations. In addition, the presence of a "low-mass" peak is quite interesting and worth mentioning. We have stated that, since light-mass ZAMS progenitors are very abundant, it is expected that the presence of a clustering at $\sim 1.25M_{\odot}$ can be easily seen. There are definitely a group of neutron stars in the histogram that were identified as such (Schwab et al., 2010), but they are often "merged" with the main "first peak" using statistical discriminators. In other words, even though their presence is possible, it has a low probability from this point of view (Horvath and Valentim, 2017). Moreover, it

is intriguing that, even *ignoring* the electron-capture events, a peak at that position has been obtained by Sukhbold et al. (2016). Therefore, we find somewhat counter-intuitive that the statistical significance of this group is not higher than the presently obtained one.

Finally, we would like to point out that a substantial advance in the knowledge of the connection between SN events and NS masses has a long road ahead. It is clear that the attack to this problem produced a lot of advances, and revealed an extreme complexity that is still being deciphered. One of the major issues, in our view, will be to establish whether the formation of NS and BH is monotonic (Burrows and Vartanyan, 2021) or "intermittent" (Sukhbold et al., 2016), and which are the conditions for that behavior.

2.3.3.2 Binary systems

Neutron stars are known to be present in a variety of systems. Some of them required quite sophisticated models for the evolution of a binary system featuring several phases along its life. Therefore, the question of a *binary* neutron star origin, in contrast with the isolated single-star evolution discussed above, arises.

The full evolution of stars in binary systems is not yet calculated until the *CO* core is formed. This means that the pre-supernova structure is not really known, but rather assumed using reasonable prescriptions. It is generally assumed that the whole consequence of binary interaction is to promptly remove the entire hydrogen envelope of the star at helium ignition (Ertl et al., 2020). The exact amount of accurateness of this simplification is not known, although it is a very reasonable first attempt and does not seem to imply any obvious misbehavior. An attempt to improve the situation can be seen in the work by Patton and Sukhbold (2020).

Works using some version of this simple "stripping" hypothesis have been presented, with exploding "helium star" masses ranging from ≥ 1 to $40 M_{\odot}$ since the removal of the envelope is a common feature of almost all close binary system evolution, the relation of the final iron core mass with the initial M_{ZAMS} is uncertain, because it depends on the mass loss rate, and even the specific code results need to be validated. Nevertheless, the neutron star distribution presents some features which are not present in the single-star explosions. For example, Woosley et al. (2020) obtain some objects that, because of larger fallback, lie above the $2 M_{\odot}$ mark for all the mass-loss prescriptions. Ertl et al. (2020) also obtain a small fraction of heavy objects. In both cases, the synthesis of a bimodal (or

even trimodal) population presented, as we will discuss in the next chapter, remains to be demonstrated in detail. The production of stars with $M_G \leq 1.2M_\odot$ does not appear to be favored in these simulations. However, the work of Fortin et al. (2016) claims to produce neutron stars as light as $\sim 1M_\odot$, although their framework is difficult to compare with the former.

Given that there are many systems in which the interaction of both components inevitably leads to consider the issue of the explosion(s) themselves, it is likely that substantial advances can be made in the near future, once the pre-collapse structure can be determined (Patton and Sukhbold, 2020). One prime example is the well-known path towards binary neutron stars (see, for example, Tauris et al., 2017; van den Heuvel, 2018) in which a detailed evolution implying "ultra-stripped" supernovae is needed. To connect with the issue of the NS distribution, we should state that even if the binary neutron stars that originated the "$1.4M_\odot$ paradigm" have not accreted substantially after formation, no real reason to expect a "fixed mass" exists. In fact, recent observations of *asymmetric* binary neutron star systems (Ferdman et al., 2020) that can merge on less than a Hubble time may call for a reanalysis of the masses at birth, in line with the simulation work just described. On the other hand, BH production with a supernova explosion has been also found possible, and in fact a recent report Maxted et al. (2020) claims one of these identifications.

2.3.3.3 Accretion-Induced Collapse

White dwarfs are subject to the Chandrasekhar limit. For binary systems with a massive WD, a high accretion rate ($\dot{M}$) from a MS or red giant companion can make the electron captures more efficient than the thermonuclear ignition of carbon or even oxygen, triggering the collapse of the star since the degenerate electron pressure is reduced (Nomoto and Kondo, 1991). This scenario, proposed more than 40 years agor, is known as the *Accretion-Induced Collapse* (AIC) and can be quite frequent in the universe, originating NSs in many binary systems.

The detection of a large number of low-mass binary pulsars in globular clusters was one of the features in which AIC was suggested to operate (Grindlay and Bailyn, 1988). AIC has been also invoked in the magnetar formation problem (Margalit et al., 2019), expecting a flux-conservation amplification of an initial magnetic field of the WD, and many other systems like intermediate-mass and millisecond pulsars. A "double degenerate"

AIC, resulting from the merger of two white dwarfs with a short orbital period, was later discussed as a complementary possibility to the "single degenerate" channel, analogously to the problem of Type Ia supernova progenitors to which they have a kinship.

Such events have never been positively identified, a fact that is not at all surprising since their luminosity are expected to remain low. The first detailed calculation of the AIC (Fryer et al., 1999) obtained an important output of exotic isotopes in the $\sim 0.1 M_{\odot}$ ejecta, and proceed to deduce an upper limit to the occurrence in the galaxy based on the measured abundance of them. This exotic isotope production has been challenged by (Qian and Wasserburg, 2007), and makes the issue of the upper limit uncertain.

On the other hand, population synthesis have yielded the expectation of $\sim 10^7$ pulsars formed by AIC in the single-degenerate channel and a few times this figure coming from the double-degenerate channel (Wang and Liu, 2020). This are high numbers and may be in tension with the estimated rate of $\leq 0.1\%$ of the total neutron star population estimated by Fryer et al. (1999). If the overproduction of exotic isotopes can be avoided, high rates could be eventually accepted. The alternative way out of this quandary is that the number of suitable progenitor systems is overestimated, and that AIC NSs will not be produced in many of the current candidates mergings, but which of these solutions is viable remains unsolved for the present.

The production of neutron stars in the single-degenerate channel would be in a narrow range around $1.25 M_{\odot}$ naively, but models envisage the accretion to resume after their formation. Therefore, the actual range of the neutron star masses may extend all the way up to the highest measured masses if the accretion conditions allows it. For the double-degenerate channel, the expected range is different, and is believed to span the range $1.4 - 2.8 M_{\odot}$, with a slight variation according to the chemical composition of the WDs (Wang and Liu, 2020). We note that this may be an efficient way to form extremely heavy neutron stars "at birth", a feature that may be required if more heavy objects are detected. The contribution of GW observations to this task is very important, as suggested by the detection of a $2.6 M_{\odot}$ object in the merge GW190814 (Abbott et al., 2020), although the true nature of this component remains to be confirmed. The recent detection of the gamma-ray burst GRB 211211A, suggested to arise from a compact star merger (Gao et al., 2022; Gompertz et al., 2023), was observed to have a longer duration than the sGRB 170817A originated from the merger of two NSs. It is possible that this

new event resulted from the merger of a NS with a WD, living a magnetar behind (Zhong et al., 2023). If confirmed to be true, this will add a new window of possibilities to the formation of NSs.

2.3.4 Observational properties

X-ray satellites and radio telescopes have provided different approaches to measure fundamental parameters of neutron stars, in addition to the masses obtained from binary systems. The properties of these objects depend directly on the adopted microscopic model, which describes the equation of state.

- Mass: The gravitational mass can be inferred directly from observations of X-ray binaries, pulsar binaries and gravitational waves. Determining the mass of a neutron star provides a unique test for predictions that combine nuclear matter theory and general relativity. In addition, observed masses reveal information about the final stages of stellar evolution, and determining the masses of X-ray sources allows obtaining information about the cores of stars that have gone through the final stage of stellar evolution.

- Dispersion index and pulsar distance: The "pulsating" nature of emissions and the dispersive nature of the interstellar medium provide the dispersion index, which allows estimating the distances of individual pulsars.

- Rotational periods: Pulsars with periods of 1.6 ms have already been observed, so the equation of state that describes nuclear matter must account for this result, as well as for the masses. The detection power of millisecond pulsars, with periods below 4ms, is still very small, so statistics obtained to date may be distorted from reality, such that the non-detection of objects with periods below 1ms does not mean that they do not exist. In addition, pulsars are losing angular momentum due to the radiation they emit, consequently the rotation period of these objects increases.

- Radius: Measuring radii of $10km$ at distances of at least 10^{15} km is currently impossible. There are no methods to directly determine the radius of a neutron star. However, the combination of observational data with theoretical assumptions allows predicting these values. The discovery of a nearby neutron star, RXJ 185635-3754,

allowed, through X-ray flux and temperature (which is obtained assuming that the star is a blackbody), to estimate an effective radius of $\sim 7km$. If the existence of objects of this size is confirmed, once again it will be necessary to find equations of state that are consistent.

- Magnetic fields: The theory of pulsars is based on the idea that neutron stars are highly magnetized objects. It is estimated that the magnetic field inside these objects is of $\sim 10^{12} - 10^{13}\ G$. This estimate is obtained from the lines of the X-ray spectrum.

There are still other properties of compact objects that can be obtained from observational data. Weber (1999) presents a more detailed approach to this topic.

2.4 Relativistic stars

Under Newton's theory, a mass density ρ must generates a gravitational field that obeys to the Poission equation:

$$\nabla^2\phi = 4\pi G\rho. \tag{2.15}$$

Starting from this assumption, Einstein developed his theory of relativistic gravitation for a curved manifold, where a source of a gravitational field should had a concept analogous to the mass density and be invariant. He defined this source as the *energy-momentum* tensor ($\mathbf{T}$). The relativistic equation should then be a generalization of Poisson's equation without any preferred coordinate system and satisfying the *Equivalence Principle* (local conservation of energy and momentum; Schutz, 2009). Einstein came then with what is roughly recognized as the *Einstein Field Equations* (EFE):

$$G^{\alpha\beta} = 8\pi T^{\alpha\beta}, \tag{2.16}$$

where $\mathbf{G}$ is the metric tensor. This is a system of ten coupled nonlinear differential equations, from which six are independent. That said, it is not easy to solve the EFE analytically, and most solutions are studied numerically. Einstein introduced the cosmological constant (Λ) later, to obtain static solutions for the large-scale behaviour of our universe, but we do not include it in Eq. 2.16 since it is not important for describing relativistic stars.

It is worth mentioning that the EFE are not the only equations that satisfies all the necessary conditions for a gravitational field in a curved manifold. Alternative theories

exists, but until now Einstein equations have passed all tests, both in weak and strong field, and does not show conflicts with experiments, despite of being the most simplistic description until now.

For an uncharged, static and spherically symmetric fluid, the line element (metric) of Minkowski space is given by:

$$ds^2 = -c^2 e^{2\nu(r)} dt^2 + e^{2\lambda(r)} dr^2 + r^2(d\theta^2 + \sin^2\theta d\phi^2). \tag{2.17}$$

With these simplifications and assuming that pressure is isotropic, the application of Eq. 2.16 leads to expressions for the surviving components, which are:

$$\begin{aligned}
\frac{8\pi G}{c^2}\rho(r) &= \frac{\lambda' e^{-\lambda}}{r} + \frac{1 - e^{-\lambda}}{r^2}, \\
\frac{8\pi G}{c^4}p(r) &= \frac{\nu' e^{-\lambda}}{r} - \frac{1 - e^{-\lambda}}{r^2}, \\
\frac{8\pi G}{c^4}p(r) &= e^{-\lambda}\left[\frac{\nu''}{2} + \frac{\nu'^2}{4} - \frac{\nu'\lambda'}{4} + \frac{\nu' - \lambda'}{2r}\right],
\end{aligned} \tag{2.18}$$

where the lines represents derivatives with respect to r. Now we have four unknown quantities as a function of the radial coordinate (λ, ν, ρ, p), and only three equations. To break this degeneracy is necessary to provide an independent equation corresponding to some additional hypothesis (de Avellar and Horvath, 2010):

- If one of the four mentioned quantities is given (by an *ansatz*, for example), an exact or numerical solution can be found by integration. This, however, does not guarantee any control over the *equation of state* (EoS), which gives a relation between pressure and density $p(\rho)$;

- If the EoS is given, the integration can be (at least numerically) performed and the properties of the stellar model follow;

- If an EoS and one of the functions are given, a match of the overdetermined system can be achieved, but this is in general possible for only certain values of the model parameters.

If more degrees of freedom are provided, like a pressure anisotropy, the third route can be employed without an overdetermined system.

Karl Schwarszchild was the first, in 1916, to found an exact solution for these equations. His solution was build for the outside region of an static and spherically symmetric body,

and revealed a singularity for $r_s = 2M$[3], called *Schwarzschild radius*, that represents the minimum radius an relativistic object can have withouth gravitationally collapsing.

2.4.1 Criteria for physical acceptability

To describe a relativistic object, the exact solutions of EFE must satisfy a few conditions in order to be physically acceptable and, assuming $G = c = 1$, these are:

i. Regularity of the gravitational potential at the origin:

$$e^{2\lambda(0)} = 1 \qquad and \qquad (e^{2\lambda(r)})'_{r=0} = 0,$$

$$e^{2\nu(0)} = cte \qquad and \qquad (e^{2\nu(r)})'_{r=0} = 0.$$

Otherwise the curvature of spacetime at the center of the star would diverge or become infinite.

ii. Radial pressure and energy density profiles must be positive definite at the origin.
To ensure that the star has a finite mass, exerts an outward force to counter gravity, and maintains a well-behaved and regular solution.

iii. Radial pressure must vanish at some finite radius:
Pressure function must be continuous everywhere, otherwise an infinite pressure gradient would emerge. Since the pressure is null in the vacuum outside the star, so it has to vanish at the surface of the star.

iv. Energy density and radial pressure profiles must decrease monotonically from the centre to the boundary.
Or the pressure gradient would become too steep, resulting in an imbalance and a tendency for the star to collapse under gravity.

v. The sound speed must be subluminal everywhere ($v_s^2 = dP_r/d\rho < 1$):
To maintain the causality, the sound speed inside the star must be lower than the speed of light.

vi. At the surface of the star, the metric needs to correspond to the Schwarzschild solution:

$$e^{2\nu(r)} = \left(1 - \frac{2M}{R}\right) \qquad and \qquad e^{2\lambda(r)} = \left(1 - \frac{2M}{R}\right)^{-1}.$$

[3] This expression is derived assuming $G = c = 1$

These conditions guarantee the usefulness of the solution for a realistic description of stellar models.

2.4.2 Hydrostatic equilibrium

The stellar structure is sustained by the *hydrostatic equilibrium*. In case of regular stars, this equilibrium is obtained from a combination of Newton's 2nd law and classical gravity law, resulting in:

$$\frac{dP}{dr} = -G\frac{M\rho}{r^2}. \tag{2.19}$$

From this result we see that the gradient of pressure is the responsible for sustaining the star, and that the pressure must decrease from the centre to the surface. For compact stars, however, the equilibrium must be described from the EFE.

Tolman (1939) and Oppenheimer and Volkoff (1939) derived, independently, the equation of hydrostatic equilibrium for compact stars with spherical symmetry, recognized as the *Tolman-Oppenheimer-Volkoff* (TOV) equation. This equation, taken together with the mass continuity completely determine the structure of spherically simetric and static relativistic stars:

$$\frac{dp}{dr} = -\frac{Gm(r)\rho(r)}{r^2}\left(1+\frac{p(r)}{c^2\rho(r)}\right)\left(1+\frac{4\pi r^3 p(r)}{c^2 m(r)}\right)\left(1-\frac{2Gm(r)}{c^2 r}\right)^{-1}, \tag{2.20}$$

$$m(r) = 4\pi\int_0^R r^2\rho(r)dr. \tag{2.21}$$

The Eq 2.20, is the relativistic correction to the Eq. 2.19, and gives the balance between pressure acting radially outward, and the gravitational force acting radially inward. Compared with the Newtonian case, this correction increases the magnitude of the pressure gradient, establishing a limit value for both mass and radius. This feature is a purely general relativistic effect arising from the denominator $(1-2Gm/c^2r)$. The Eq. 2.21 defines the *gravitational mass* of the star as a function of the radius and of the density, where $m(r=R)$ is the mass within a sphere of radius R.

Oppenheimer and Volkoff were the first to apply an equation of state to describe the macroscopic properties of a NS. They assumed that the star was made of a degenerate Fermi gas of neutrons. The maximum mass resulted to be 0.7 $M_\odot$, highly contradicting the observed masses observed for these objects, as we will show latter.

2.4.3 Mass-radius relation

The equation of state is a key ingredient since it relates the microphysics of the star with the relativistic macroscopic properties. Given an EoS and initial conditions, the TOV can be solved iteratively. At the center of the star ($r = 0$) the mass and pressure derivative must be null. From a given central density ρ_c, the central pressure follows from the EoS. A mass at $r + dr$ is found by integrating Eq. 2.21, and followed by an integration of TOV equation at the same radial coordinate. The energy density follows again from the equation of state, so the process can be repeated increasing the r coordinate, until the pressure vanishes whithin a radius that define the stellar radius $r = R$, and consequently the mass of the star $M(R)$.

For each EoS there is a unique relation between stellar mass and central density. Solving the TOV for a given equation of state covering the valid range of densities for the matter into question provide us with a *mass-radius* relation. Figure 2.8 shows examples of several sequences of stars, each of them built from different EoSs. Mass measurements obtained from different methodologies are capable of constraining the valid equations, since they need to accomodate the observed value at least as a maximum. The GW190814 is the result of a merger between a black hole of 23 $M_\odot$ and a companion star with a nature yet undetermined with a mass of 2.59 $M_\odot$ (Abbott et al., 2020). If confirmed as a NS, this discovery will be a breakthrough for the astronomical field.

2.4.4 Rhoades-Ruffini limit

Establishing the maximum mass of NSs is vital not only to understand the true nature of matter inside it but also to set the limit from where the formation of a black hole is unavoidable. The exact nature of matter at supranuclear densities is a long-posed problem for which a solution is still nowadays elusive, this is why the availability of an "absolute" value for the limit mass is so important.

In fact, as Rhoades Jr and Ruffini argued in 1974, it is not really necessary to know the exact equation of state to obtain a valid theoretical limit. This theoretical threshold on the mass comes from well-established physical principles that all the matter should obey, which are:

1. The compact star must obey the General Relativistic equation for hydrostatic equi-

librium;

2. Matter must obey the Le Chatelier Principle, stating that a disturbance in a system in equilibrium will be opposed to restoring the equilibrium;

3. Matter must obey the Principle of Causality, which implies that the sound speed must remain lower than the speed of light in the medium.

To comply with these three requirements, Rhoades Jr and Ruffini assumed that the EoS is well-known until a fiducial density of $\rho_\star = 4.6 \times 10^{14}\ g/cm^3$. Above it, they assumed that the equation of state is the stiffest possible, with a sound speed equal to the speed of light. Thus, they found a maximum possible mass for a neutron star of about 3.2 $M_\odot$.

The Rhoades-Ruffini mass limit can be expressed as (see Chamel et al., 2013):

$$m_{RR} \simeq 3.0 \left(\frac{5 \times 10^{14}}{\rho_\star}\right)^{1/2} [M_\odot]. \tag{2.22}$$

As a conclusion, all compact objects whose mass are measured to be higher than 3.2 $M_\odot$ must be a black hole provided it is non-rotating, isotropic and GR holds.

As a further development, allowing the violation of the causality, using an incompressible fluid, the mass limit can be expressed as (see Chamel et al., 2013):

$$m_{RR,non-causal} \simeq 5.09 \left(\frac{5 \times 10^{14}}{\rho_\star}\right)^{1/2} [M_\odot]. \tag{2.23}$$

In Eq. 2.22 and Eq. 2.23, $\rho_\star$ is the value assumed to be the fiducial one.

It is worth stressing that the Rhoades-Ruffini limit does not take into account other effects such as rotation and anosotropies in the fluid's pressure that, as we will discuss later in this thesis, allows matter inside the NS to support masses higher than 3.2 $M_\odot$.

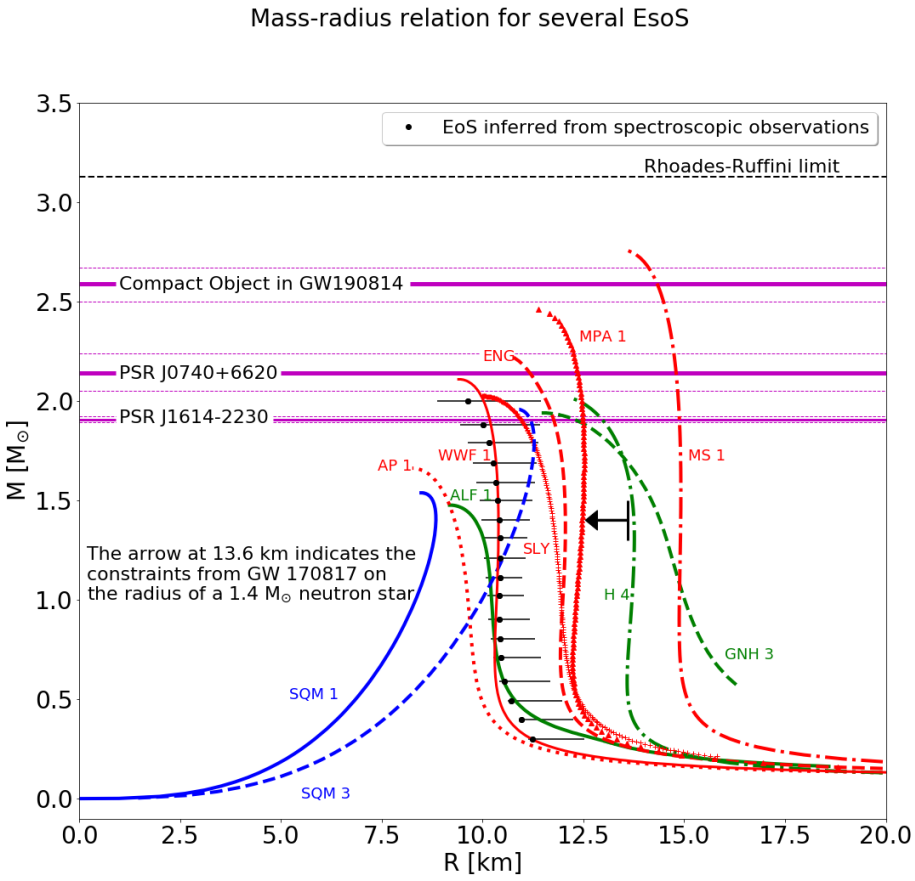

Figure 2.8: Mass-radius relation for several equations of state, named in the Figure, illustrating the "families" of equations of state. The hadronic EsoS are the AP 1, ENG, MS 1, MPA 1, SLY and WWF1; the hybrid ones are the ALF 1, GNH 3 and H4; the ones with strange quark matter are the SQM 1 and SQM 3. The black dots represent an EoS inferred from spectroscopic observations. The data for this $M - R$ diagram and the observational dots were taken from `http://xtreme.as.arizona.edu/` (Earlier compilations and naming conventions are from Lattimer and Prakash, 2001 and Read et al., 2009. The full list included above is from Özel and Freire, 2016) In this Figure, we also plot: PSR J1614-2230 ($m = 1.928 \pm 0.016\ M_\odot$), PSR J0740+6620 ($m = 2.14^{+0.10}_{-0.09}\ M_\odot$), and the compact object in GW190814. Note that the mass values of PSR J1614-2230 and PSR J0740+6620 are updated in Table A.1 . The sequences were calculated from the TOV, i.e., they do not include rotation. Extracted from Horvath et al. (2023).

Chapter 3

The mass distribution of neutron stars

Although pioneer works pointed out the possibility of a wide range of NS masses, for more than 30 years after the discovery of pulsars the most accepted idea for astronomers and astrophysicists was that a so-called *canonical* mass value of $\sim 1.4 M_{\odot}$ should be imprinted on NS at birth. This was based on the state of the iron core prior to the beginning of collapse, supported by the electron degeneracy pressure. Nowadays, as discussed in Sec. 2.3.3, it is widely known that depending on the initial mass of the progenitor star and its metallicity, considerably smaller *Fe* cores can colapse leaving NSs with masses as low as 1.17 $M_{\odot}$ (Suwa et al., 2018), at the same time that heavier cores can explode forming remnant NSs with masses up to ~ 2 $M_{\odot}$ (Burrows and Vartanyan, 2021). In the case of the most massive NSs observed so far (≥ 2 $M_{\odot}$), it is not clear yet if they are born massive, and/or substantial accretion is necessary to achieve these high masses.

Discussions about the mass range a NS can attain were presented in many works, as for example those referenced in Joss and Rappaport (1976); Thorsett and Chakrabarty (1999); Baumgarte et al. (1999) and many others. Observational works at that time seemed to provide support to the idea of a single-mass scale. Finn (1994) employed a statistical analysis of a sample of four double neutron star (DNS) systems with the constrained masses of eight NS, and found that masses should fall predominantly in the range $1.3 < m/M_{\odot} < 1.6$. Thorsett and Chakrabarty (1999) obtained a mean value of $1.35 \pm 0.04 M_{\odot}$ for a sample of 19 NS masses, and no evidence for a significant dispersion around the single scale.

At the turn of the 21st century, mass measurements started to show a significant spread, indicating a possible evidence of different NS types that would be reflected in a bimodality or multimodality in the NS mass distribution, instead of an unimodal single-scale shape.

As seen in van den Heuvel (2004), a theoretical speculation of the possible existence of *three* neutron star classes already existed. In addition to the observational advance, the technological advance has provided us with faster and higher-capacity computers, allowing the implementation of increasingly robust statistical analysis. This fact permitted the Bayesian approach to spread among scientific community through *Markov Chain Monte Carlo* simulations. Several groups employed these techniques to extract information from the mass distribution of NSs (Schwab et al., 2010; Valentim et al., 2011; Zhang et al., 2011; Kiziltan et al., 2013; Özel and Freire, 2016) and its maximum mass (Antoniadis et al., 2016; Alsing et al., 2018; Shao et al., 2020), each of them with their own model particularities.

Schwab et al. (2010) was the first to discuss the evidence of a bimodal distribution based on a sample of 14 well constrained masses (with uncertainties $\lesssim 0.025\ M_\odot$). The first peak was found to cluster around $\sim 1.25 M_\odot$, which they associated with NS formation from an ECSN expected to occur in degenerate cores of *OMgNe* (Nomoto, 1984; Podsiadlowski et al., 2004), as we discussed in Sec. 2.3.3. The second peak was found around $\sim 1.35 M_\odot$, and was associated with the "standard" Fe CCSN.

A previous work from our group (Valentim et al., 2011), based on a Bayesian inference of 54 measured NS masses, gave evidence for a bimodal distribution distinguishing a group centered at 1.37 $M_\odot$ from a heavier group with a mean at $1.73 M_\odot$. The NSs in the first group were associated with the "standard scenario", while those in the second group are likely a combination of NSs that may have passed by an accretion phase leading to substantially higher masses (Bhattacharya and van den Heuvel, 1991; Tauris and Van Den Heuvel, 2006), in addition to those that are born naturally more massive. No evidence was found for a clustering of masses around $1.25 M_\odot$, expected from evolutionary grounds. This class formed from ECSN seems to be "maskared" by the standard scenario when we analyze the whole sample of NS masses, what could be a selection effect. All subsequent analysis showed consistent results with those found in Valentim et al. (2011).

Different distribution families can be invoked in order to describe the mass distribution of NSs, with the selection methods responsible for indicating which one is the most favorable. However, the preference for analysis employing multimodal models is an attempt to accommodate the different formation pathways expected for these objects. All analysis conducted with the data available to date converge towards a consensus on bimodality. Furthermore, works like that of Shao et al. (2020) have considered mixture models invol-

ving different families of distributions, but, as of now, there is also no evidence suggesting more complex models than a Gaussian mixture.

The first analysis concerned with the upper mass limit of NSs was introduced by Antoniadis et al. (2016), and later implemented by Alsing et al. (2018). Analyzing a sample of 74 NSs, this last result showed evidence for a bimodal distribution compatible with all previous works, with the addition of a sharp cut-off at $2.12^{+0.09}_{-0.12}$ $M_\odot$. A following analysis included a few new massive NSs, as the PSR J0740+6620 (Cromartie et al., 2020), PSR J1600-3053 (Arzoumanian et al., 2018), PSR J1959+2048 and PSR J2215+5135 (Kandel and Romani, 2020), as well as the component masses of GW170817 (Abbott et al., 2019) and GW190425 (Abbott et al., 2020) and the isolated star PSR J0030+0451 (Riley et al., 2019). Despite of the bimodal behaviour clustered around the same values as previous works, they found a slightly higher maximum mass, $2.26^{+0.12}_{-0.05}$ (68% credible interval; Shao et al., 2020).

While the current *lowest* mass observed for a NS is 1.174 $M_\odot$ (Martinez et al., 2015), the most massive ones are above 2 $M_\odot$. Although PSR J0740+6622 (Cromartie et al., 2020; Fonseca et al., 2021) was, until the publication of Shao et al. (2020), recognized as the heaviest well-constrained pulsar, with $m = 2.08 \pm 0.07$ $M_\odot$, there are at least other 10 systems in the sample with masses that can be significantly higher. However, mass measurement methods of these objects are subject to larger uncertainties since their orbital inclination angles are not well constrained, and the pulsar mass is proportional to $1/\sin^3 i$. The recent discovery of PSR J0952-0607 (Romani et al., 2022) revealed a robust mass of 2.35 ± 0.17 $M_\odot$, obtained from spectrophotometry and imaging of the companion star, and placed a lower limit in the maximum mass of $M_{max} > 2.19$ $M_\odot$, yet to be confirmed.

While the currently most accepted maximum mass still hovers around values not much higher than 2 $M_\odot$, the number of evidences that support the existence of extremely massive neutron stars has been increasing in recent times. GW detections have created a tension in the expected value for the maximum mass since analyses of the GW170817 event seems to require $m_{max} < 2.3 M_\odot$, while the GW190814 event requires $m_{max} > 2.5 M_\odot$ if the less massive component is confirmed to be a NS (Nathanail et al., 2021). An analysis by the LIGO/Virgo collaboration itself suggests that the GW190814 is likely an *outlier* from the class of GW signals emitted by BH-BH mergers (Abbott et al., 2021), i.e., it is likely that the component with $2.59^{+0.08}_{-0.09}$ is a NS. An analysis of four LIGO-Virgo NSBH events,

assuming the existence of rapidly spinning NSs, found a maximum mass of $2.7^{+0.5}_{-0.4}$ $M_\odot$ (90% credibility; (Ye and Fishbach, 2022), 2022). However, if only non-spinning NSs are considered, the maximum mass must be > 2.53 $M_\odot$ (90% credibility). In the same work they argued that a sample pof > 150 NSBH merger events is necessary to constrain the maximum mass of non-spinning NSs with an accuracy of ± 0.02 $M_\odot$.

In this Chapter we present an analysis of the mass distribution of binary neutron star systems, with the most up-to-date sample of 112 NSs (Fig. 3.1). We did not included masses from isolated NSs (such as PSR J0030+0451) neither from GW components in our analysis, since it is not clear yet if we can treat them as part of the same distribution, as they might present significantly different features. It is important to note, however, that although the shape of distribution can be different between galactic and extragalactic populations, for example, astrophysical information from all kind of sources are key to set reliable constraints on the upper limit of NS masses. The current sample of galactic pulsars still does not show any evidence for three or more distinct classes of NSs, but we shall see that our analysis favors the existence of ultra-massive NSs, with a result of $m_{max} = 2.60$ $M_\odot$. We comment on the reasons leading to a different result compared to those found by Alsing et al. (2018) and Shao et al. (2020). We also stress that we use the notation m_{max} for a statistical threshold, which is not necessarily equivalent to the physical limit derived from the TOV equation (M_{max}). As the sample grows asymptotically, the value of m_{max} can approach (if stellar evolution allows it) the true maximum mass M_{max} predicted by GR, constraining the valid EoS.

3.1 Neutron star mass measurements

The vast majority of NSs are observed as pulsars, rapidly-rotating and high-magnetized neutron stars emitting beams of radiation along its magnetic axis that are seen on Earth as a pulse due to the lighthouse effect (Rezzolla et al., 2018). The extreme regularity of pulses, responsible for recognizing pulsars as the most stable clocks in the observable universe, makes *pulsar timing* the most accurate method to determine masses of NSs, as well as test fundamental physics. The procedure consists in monitoring the times-of-arrival (ToAs) of pulses over several years to determine the pulsar's rotation period. Thanks to the regularity, small deviations of ToAs are detectable with precision. The greater the

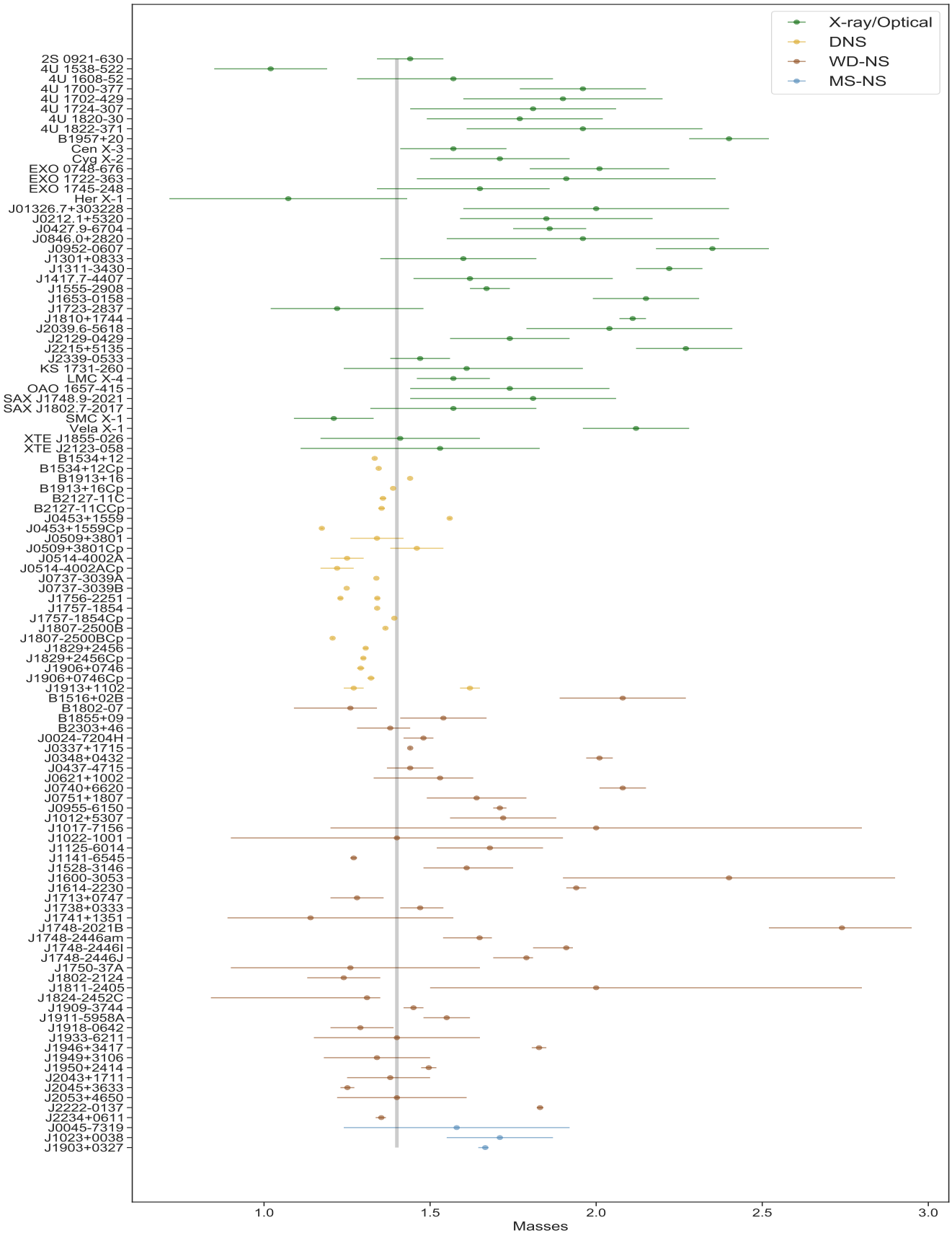

Figure 3.1: The revised and updated sample of 112 systems containing NS, separated by colors in four groups due to system type and showing their corresponding error bars. We considered only systems with pulsar individual mass measured. Masses and references are specified in Table A.1

number of collected ToAs, greater will be the precision achieved.

Nowadays, more than 3300 radio pulsars were observed (see a catalogue in Hobbs et al., 2004), but only a few aspects of them can be directly inferred from observations, and only a tiny fraction of the total sample allows mass measurements. The ToAs reveals the orbital properties of the system expressed in terms of Keplerian parameters: orbital period (P_B), eccentricity (e), semimajor axis projection onto the line of sight ($x = a \sin i$), time (T_0) and longitude (ω) of periastron. From Kepler's third law, a mass function for each component (pulsar, m_p, and companion, m_c) of the system emerges:

$$f_p = \frac{(m_c \sin i)^3}{(m_p + m_c)^2} = \frac{4\pi^2}{T_\odot} \frac{x^3}{P_B^2}. \tag{3.1}$$

where $T_\odot \equiv GM_\odot/c^3 = 4.925490947\ \mu s$ (G is the gravitational constant, c is the speed of light and $M_\odot$ is the solar mass). If both functions can be measured as well as the mass ratio ($q = m_p/m_c$), the individual masses of the system can be determined provided the inclination angle i, responsible for the major uncertainty in these measurements, is known.

In the special case of compact binaries, where the companion is a WD or a NS, relativistic effects, described by post-Keplerian (PK) parameters as functions of Keplerian parameters (Stairs, 2003), influences the orbit and can be measured. These effects are:

1. Orbital period decay, $\dot{P}_b$:

$$\dot{P}_b = -\frac{192\pi}{5} \left(\frac{P_b}{2\pi T_\odot}\right)^{-\frac{5}{3}} \left(1 + \frac{73}{24}e^2 + \frac{37}{96}e^4\right) \left(1 - e^2\right)^{-\frac{7}{2}} \frac{m_p m_c}{m^{1/3}}; \tag{3.2}$$

2. Range of Shapiro delay, r:

$$r = T_\odot m_c; \tag{3.3}$$

3. Shape of Shapiro delay, s:

$$s = \sin i = x_p \left(\frac{P_b}{2\pi}\right)^{-2/3} \frac{m^{2/3}}{T_\odot^{1/3} m_c}; \tag{3.4}$$

4. "Einstein delay", γ:

$$\gamma = e \left(\frac{P_b}{2\pi}\right)^{1/3} T_\odot^{2/3}\ \frac{m_c\,(m_p + 2m_c)}{m^{4/3}}; \tag{3.5}$$

5. Advance of periastron, $\dot{\omega}$:

$$\dot{\omega} = 3 \left(\frac{P_b}{2\pi}\right)^{-5/3} \left(1 - e^2\right)^{-1} (m\ T_\odot)^{2/3}. \tag{3.6}$$

If two PK parameters are measured, the component masses are individually determined. If more PK parameters are measured, is also possible to test GR within a very high precision, as shown in Kramer et al. (2021). Accretion torques in binary systems can circularize the orbits, and consequently many NS binaries have extremely low eccentricities, hampering the measurement of $\dot{\omega}$ and γ. On the other hand, the Shapiro delay of the pulses due to the gravitational field of the companion is dependent on the orbital inclination, being typically relevant for systems with high inclinations. Lastly, detection of orbital decay due to gravitational wave radiation, ($\dot{P}_b$) is only possible for very short orbits. All these conditions makes pulsar mass measurements a challenging task. If relativistic effects are too small, they can go undetected even after years of pulsar timing.

The *Neutron star Interior Composition ExploreR* (NICER) is a telescope placed on board of the International Space Station in 2017, to enable timing and rotation-resolved spectroscopy of thermal and non-thermal X-ray emissions of NSs. Recently, it allowed to precisely measure radii and masses of two pulsars, namely PSR J0740+6620 and PSR J0030+0451 (Riley et al., 2019, 2021). Despite being a promising avenue, the dominant method to infer NS masses continues to be the study of the orbital motion in binary systems determined through pulsar timing of radio sources (Horvath and Valentim, 2017).

3.1.1 Optical spectroscopy

If the pulsar has an optically bright low-mass companion, like main sequence and post-main sequence stars or WDs, a phase-resolved spectroscopy of the companion yields the orbital radial velocity amplitude (K_c), which combined with x and P_b, provides the binary mass ratio $q = (m_p/m_c) = (K_c/K_p)$. For WD companions, their radii can be estimated given the distance (d) to Earth is known, and the optical flux (F_O) and effective temperature (T_{eff}) are measured:

$$R_{WD} = \left(\frac{F_O}{\sigma}\right)^{1/2} \left(\frac{d}{T_{eff}^2}\right), \tag{3.7}$$

where σ is the Stefan-Boltzmann constant. Their masses can thus be estimated combining the effective temperature with the surface gravity fitted from a synthetic atmosphere. As we can see, this method is model-dependent and can lead to large systematic errors.

Spider systems are of particular interest since most of the largest NS masses have been inferred from them, through spectrophotometry methods (Linares, 2020; Horvath

et al., 2020). These are compact binary millisecond pulsar systems with semi-degenerate companions, classified under two groups. The Black-Widows (BW) have companions with masses $m_c \leq 0.05\ M_\odot$, while for Redbacks $0.1 \leq m_c \leq 0.5\ M_\odot$. The companion's outer envelope is believed to be ablated by the intense pulsar wind[1], filling the system with intra-binary material that causes the radio pulsation to be scattered and absorbed (Kansabanik et al., 2021). As a consequence, their optical light curves are sensitive not only to the orbital inclination, but also to heating models of companion surface's, difficult to predict. Large systematic error on the inclination angle estimate can result in large bias on the mass estimate for this class of pulsars.

3.1.2 Gamma-ray eclipses

Millisecond pulsars also emit gamma-ray pulsations (Atwood et al., 2009). Contrary to other wavelenghts, it seems unlikely that γ-rays are absorbed in the diffuse intra-binary material. Consequently, eclipses observed in gamma-ray are potentially associated only with the occultation of the pulsar by the companion, what provides a robust determination of the inclination angle. The work in Clark et al. (2023) searched for gamma-rays eclipses in 49 confirmed and candidate spider systems, finding it to be present with a confident level in 5 systems, from where masses were determined (Table 3.1). In only one out of 5 systems the inclination angle was found to be inconsistent with optical modelling. For PSR B1957+20, photometric observations provided $63^o \lesssim i \lesssim 67^o$, which results in a best fit with a high mass, $m = 2.4 \pm 0.1\ M_\odot$ (Van Kerkwijk et al., 2011). The recent observations in γ-rays requires $i > 84.1^o$, corresponding to a significantly lower mass, $m = 1.81 \pm 0.07\ M_\odot$. The difference they found for mass estimates can have a huge impact on the maximum mass of NSs and, consequently, on the state of matter at ultra-high densities. The treatment in (Clark et al., 2023) relies in simplistic assumptions for companion winds, and further studies are necessary to confirm its robustness.

[1] This is the reason why these systems are called spiders, in an analogy with the black widow and redback spiders which are known to kill and devour their male partners.

Pulsar	m_p ($M_\odot$)
B1957+20	1.81 ± 0.07
J1048+2339	1.58 ± 0.07
J1555−2908	1.65 ± 0.04
J1816+4510	1.90 ± 0.13
J2129−0429	1.70 ± 0.11

Table 3.1 - Mass estimates for spider systems with detected eclipses in gamma-rays, derived by Clark et al. (2023).

3.2 Statistical analysis

Statistics is a branch of mathematics dedicated to develop and make use of methods to collect, organize, interpret, present and analyze data. By applying mathematical and computational tools, it has the purpose of infer or predict aspects of a phenomenon from which data is related, helping to make decision based on evidences (data). Statistics is used in a wide variety of fields, including astronomy and astrophysics, and is generally constructed under applications of probability theory, which in turn has the aim of quantifying the associated uncertainty.

Different epistemological definitions are used to construct probabilistic models, as the frequentist, logical, subjectivist and Bayesian. The choice for a specific approach depends on the nature of data, research questions, and the goals of the analysis. The most widely used is the frequentist (or classical) approach, based on the idea that parameters being studied possess a *true* value. The frequentist method focuses on point estimations (*i.e.* means, medians, etc), with the goal of finding the true value that represents the unknown parameter. In this approach probabilities are defined as the relative frequency of an event occurring in a infinite number of repetitions of the same experiment, and treated as measures of uncertainties associated with data. One of the fundamental aspects of frequentist approach is the hypothesis testing, where the evidence against a "null hypothesis" is quantified respect to alternative hypothesis, based on sampled data. The frequentist treatment is based on criteria and principles including impartiality, efficiency, consistency, conditionality, likelihood and etc.

On the other hand, for Bayesian statistics probability is identified as a *credible* degree that can be measured. This approach does not account only for data, as in the frequentist case, but also for the previous knowledge/beliefs one have about the subject being studied,

described in terms of a probability distribution. It is important to note, however, that this *a priori* knowledge can change when new evidence comes up, as well as different individuals can have distinct beliefs for the same problem in light of the same evidences. For these reasons some statisticians consider the Bayesian approach controversial and highly subjective. However, analysis made under the Bayesian treatment are shown to be consistent, and provides good predictions.

The main difference between both approaches is that frequentist statistics tries to eliminate/reduce uncertainties of a model providing estimates for the data, searching for the "true value" of each parameter, while Bayesian statistics tries to preserve and refine uncertainties updating beliefs with new evidences provided by the observed data. Furthermore, Bayesian analysis can be specially advantageous when dealing with small samples, in comparison to classical statistics, and offers a natural framework for decision making under uncertainty.

3.2.1 Bayesian Inference

The construction of Bayesian statistics is based on the *Bayes theorem* (Bayes, 1763), derived from axioms of conditional probabilities, and defined as:

$$P(A|B) = \frac{P(A \cap B)}{P(B)}, \tag{3.8}$$

which asserts that, the probability of event A to occur given that event B occurred, is equivalent to the ratio between the probability of occurrence of both A and B and the probability of B only.

The same is valid for the conditional probability of B given A, so knowing that $P(A \cap B) = P(B \cap A)$, we are led to the relation:

$$P(B)P(A|B) = P(A)P(B|A), \tag{3.9}$$

which results in the *Bayes theorem*:

$$P(A|B) = \frac{P(A)P(B|A)}{P(B)}. \tag{3.10}$$

In the case we are interested in the *posterior* probability distribution of a parameter θ, or a set of parameters $\boldsymbol{\theta}$, given the observed data (D), we may write:

$$P(\theta|D) = \frac{P(\theta)P(D|\theta)}{P(D)}, \tag{3.11}$$

where:

- $P(\theta|D)$ is the *posterior* distribution, translated as degree of credibility on θ given that an evidence (D) has been taken into account;
- $P(\theta)$ is the *a priori* distribution, which express a confidence degree on θ without taking the evidence D into account - it is our previous belief about each parameter in the model;
- $P(D|\theta)$ is the *likelihood function*, that provides the probability of detecting a data D from a model with the fixed parameter θ;
- $P(D)$ is the *predictive* probability, which is a normalization constant.

3.2.2 Marginalization

Suppose that we have a distribution $P(\theta, \phi|D, M)$, where M is an additional information regarding a hypothesis on D, and that we are only interested in inferences about the parameters θ. In this case, ϕ is what we call a *nuisance* parameter. In the Bayesian approach, is possible to marginalize the *posterior* probability by integrating out the irrelevant degrees of freedom:

$$P(\theta|D, M) = \int P(\theta, \phi|D, M)d\phi. \tag{3.12}$$

where $P(\theta|D, M)$ is called the marginal *posterior* distribution for θ (Bernardo and Smith, 2009).

3.2.3 Model Selection

In the Bayesian approach, model selection is important in order to select the most appropriate model among a set of candidates, based on the observed data, by assessing their relative strengths. It allows to choose a model that strikes a balance between simplicity and flexibility, avoiding an overfitting of the data, and that provides the best predictions for future observations. There are a variety of model selection methods, each of them based on different assumptions and evaluating criteria. Statisticians recommends to apply multiple methods to enhance the rigor and reliability of the model selection, helping to mitigate the limitations of individual methods. If multiple methods consistently point to the same model, it increases the confidence in the selection.

In the following we describe one of the selection methods, based on the *Bayes factor* (BF). Suppose that M_i denotes the proposition asserting that a model i describes the data, and I denotes the proposition asserting that one of the candidate models do describes the data. *Bayes theorem* might be used to calculate the probability of M_i, given that one of the models actually describes the observations:

$$P(M_i|D,I) = \frac{P(M_i|I)P(D|M_i,I)}{P(D|I)}, \tag{3.13}$$

with $P(M_i|I)$ corresponding to the *a priori* distribution, M_i resembling the parameter and I the model.

The ratio between the probability for model M_i and for model M_j is called the *odds* in favor of M_i over M_j, denoted by O_{ij}:

$$O_{ij} = \frac{P(M_i|D,I)}{P(M_j|D,I)} \tag{3.14}$$

$$= \frac{P(M_i|I)}{P(M_j|I)} \frac{P(D|M_i,I)}{P(D|M_j,I)} \tag{3.15}$$

$$= \frac{P(M_i|I)}{P(M_j|I)} B_{ij}, \tag{3.16}$$

where B_{ij} is the *Bayes factor*. This factor is nothing more than the ratio between model's likelihoods, and quantifies the support of one model over the another. Table (3.2) summarizes the interpretation of B_{ij} recommended by Kass and Raftery (1995).

Bayesian model comparison is based on averaged likelihoods, so it tends to favor simpler models even when simple and complicated models have equal *a priori* probabilities, a property known as *Ockham's razor*. For frequentist statistics, model selection is usually performed under *likelihood ratio tests* based on maximum value of likelihoods. In these tests model complexity are not taken into account.

Table 3.2 - Bayes factor interpretation

$ln(B_{ij})$	B_{ij}	Strength of evidence for M_i over M_j
0 to 1	1 to 3	Not worth more than a bare mention
1 to 3	3 to 20	Positive
3 to 5	20 to 150	Strong
>5	>150	Very strong

The integrals needed to calculate the average likelihoods in the Bayesian framework are often challenging, so it is common to use an approximation known as *Bayesian Information*

Criteria (BIC), with a Gaussian approximation to calculate it. The log of Bayes factor can thus be approximated as:

$$ln\ B_{ij} = ln\left(\frac{\mathcal{L}_j(\theta,\phi)}{\mathcal{L}_i(\theta)}\right) - \frac{1}{2}m_\phi lnN, \tag{3.17}$$

where model j is the most complex, with additional parameters ϕ. The m_ϕ is the dimension of ϕ, $\mathcal{L}$ is the model likelihood and N is the sample size. The BIC has the aim of balancing model fit and complexity, usually favoring simpler models, satistying the *Ockham's razor*.

Another alternative method is the second-order *Akaike Information Criteria* (AIK[2]; Akaike, 1974):

$$AIK_{c_i} = -2ln\mathcal{L}_i + 2k\frac{N}{N-k-1}, \tag{3.18}$$

where k is the number of free parameters in the model, so it also balance model fit and complexity. The relative likelihood between two competing models can be calculated as:

$$\delta\mathcal{L}_{\mathcal{AIK}} = exp\left[\frac{AIK_{min} - AIK_{max}}{2}\right], \tag{3.19}$$

and lower AIK values indicate better-fitting models. This method seeks to minimize the information loss, it does not assume any *a priori* distribution, and is asymptotically efficient being suitable for both small and large sample sizes.

The choice between both methods depends on the analysis. While AIC may be preferred for larger samples, as it places less stringent penalties on model complexity, the BIC is particularly useful for smaller samples. However, it is beneficial to compute both criteria and examine their results together with other methods and/or relevant information.

3.2.4 Bayesian sampling

The normalization constant of *Bayes theorem*, also called predictive probability:

$$P(D) = \int P(\theta)P(D|\theta)d\theta \tag{3.20}$$

is often hard to compute, specially for a high-dimensional parameter space. Consequently, for these complex models it is often impossible to find analytical solutions for the *posterior* distributions. Computational Bayesian statistics is based on developing algorithms to draw samples from the true *posterior* distribution, even when only the non-normalized version

[2] The usual acronym for Akaike Information Criteria is AIC. Here we use AIK to distinguish from the acronym for Accretion Induced Collapse.

of it is available. One of the most widespread and implemented method is the `Markov Chain Monte Carlo` (MCMC).

The MCMC method is a class of algorithms that use Markov Chains to generate a sequence of samples from a target probability distribution of interest. These algorithms can also handle models with many parameters, where traditional methods like grid-based approaches and numerical integration are impractical.

3.2.4.1 Markov Chain

Markov Chain is a *stochastic* process[3] for a sequence of random variables $X^1, X^2, ..., X^n$, where X^n is the state belonging to a space state at time n, with the special property of being *memoryless*. This means that the conditional probability of the process at a time n, given the previous states, depends only in the single previous state, at a time $n-1$:

$$P(X^n = x_n | X^{n-1} = x_{n-1}, ..., X^0 = x_0) = P(X^n = x_n | X^{n-1} = x_{n-1}). \tag{3.21}$$

3.2.4.2 Metropolis-Hastings Algorithm

Metropolis-Hastings (MH) is the most general algorithm of MCMC sampling method (Metropolis et al., 1953; HASTINGS, 1970), which generates candidate samples from a proposal distribution and accepts or rejects them based on a probability ratio that depends on the target distribution.

Its operation can be described as follows: suppose we are interested in sampling a distribution $f(x)$ on a state space Ω, with $x \in \Omega$. To construct the transition kernel $K(x, y)$ from a state x to a state y, the MH algorithm uses a two step process:

- Specify a proposal distribution $q(y|x)$;
- Accept draws from $q(y|x)$ with acceptance ratio $a(x, y) = min\left[1, \frac{f(y)q(x|y)}{f(x)q(y|x)}\right]$.

The transition kernel is than given by $K(x, y) = q(y|x)a(x, y)$.

There are multiple ways of constructing a proposal distribution $q(y|x)$ and each of them leads to a different version of MH algorithm (Sharma, 2017). By running the algorithm for a sufficiently large number of iterations, the chain explores the phase space and produces a sequence that approximates the desired distribution.

[3] Process that evolves through time according to some probabilistic law.

Algorithm 1: Metropolis-Hastings Algorithm

Data: Starting point x_1, function $f(x)$, proposal distribution $q(y|x)$

Result: Array of N points, $x_1, x_2, ..., x_N$

for $t = 1$ to $N - 1$ **do**

Obtain a new sample y from $q(y|x_t)$

Sample a uniform random variable U

if $U < \frac{f(y)q(x|y)}{f(x)q(y|x)}$ **then**

$x_{t+1} = y$

else

$x_{t+1} = x$

end

end

3.3 Inferences on the mass distribution of neutron stars

3.3.1 Classical analysis

Although Bayesian statistics have gained strength over the years, frequentist non-parametric hypothesis tests are roughly employed by astronomers to help exploring tentative conclusions about different phenomena and to better understand the data. Kolmogorov-Smirnov (KS) and Anderson-Darling (AD) are two well-known suitable examples of hypothesis tests, and we apply them to gather conclusions about the mass distribution of NSs.

3.3.1.1 Kolmogorov-Smirnov test

A non-parametric test that can be used as a *goodness of fit* test to determine whether a sample follows a specified distribution, or to verify if two samples are drawn from the same distribution. It measures the maximum absolute distance (D_n) between *empirical distribution function* (EDF) of the sample and the *cumulative distribution function* (CDF) of a specified distribution:

$$D_n = \sup_x |\hat{F}(x) - F(x)|, \tag{3.22}$$

where $\hat{F}(x)$ asserts for the EDF and $F(x)$ for the CDF. The null hypothesis is that the sample come from the specified distribution. From KS test it is possible to extract a p-

value, and if it is small[4] suggests that it is unlikely that data came from $F(x)$, and the null hypothesis is rejected in favor of an alternative one.

The advantages of KS test include its generality and ability to handle continuous, discrete and mixed distributions. However, it is more sensitive to differences in the the shape of the distribution in the central region rather than the tails, despite of being more suitable for larger sample sizes.

3.3.1.2 Anderson-Darling test

Similarly to KS, the AD test is also nonparametric, and based on the distance between the EDF and CDF. It is an alternative to the KS test, with the advantage of giving more weight to the tails of the distribution, presenting a more robust result (Babu and Feigelson, 2006). The distance is given by:

$$A^2 = n \int_{-\infty}^{\infty} \frac{(\hat{F}(x) - F(x))^2}{F(x)(1 - F(x))} dF(x), \tag{3.23}$$

where n is the number of observations. The test to assess if data come from the CDF, which is the null hypothesis, is:

$$A^2 = -n - S, \tag{3.24}$$

with

$$S = \sum_{i=1}^{n} \frac{2i - 1}{n} \left[\ln F(x_i) + \ln(1 - F(x_{n+1-i})) \right]. \tag{3.25}$$

A p-value with a given significance level will also determine whether the null hypothesis is rejected or not.

3.3.1.3 Frequentist analysis of NS masses

Following the motivations elucidated in the introduction of this chapter, lets assume the mass distribution of NS masses to be modeled by a Gaussian mixture with n components:

$$P(m_p|\boldsymbol{\theta}) = \sum_{j}^{n} r_j \ \frac{1}{\sqrt{2\pi}\sigma_j} e^{-\frac{1}{2}\left(\frac{m-\mu_j}{\sigma_j}\right)^2} \equiv \sum_{j}^{n} r_j \ \mathcal{N}(m_p|\mu_j, \sigma_j), \tag{3.26}$$

where μ_j and σ_j are the mean and standard deviation of the *j-th* normal component $\mathcal{N}$ with a relative weight r_j, satisfying $\sum_j^n r_j = 1$ to ensure normalization. The goal is to test which model (1, 2 and 3 normal components) is preferred for the sample of binary NS's at

[4] Small compared with a significance level, usually set as $\alpha = 0.05$. So if $p < \alpha$ the model is rejected.

Table A.1. The *maximum likelihood method* is used to derive the values of each parameter. The resulting distributions are:

Unimodal

$$P(m_p|\boldsymbol{\theta}) = \mathcal{N}(1.48, 0.35)$$

Bimodal:

$$P(m_p|\boldsymbol{\theta}) = 0.6\ \mathcal{N}(1.38, 0.15) + 0.4\ \mathcal{N}(1.84, 0.35)$$

Tri-modal:

$$P(m_p|\boldsymbol{\theta}) = 0.1\ \mathcal{N}(1.25, 0.09) + 0.5\ \mathcal{N}(1.40, 0.14) + 0.4\ \mathcal{N}(1.89, 0.30)$$

For each Gaussian mixture we applied both KS and AD tests against the empirical distribution of data. Resultant p-values are shown in Table 3.3. The simplest (unimodal) model is ruled out for both tests, while 2 and 3-component models are not rejected and presents similar p-values, so it is not possible to decide between both models only with KS and AD tests. Figure 3.2 shows in the left panel the EDF of NS sample in black, together with the CDF of three mentioned models used for tests calculations. As we can see, the unimodal distribution (blue) fits well the position of mean but is bad in adjusting the tails, while the bimodal (red) and trimodal (green) curves provide better fits along the whole distribution. Right panel shows the PDF of all models together with the sample histogram. Although the trimodal model has a p-value similar with the bimodal case, it does not show the expected behaviour, with three distinct modes. This graphical argument is also relevant to decide for a model against other, so in this case the bimodal distribution stands as more convenient.

As stated above, hypothesis tests help to gather an intuitive comprehension of the problem, but are sensitive to the parameter values and are inconclusive, specially for small samples. A Bayesian analysis can provide stronger conclusions for this problem.

Table 3.3 - P-value of two hypothesis test for three different models

Model	K-S	A-D	Conclusion
Unimodal	0.025	0.032	Reject
Bimodal	0.971	0.990	Do not reject
Trimodal	0.974	0.953	Do not reject

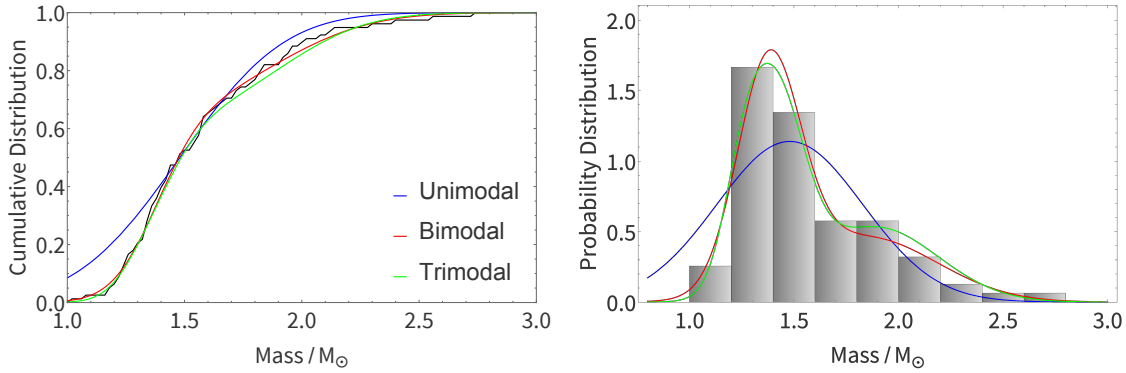

Figure 3.2: LEFT: The black curve represents the EDF of sample, while the blue curve is the CDF of an unimodal distribution, the red curve is the CDF of a bimodal distribution and in green is the CDF of a trimodal distribution. As can be noted the blue curve provides a good fit to the mean position, but is quite bad in adjusting the tails. RIGHT: The histogram of observed masses is shown, together with PDF of the 3 mixture models. Although the p-value of 2 and 3-component models are similar, the three peaks of the last one are not clearly identified, even if the binning is reduced.

3.3.2 Bayesian analysis

To proceed with the Bayesian analysis a hierarchical model is used, where the *posterior* distribution of a set of parameters ($\boldsymbol{\theta}$), marginalized over individual masses ($\mathbf{d} = \{\mathbf{d}^i\}$), is given by:

$$P(\boldsymbol{\theta}|\mathbf{d}) \propto P(\boldsymbol{\theta}) \prod_{i=1}^{N} \int P(\mathbf{d}^i|m_p^i) P(m_p^i|\boldsymbol{\theta})\, dm_p^i. \tag{3.27}$$

The $P(\boldsymbol{\theta})$ is the *a priori* distribution for each model parameter, while $P(\mathbf{d}^i|m_p^i)$ is the distribution of individual masses. We assumed the individual masses of observed pulsars to follow Gaussian distributions, with the mean and standard deviations provided in Table A.1. For example, the PSR 2S 0921-630 was reported to have a mass of $1.44 \pm 0.10\ M_\odot$ (Steeghs and Jonker, 2007), so we assume it to follow a normal distribution $\mathcal{N}(1.44, 0.10)$, and so on.

The model likelihood, $P(m_p^i|\boldsymbol{\theta})$, is assumed to be a truncated n-component Gaussian mixture model:

$$P(m_p^i|\boldsymbol{\theta}) = \sum_{j=1}^{n} r_j \frac{\mathcal{N}(m_p^i|\mu_j, \sigma_j)}{\int_{m_{min}}^{m_{max}} \mathcal{N}(x|\mu, \sigma) dx}, \tag{3.28}$$

again with $\sum_j^n r_j = 1$ to ensure normalization. The set of model parameters used is $\boldsymbol{\theta} = \{\mu_j, \sigma_j, r_j, m_{max}\}$, with $j = \{1, n\}$.

As a first step we implemented the `Gaussian Mixture Model` package (Pedregosa et al., 2011), in order to compare models with 1 to 4 Gaussian components. Since there is no astrophysical reason to believe that more than 3 classes of NS might exist, we did not

considered more complex models. Relevance has been assessed through the usage of BIC (Schwarz, 1978) and AIK (Akaike, 1974), as shown in Fig. 3.3. As we already mentioned, lower values of BIC and AIK indicate the most likely hypothesis. BIC results clearly favors $n = 2$, whilst AIK does not allow a firm conclusion between models with two and three components. It is common to find many works that base their results in only one model selection method, but as we mentioned is indeed recommended to use several different methods, whether *internal* or *external*. For this reason, we also used an external validation method based on the shape of marginalized distribution of pulsar masses. In agreement with the frequentist approach we discussed in the previous section, in the case $n = 3$ we can not clearly distinguish three modes, and the marginalized distribution of pulsar's masses resembles a bimodal behaviour. For now on, we assume $n = 2$ as a fiducial robust distribution.

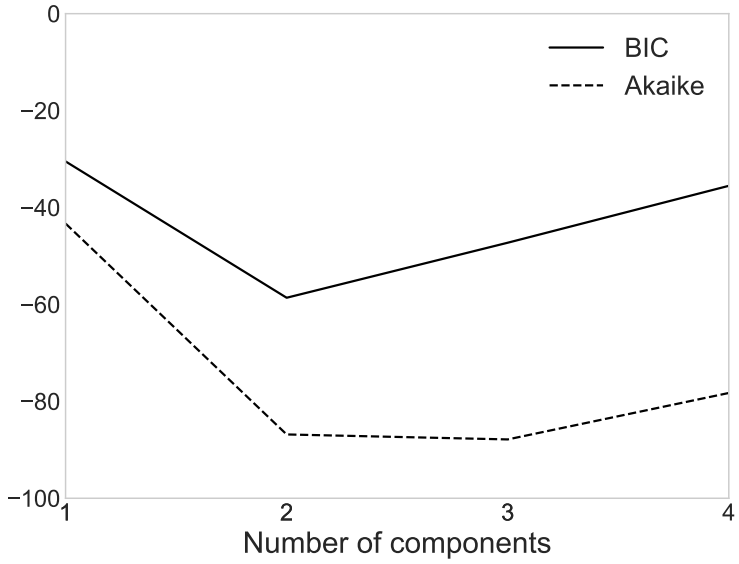

Figure 3.3: BIC and Akaike scores for a Gaussian mixture with different number of components. Lower values of both quantities indicate a better fit in the modeling. It is important to emphasize that the number of components in a model is normally accompanied by a theoretical reason, which in this case points to a maximum of three components until the moment. BIC favors a model with two Gaussians while Akaike does not provide a firm conclusion.

3.3.2.1 *Marginalized posterior distributions*

In the sequence we implemented MCMC algorithm using `pystan`, a python interface to `STAN`[5] (Team et al., 2020, STAN, 2020). In the appendix B we detail the assumptions made to run the models, as the number of chains and iterations, prior's distributions and etc.

The summary of marginalized *posterior* distributions sampled for each model parameter in the truncated scenario (described by Eq. 3.27 and 3.28) is given in Table 3.4. First column provide us the mean value of the parameter, followed in the second column by its respective standard deviation. Third columns gives the *highest posterior density* interval with 94% probability, this quantity constrains the shortest interval of masses with a given probability. The corner plot in Fig. 3.4 shows all the one and two dimensional projections of the posterior probability distributions of our parameters. The diagonal shows the marginalized posterior distribution of each parameter individually, while below the diagonal we can see the covariance between pairs of parameters in the form of marginalized two dimensional distributions.

Table 3.4 - Summary of marginal *posterior* distribution of each parameter from a bimodal right-truncated model, with the mean value in the second column, followed by respective standard deviation and the highest posterior density in fourth and fifth columns defining the lowest interval that comprises 94% of probability.

	mean	sd	94% HPDI
r_1	0.533	0.090	0.358-0.695
r_2	0.467	0.090	0.305-0.642
μ_1	1.347	0.023	1.304-1.389
μ_2	1.796	0.077	1.652-1.937
σ_1	0.085	0.020	0.049-0.122
σ_2	0.258	0.056	0.147-0.362
m_{max}	2.600	0.386	1.890-3.291

In agreement with previous analysis available in literature, our sampling results in a bimodal distribution with a class of NS's clustered around $\sim 1.35\ M_\odot$, and a second group at $\sim 1.8\ M_\odot$, with a preponderance of objects in the first class. Contrary to results found in Alsing et al. (2018) and Shao et al. (2020), our maximum mass has a mean value of

[5] Stan is a state-of-the-art platform for statistical modeling and high-performance statistical computation, which provides full Bayesian statistical inference with MCMC sampling.

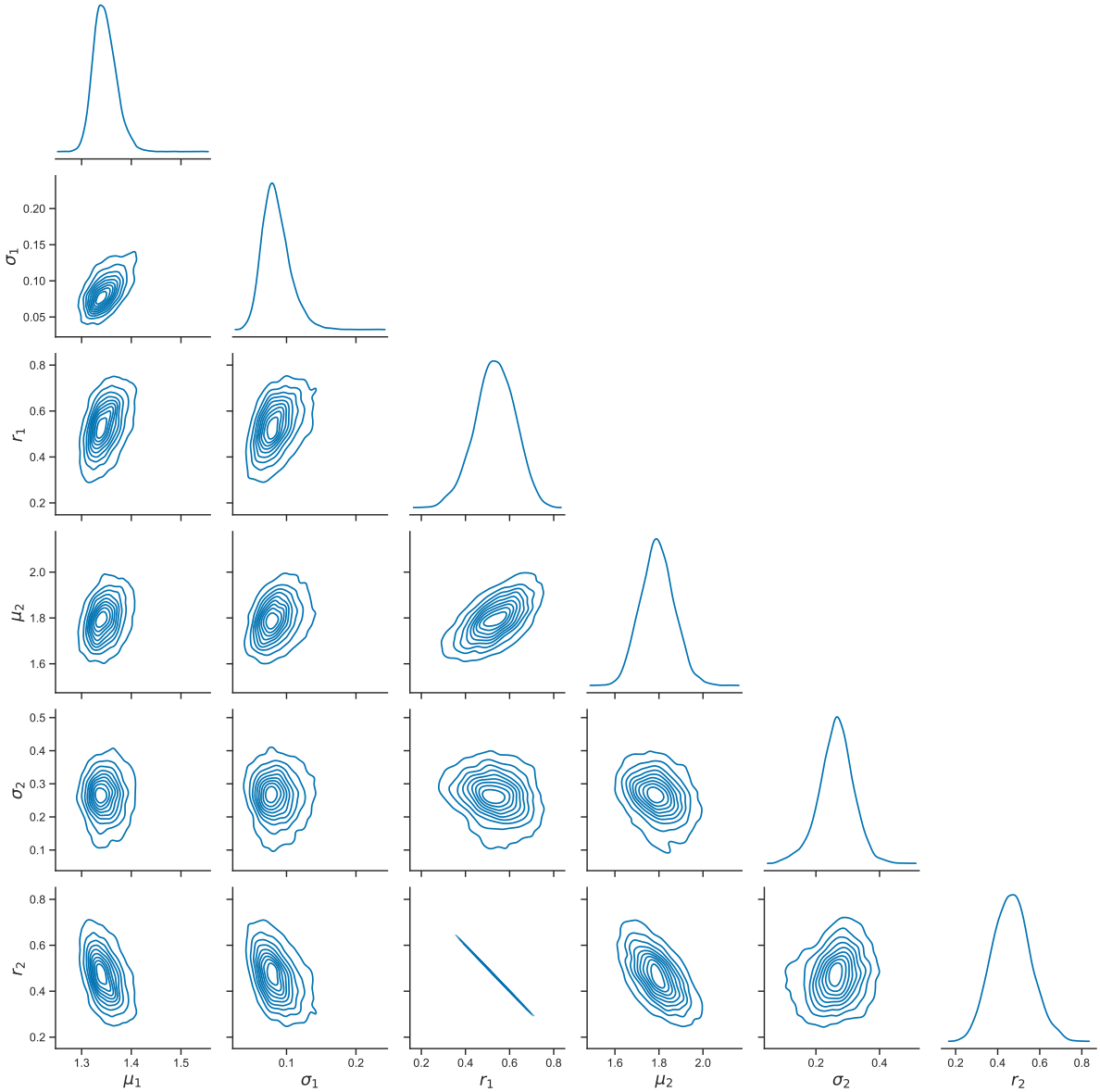

Figure 3.4: The diagonal shows the marginalized distribution for all parameters (θ) in the truncated bimodal gaussian distribution.

$m_{max} \simeq 2.6 \pm 0.4\ M_\odot$ and, as shown in Fig. 3.5, its marginal *posterior* distribution has a much broader shape compared with the works we mentioned.

This broad behaviour is somewhat expected. The posterior distribution is a balance between the information stored in likelihoods and *a prioris*. Given a strong likelihood, the *a priori* will have a small impact over the posterior distribution, such that a change of *a priori* will barely change the result. On the same way, if the degree of information about a specific parameter in the likelihood is low, the *a priori* will play a key role on the marginalized distribution of this parameter. Have we set narrower (stronger) priors, this would be imprinted in the marginal *posterior* distribution. In Section 3.3.2.4 we discuss why our result differs significantly, and why it cannot be treated as a flaw.

To check the robustness of results we investigated how an individual measurement with high mass can influence the marginalized distribution of m_{max}. The dashed line in Fig. 3.5 is the marginal distribution when we exclude PSR J1748-2021B from the sample, which has $m = 2.74 \pm 0.21\ M_\odot$. On the other hand, we check the impact of adding to the total sample a new data consistent with the lightest component of GW190814, with $m = 2.59 \pm 0.08\ M_\odot$, shown by the dotted line. As we can see in both cases, the marginalized distribution barely changes. Finally, we verified the impact of changing the masses of PSR B1957+20, J1048+2339, J1555-2908, J2129-0429 by the values obtained from γ-ray observations, listed in Table 3.1. Since the only value that changes considerably is for B1957+20, we did not expected a significant change, as confirmed by the grey dot-dashed line in Figure 3.5

3.3.2.2 Right-tail behaviour

In both works of Alsing et al. (2018) and Shao et al. (2020) an evidence for a sharp cut-off on the maximum mass was found (see Fig. 2 of both works). This implies that the right-tail of the distribution (where $m \geq 2\ M_\odot$) has a non-negligible probability for mass values right before m_{max}, and suddenly vanishes above it. The broad shape of m_{max} in our result has a consequence in the posterior sample of pulsar's mass. No sharp cut-off is observed. Instead, we have a smooth decrease of probabilities in the right-tail, until it achieves the limit value, m_{max}.

Figure 3.6 shows in light grey lines draws of 1000 posterior samples of pulsar mass distribution. The *maximum posterior probability* (MAP), in black, is the estimate that equals the mode of the *posterior* distribution. In blue we have the average mass distri-

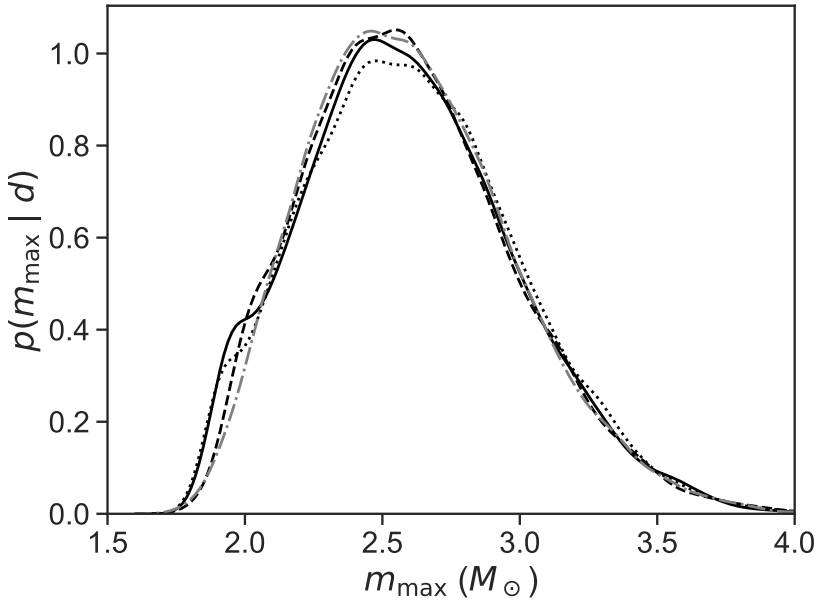

Figure 3.5: Marginal *posterior* distribution of m_{max} and a test of the algorithm sensitivity to the most massive source. Solid line is the result for complete sample (112 NS's), while dashed line is the result when removing PSR J1748-2021B and dotted line is the result for complete sample plus a pulsar consistent with the $2.59 \pm 0.08\ M_\odot$ component of GW190814. The grey dot-dashed curve is the result of substituting the masses listed at Table 3.1

bution. This plot allows us to have a visual intuition of uncertainties in each parameter, summarized in Table 3.4. Although some grey lines do show a sharp cut-off, the MAP and average distributions do not (blue and black curves).

Due to the differences found in comparison to previous works a question arises: should we expect a sharp cut-off for relatively higher thresholds? We look for any relation between the m_{max} value and the right-tail behaviour. Figure 3.7 shows in grey solid lines two empirical cumulative distribution function, which assigns a probability for each datum, one for original sample (step-shaped curve) and the other for a synthetic sample with 11200 points to take into account the uncertainties of mass. The black dashed curve is a truncated Gaussian mixture that resembles our mean result presented in Sec. 3.3.2.1, with $m_{max} = 2.59$. Dotted curves are reconstructions of the posterior mean distribution from Alsing et al. (2018) with different values of truncation, starting with the original one in 2.12 $M_\odot$, followed by 2.22 $M_\odot$, 2.32 $M_\odot$ and 2.42 $M_\odot$, from left to right. The right panel of Figure 3.7 gives a zoom in the region of accumulated probabilities between 90% and 100%.

As we can see in the zoom, there is an apparent trend on the right-tail behaviour depen-

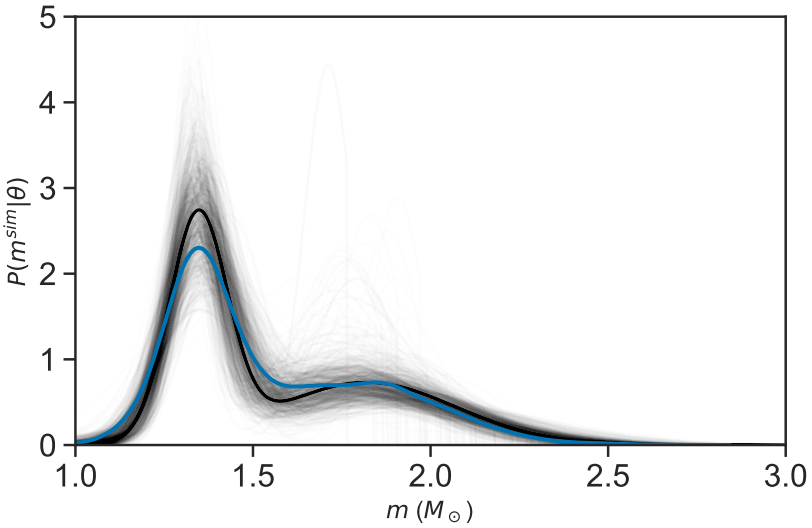

Figure 3.6: Grey lines represent 1000 posterior samples drawn from truncated model summarized in Table 3.4. The blue curve is the posterior mean of these synthetic samples and the black line is the maximum *a posteriori* distribution.

ding on the mass threshold. For lower thresholds, namelly 2.12 and 2.22, the cumulative distribution presents a kind of "knee" when it achieves the value of 1. This is translated in a sharp cut-off in the probability distribution function (PDF). As the threshold value increases, smoother is the way in which the cumulative distribution approaches 1.

If a sharp cut-off was expected for large values of m_{max}, the probability to observe masses close to it would increase, compared with a case where the sharp cut-off is absent. This result might indicate that, if these "ultra-massive" NSs really exist in Nature, they are very rare. This is in agreement if the fact that, according to the initial mass function (IMF), the number of progenitor stars reduces as we increase masses. Consequently, the number of very heavy NSs must be low.

3.3.2.3 Posterior Predictive Check

An important step in Bayesian analysis is to check if predictive simulated data look similar to observed data, *i.e.*, if we detect new observations drawn from the posterior distribution, we want to know if they will be compatible with current observed sample. A discrepancy might reveal a misfit. This analysis is called *posterior predictive check* (PPC) and, one of the ways to proceed with it is to graphically compare summaries of real data with summaries of simulated data. But in addition, it can be useful to quantify the level

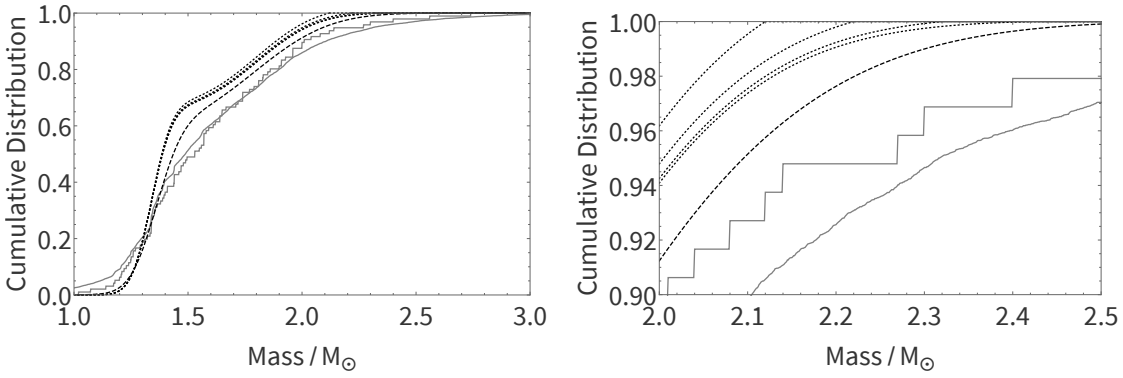

Figure 3.7: Cumulative distribution function to investigate the behaviour of right end tail depending on truncation parameter. Solid gray curves are the empirical cumulative distribution function which assign a probability for each datum, where the step-shaped curve is the EDF for original sample with 112 points and the other is the EDF for a synthetic sample with 11200 points that take uncertainties into account. Dashed line is a Gaussian mixture built from our posterior mean distribution summarized at Table I of main text. Dotted curves, on the other hand, are reconstructions of posterior mean distribution obtained in Alsing's work, but with different values of m_{max}. From left to right, truncation points are set as 2.12 $M_\odot$ (original value), 2.22 $M_\odot$, 2.32 $M_\odot$ and 2.42 $M_\odot$. There is a trend of an increasingly smooth fall as the maximum mass increases. Moreover, Alsing's result no longer matches the updated sample.

of discrepancy by defining a "test quantity" (T), which can be, for example, the mean. A Bayesian p-value is then computed as the probability that the test quantity of simulated data, T^{sim}, exceed the T value for real data:

$$p = P(T(m^{sim}) > T(m)|m). \tag{3.29}$$

After the detection of GW170817 several works were published where the maximum mass allowed for NS's is derived (Ai et al., 2020; Rezzolla et al., 2018; Margalit and Metzger, 2017; Ruiz et al., 2018; Shibata et al., 2019). All these analysis resulted in maximum masses significantly lower than the m_{max} we found from the sample of galactic binaries with NSs. To quantify if the values derived from GW data are compatible with the posterior distribution of pulsar masses sampled from the galactic binaries, we apply a PPC.

As our goal is to investigate the maximum of the distribution, we performed a new MCMC sampling from a non-truncated Gaussian mixture, to avoid any influence on the maximum. The only difference with the previous model is that now $P(m_p^i|\boldsymbol{\theta}) = \sum_j^n r_j \ \mathcal{N}(m_p^i|\mu_j, \sigma_j)$. In Table 3.5 we summarize the mean and standard deviation of each model parameter.

We used results shown in Table 3.5 to generate, through `MATHEMATICA`Wolfram (2020), 100.000 posterior predictive distributions following a Gaussian mixture with $n = 2$. Further-

Table 3.5 - Summary of marginal *posterior* distribution of each parameter in the non-truncated bimodal model. These results were used to generate 10.000 synthetic bimodal Gaussian distributions.

r_1	r_2	μ_1	μ_2	σ_1	σ_2
0.454 ± 0.094	0.546 ± 0.094	1.345 ± 0.029	1.785 ± 0.071	0.097 ± 0.027	0.308 ± 0.039

more, we defined the test quantity, T, as the amount of elements in the observed sample with masses higher than a specific value, named m_{max} to illustrate our goal to examine the maximum mass. The p-value results from the number of times that $T^{sim} > T$. The left panel at the top of Figure 3.8 give us an analogue to the probability of, in future observations, detect objects with $m > 2.09\ M_\odot$.

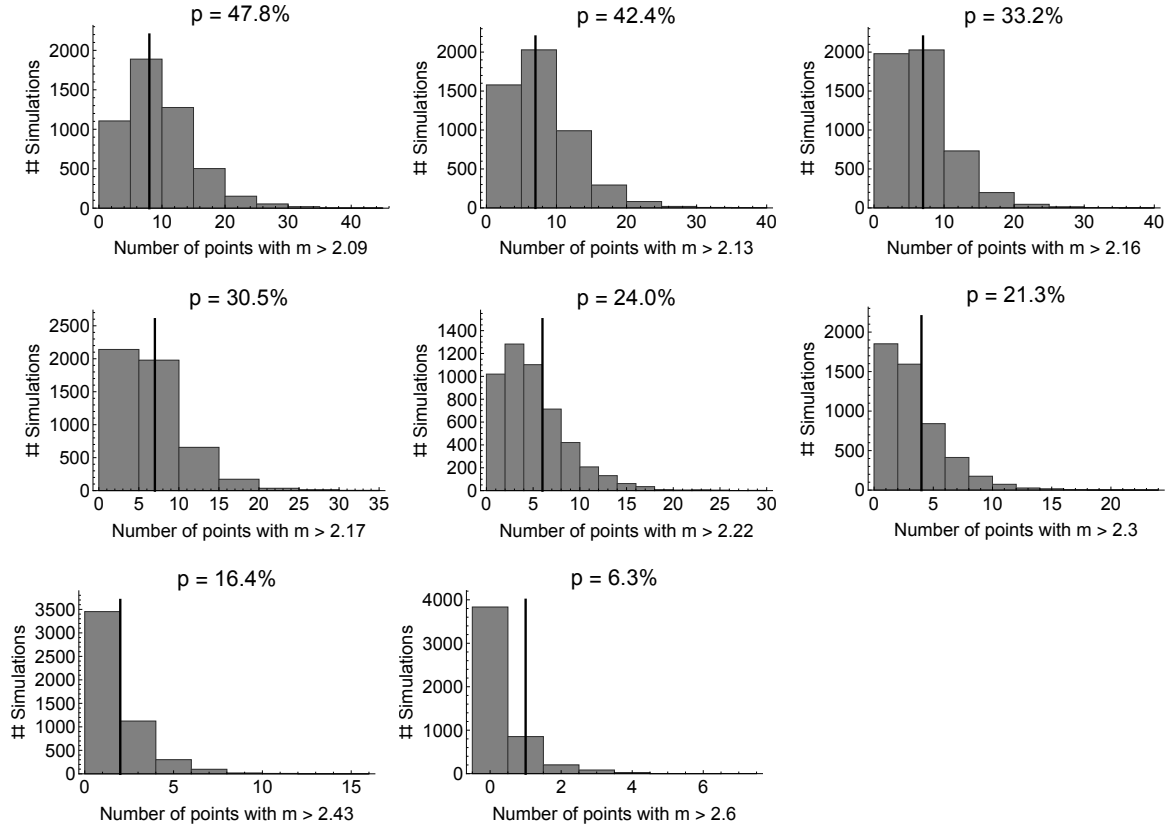

Figure 3.8: Posterior predictive check on two-Gaussian model without truncation. The purpose is to investigate the upper tail of distributions. High p-values indicates that values higher than the one specified in the label are very common, thus they cannot be pointed as valid thresholds. The adopted m_{max} from NS-NS mergers are, from left to right and top to bottom: Ai et al. (2020) with $2.09^{+0.11}_{-0.09}\ M_\odot$; Shao et al. (2020) with $2.13^{+0.08}_{-0.07}\ M_\odot$; Rezzolla et al. (2018) with $2.16^{+0.17}_{-0.15}\ M_\odot$; Margalit and Metzger (2017) with $2.17\ M_\odot$; Ruiz et al. (2018) with $2.16 - 2.28\ M_\odot$; Shibata et al. (2019) with $2.3\ M_\odot$; Ai et al. (2020) with $2.43^{+0.10}_{-0.08}\ M_\odot$. Last panel represents our result summarized at Table 3.4. We used the mean value of each referenced work, since they cover the whole range of high masses reasonably well.

3.3.2.4 A comparison with Alsing's treatment

As we discussed in Sec. 3.1, the best determined masses of pulsars are those where relativistic effects takes place and two or more post-keplerian parameters are observed. In these cases both works of Alsing et al. (2018); Shao et al. (2020) consider individual masses to be normally distributed, as we made. Otherwise, only lower/upper limits can be set from observations to the pulsar masses. If, despite of the mass function, only the $\dot{\omega}$ is constrained, the system total's mass can be determined. In this case, the individual likelihood is given by:

$$\begin{aligned} P(d|m_p) &\propto \int\int P(d_t|m_p, m_t, i) dq\ dm_t \\ &= \int exp\left(-\frac{(m_t-\mu_t)^2}{2\sigma_t^2}\right) \frac{m_t^{4/3}}{3(m_t-m_p)^2 f^{1/3}\sqrt{1-\frac{f^{2/3}m_t^{4/3}}{(m_t-m_p)^2}}} dm_t. \end{aligned} \tag{3.30}$$

Finally, if only the mass-ratio can be determined from phase-resolved optical spectroscopy, the pulsar mass likelihood assumes the form:

$$\begin{aligned} P(d|m_p) &\propto \int\int P(d_q|m_p, q, i) di\ dq \\ &= \int exp\left(-\frac{(q-\mu_q)^2}{2\sigma_q^2}\right) \frac{(1+q)^{4/3}}{3f^{1/3}m_p^{2/3}q^2\sqrt{1-\left(\frac{f}{m_p}\right)^{2/3}\frac{(1+q)^{4/3}}{q^2}}} dq. \end{aligned} \tag{3.31}$$

The main assumption to derive equations 3.30 and 3.31 is that $\cos i$ is isotropically distributed, *i.e.*, is subject to a uniform *a priori* so that i can assume any value between $0° - 90°$. The main source of uncertainty in mass measurements from Kepler's law is the orbital inclination angle, i, where:

$$m_p \propto \frac{1}{\sin^3 i}. \tag{3.32}$$

Although it is difficult to determine this parameter precisely, constraints can be set from the orbital geometry of the binary system, such as through the presence or not of eclipses.

In this section we investigate the impact of this treatment in the marginal posterior distribution of m_{max}. In order to do that, we first reproduce their analysis using Eq. 3.30 and 3.31 when individual masses are not well determined. In Table 3.6 we compare the individual mass inferred from MCMC sampling (second and third columns) for a few systems, with the best-fit mass determined by observations.

In the sequence, we change the treatment for systems listed in Table 3.6, since they are potentially the most massive ones ($\geq 2.0\ M_\odot$) among those systems with individual

Table 3.6 - Individual pulsar mass of systems listed in this table are sampled from equations 3.30 and 3.31, as functions of the total mass (second column) or mass ratio (third column). They are particularly interesting since their masses derived from observations (fourth column) are $\geq 2.0\ M_{\odot}$.

Pulsar	m_{mt}	m_q	$m_{observations}$
B1957+20	-	1.06 - 2.02	2.40 ± 0.12
J1311-3430	-	1.17 - 2.07	2.22 ± 0.10
B1516+02B	1.26 - 2.23	-	2.08 ± 0.19
J1748-2021B	1.22 - 2.25	-	2.74 ± 0.21

likelihoods in the form of equations 3.30 and 3.31, and treat them in terms of normal likelihoods to check for the impact it has on the inference of m_{max}.

By reproducing the approach from Alsing et al. (2018) and Shao et al. (2020), we obtain the marginalized posterior distribution shown in the left panel of Figure 3.9, with a mode at $\sim 2.2\ M_{\odot}$. If we keep their modelling with 3 types of likelihoods, but only for systems B1957+20, J1311-3430, B1516+02B and J1748-2021B we assume the likelihood to be gaussian, with mean and standard deviation given at the fourth column of Table 3.6, the shape of marginalized posterior distribution of m_{max} changes considerably, as seen on the right panel.

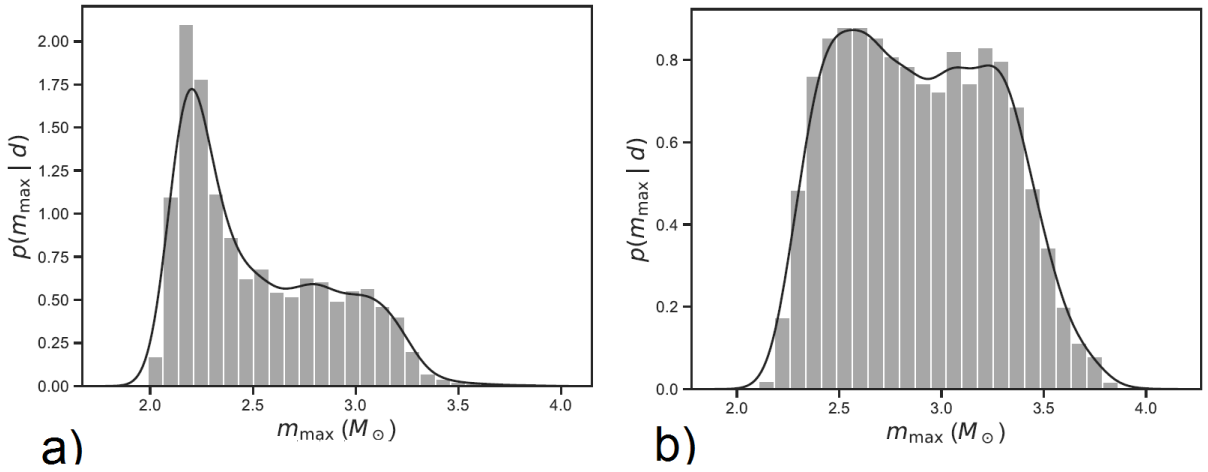

Figure 3.9: Marginalized *posterior* distributions of maximum mass parameter. Left panel a) shows the result assuming q and m_t based likelihoods for all pulsars mentioned in Table 3.6. Right panel b) shows the result when assuming the likelihood of these systems to follow gaussian distributions with values listed in the fourth column of Table 3.6.

As we showed, the prior assumption on orbital inclination angle has a large impact on the determination of the mass threshold, and needs to be treated carefully. The ideal case

would be to construct the likelihood including the parameter i for each particular system, where values are given by observations. Furthermore, as this treatment underestimate the individual sampled masses, it has as a consequence a narrower marginal distribution for the maximum mass parameter, which in turn leads to the presence of a sharp cut-off on the posterior mass distribution.

3.4 Conclusions

For decades after the first pulsar mass measurement it was believed unlikely that they could deviate substantially from $1.4\,M_\odot$, a value inferred from a few Double Neutron Star systems (Finn, 1994) and somewhat expected from evolutionary grounds. The continuous search and pulsar surveys exposed a larger spread in masses, but the maximum mass was not expected to reach values close to 2 $M_\odot$. This paradigm was initially broken by the discovery of PSR J1614-2230 with $m = 1.97 \pm 0.04$ $M_\odot$ (Demorest et al., 2010; recently updated to $m = 1.94 \pm 0.03$ [Shamohammadi et al., 2022]). Later, the mass measurement of PSR J0740+6620 ($m = 2.08 \pm 0.07$ $M_\odot$) confirmed that the true limit for NS masses is above two solar masses. However, there is still a tension about whether the threshold is below or above $2.2 - 2.3$ $M_\odot$, and a handful of candidates suggesting even higher values.

The detection of gravitational wave signals from the merger of compact objects strengthened the tension. Predictions for the confirmed double NS merger, GW170817 (Abbott et al., 2017b), firstly resulted in mass thresholds in the interval between 2.1 and 2.3 $M_\odot$ (Ai et al., 2020; Shao et al., 2020; Rezzolla et al., 2018; Margalit and Metzger, 2017; Ruiz et al., 2018; Shibata et al., 2019), although the values obtained would be different if differential rotation, instead of rigid, was assumed for the merged unstable object. For GW190814, a second component with ~ 2.6 $M_\odot$ may have been a NS if the static mass threshold (applied to a slow or non-rotating NS) happens to be ≥ 2.5 $M_\odot$. An analysis made by the LIGO team (Abbott et al., 2021) of the BBH population found the GW190814 to be an outlier, *i.e.*, it is likely from a NS-BH merger. In addition, from analysis of the available LIGO-Virgo NS-BH events, the maximum mass of non-spinning NS was found to be $2.7^{+0.5}_{-0.4}$ $M_\odot$ (Ye and Fishbach, 2022), a completely independent piece of evidence to mount the puzzle of the maximum mass value.

In this chapter we proceed with a mass distribution analysis of galactic binary systems

with at least one NS. As we showed both in frequentist and Bayesian approaches, the sample is still consistent with the existence of two different classes of NSs. The first one is centered around $\sim 1.35\ M_{\odot}$ which groups those formed from electron capture supernovae of *OMgNe* cores and those formed from the core collapse of lighter Fe cores. The second class is clustered around $1.8\ M_{\odot}$, with greater dispersion and smaller amplitude. Nowadays we know that NSs belonging to this class can be born more massive naturally, althought accretion can also be present, as is the case of spider systems (Horvath et al., 2020). A larger sample of mass measurements is still necessary to reveal whether there is indeed a clustering of objects around two or more preferred values, with substantial differences between groups, or whether the population behaves more like, for example, a power law.

By modeling a truncated mixture of two Gaussians, we were able to infer a threshold parameter, namely the maximum mass m_{max}. The marginal posterior distribution, shown at Figure 3.5, exhibits a broad behaviour, with a mean at $\sim 2.6\ M_{\odot}$, a relatively higher value than expected from previous analysis of the galactic population (Alsing et al., 2018; Shao et al., 2020). As we discussed in Section 3.3.2.2, the absence of a sharp cut-off at the posterior distribution of pulsar masses (Figure 3.6) is a reflex of the broader shape of m_{max}. Furthermore, as a higher value is expected for the mass threshold, a sharp cutoff is less likely to be present (Fig. 3.7).

In the sequence we generated predictive distributions of NS's masses, to simulate future observations, and quantified how probable it is to find within these distributions NS's with masses above a threshold value. For these values we used the maximum masses inferred from different works based on the GW170817 (Ai et al., 2020; Rezzolla et al., 2018; Margalit and Metzger, 2017; Ruiz et al., 2018), together with the m_{max} we inferred. This analysis allow us the verify if the maximum mass inferred from this particular extragalactic event is consistent with the galactic binary population. The result also shown to be consistent with a higher maximum mass, supporting the existence of NS's with extreme masses, like the less massive component at GW190814.

Lastly, our model assumes all individual pulsar masses likelihoods to be Gaussian. The mean and standard deviations used are those reported in Table A.1, derived from observations by placing geometric constraints to the system orbit. The treatment of Alsing et al. (2018) and Shao et al. (2020) distinguish from ours in this matter. For systems where individual masses are not well determined, they consider the likelihoods to be given by Eqs.

3.30 and 3.31, assuming a uniform *a priori* to $\cos i$. As we showed in Sec. 3.3.2.4, differences between treatments are indeed responsible for the significant differences we found for m_{max}, so that their results underestimate values, and disfavor the existence of extremely massive NSs.

It is important to highlight that this is the maximum inferred from the NS binary population of galactic systems. As we mentioned, the picture can be different for isolated NS's, since the range of progenitor leading to ECSN, for example, is different (Podsiadlowski et al., 2004) and accretion phases are not present. Furthermore, metallicity also plays a role, and progenitor systems of GW events at higher redshifts can be somewhat distinct from our local population. Efforts to increase the number of mass measurements from NS's are deeply desirable.

Chapter 4

Double Neutron Star Systems

The detection of gravitational waves from the merger of two NSs opened a new era in the multimessenger and multiwavelength astronomy, and placed the Double Neutron Star systems (DNSs) in a privileged role. DNS mergers in distant galaxies, caused by the slow but ever increasing loss of orbital energy due to gravitational wave (GW) emission, were, for many decades, thought to be at the origin of short gamma rays bursts (GRBs), an idea confirmed when the gravitational wave signal from such merger was detected by LIGO at the same time as a faint nearby GRB (Abbott et al., 2017b). These DNS mergers are thought to create large percentages of the heaviest chemical elements in our Universe (Safarzadeh et al., 2019), and can also help to resolve the state of ultra-dense matter and the Hubble tension (Abbott et al., 2017a). Furthermore, DNSs touch many different areas of astrophysics and fundamental physics. Radio timing can yield some of the most precise tests of gravity theories (e.g., Kramer et al., 2021), especially tests of its radiative properties, which are impossible in our Solar System. The many quantities measured from timing - the position and proper motion, the spin characteristics, the orbital characteristics and the masses - provide important clues for their formation (Tauris et al., 2017), which in turn provide important constraints on the physics of supernovae.

All these lines of research imply that is is vitally important to understand not only the formation of DNSs, but also their properties at merger. In this Chapter we summarize the current understanding of the formation and merger of DNSs, check for consistency between theory and the most up-to-date sample, and introduce an online living catalogue [1] built to facilitate the access to information about DNSs. The catalogue might help the scientific community to establish relations between the galactic and extragalactic sample, with the

[1] `https://donutss.onrender.com/`

aim to improve searches of GW signals to help solve the most intriguing problems related with neutron star physics. All the discussion will be present in a paper Rocha *et al.* that is in preparation.

4.1 Formation of DNS systems

A standard scenario for the formation of DNS systems in the galactic disk emerged from a series of theoretical works, with an endorsement from population synthesis studies, and we describe it in the following paragraphs [2]. The complete scenario is illustrated in Fig. 4.1.

The system starts with two OB-stars at the *zero age main sequence* (ZAMS), massive enough to terminate their lives in a core-collapse SN. For *primary*[3] stars, the initial mass must be in the range $\sim 8 - 12\ M_\odot$, while for the secondary the range is $\sim 5 - 7\ M_\odot$ since they accrete matter from the companion. These intervals, however, depends on the metallicity and can be as high as 15 $M_\odot$ for primaries with solar metallicity. To enable formation of a tight DNS, the components must be in a system initially close enough to ensure interactions via stable or unstable mass transfer.

The primary star evolves until it fills its Roche Lobe (RL) and starts transferring matter to the secondary. If the transfer is unstable, it will undergo a *common envelope* (CE) phase from where they can end up merging into a single star, or the envelope can be ejected before the stars coalesce. This last path will leave a stripped primary orbiting a MS star, with an orbit that can be significantly tight. Otherwise, a stable transfer will have a similar destiny. It will end with a He star and a massive companion that accreted a large fraction of matter loosed from the primary star. The accretion leads to a spin-up of the companion and a net widening of the orbit. The He star continues evolving until it explodes into a SN. If the binary system remains bound, it will eventually become observable as a *high-mass X-ray binary* (HMXB), i.e., a NS orbiting a luminous and massive companion star. Before this stage, the binary can also be seen as a radio pulsar orbiting a OB-star.

[2] DNS systems in Globular Clusters (GC) might be formed by secondary exchange encounters, and consequently all information about the past evolution is lost. These systems are not taken into account on the study of the recycling process and impact of the second SN.

[3] The primary star is usually defined as the most massive at the begin of evolution, since it will fill its Roche Lobe before and consequently form the first remanescent object.

The secondary expands and initiate its Roche Lobe overflow (RLO) during the HMXB stage. The large mass-ratio between the OB-donor star and the accreting NS will cause the orbit to shrink and lead to a dynamical unstable transfer. For wide systems, the timescale on which they become dynamically unstable can be as short as a few 100 yr, leading to the formation of a CE phase. Drag forces from the motion of the NS inside the giant star's envelope causes dynamical friction, and can led to an extreme loss of orbital angular momentum and even the ejection of the hydrogen-rich envelope, resulting in a much closer orbit.

Systems surviving the CE phase will consist of a NS orbiting a He star and, depending on orbital separation, a Case BB RLO can occur. This additional phase of mass transfer can be relatively long and is responsible for *recycling* the NS reducing significantly its spin period, and allowing an extreme stripping of the He star prior to its explosion. If the system survive to this second SN, again depending on the orbital separation and kick magnitude, it will form a DNS. This second SN is usually associated with an *ultra-stripped SN* (USSN), since the exploding star was stripped before the collapse and the amount of ejected matter is much smaller, as well as the energy of the explosion. If the post-SN orbital period is short enough, the system will eventually merge due to GW radiation, with a final remnant that can be a BH or even a NS, depending on their maximum mass.

A few aspects of the DNS formation are yet uncertain, including specially the CE evolution followed by the spiral-in of the NS, as well as the momentum kick imparted onto newborn NSs. In first place, it is difficult to predict the final post-CE separation after the ejection of the companion envelope given that it is difficult to distinguish the separation between ejected envelope and the remaining core. In second place, the magnitude and direction of kick imparted onto a NS during a SN needs more investigations, and we will provide a brief discussion in this topic later in this Chapter.

Although this is the standard scenario to form DNS systems, it is not necessarily the only one. In analogy with the whole sample of NSs, a standard scenario was also believed to be unique, but nowadays we know that many possibilities exists, as we already discussed. There are DNS, for example, where the radio source is the non-recycled component, and assume only one formation without further evidences can be misleading.

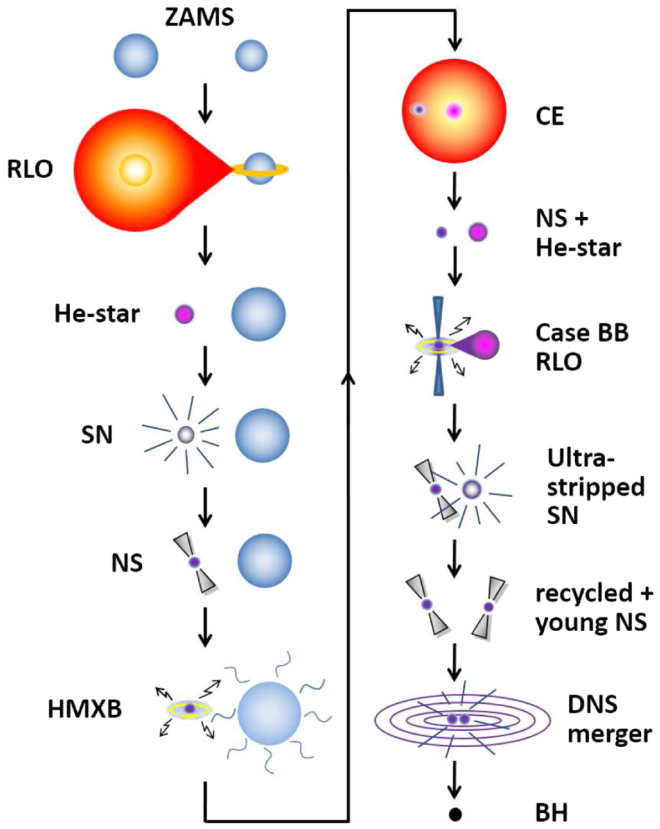

Figure 4.1: Standard formation scenario proposed to the formation of a DNS system that will merge within a Hubble time. Look at Sec. 4.1 for a description of each stage. Extracted from Tauris et al. (2017).

4.2 DNS population and main characteristics

Compared with the total sample, DNS systems seem to present a smaller spread over masses, as we can see at Fig. 3.1. However, it is important to note that a significant fraction can have an asymmetric mass-ratio (Ferdman et al., 2020), like PSR J0453+1559 and PSR J1913+1102. The recycling process is expected to increase the mass of the first-born pulsar, and as a consequence, they present masses slightly larger than the non-recycled companions. In Fig. 4.2, we plotted a histogram and a diagram of DNS masses where purple dots represents recycled components, while green dots are for the non-recycled and the blue dots for the companion stars whose nature is not confirmed, i.e., they can also be heavy WDs.

The amount of mass accreted by the first-born NS was calculated in (Tauris et al., 2017), for each possible stage during the binary evolution - wind accretion in the HMXB stage; CE and spiral-in evolution; wind accretion from the helium/Wolf-Rayet star; case BB RLO; shell impact from the second SN - and was found to be $\Delta M_{NS} < 0.02\ M_{\odot}$. This provide us an indicative that the observed mass of NS components in DNS systems reflects their masses at birth, with no substantial accretion. It is possible to see (histograms at the top panel of Fig. 4.2) that there is a difference of $\sim 0.1\ M_{\odot}$ between first and second-born NSs that, therefore, is associate with different conditions at the onset of SN explosions.

Despite of masses, all observed and derived quantities of DNS systems are important to understand how they are formed, including spin periods (P), their time derivatives ($\dot{P}$), surface magnetic fields (B), eccentricities (e), orbital periods (P_b), as well as kinematic properties. Any correlation between orbital parameters and the spin period, for example, carries information about the recycling process. In Table 4.1 we summarize the observed ranges of the key properties of DNSs. The complete list of DNS properties in all 27 confirmed and candidate systems can be found in Table 4.1. Some selection effects can have an influence on the observed ranges, as is the case of the orbital period, for example. For tight systems, the fast-changing Doppler shift can cause the spin period observed on Earth to change significantly within a single observation and, as a consequence, there is generally a bias against the detection of pulsars in systems with orbital periods of ~ 0.1 days or less.

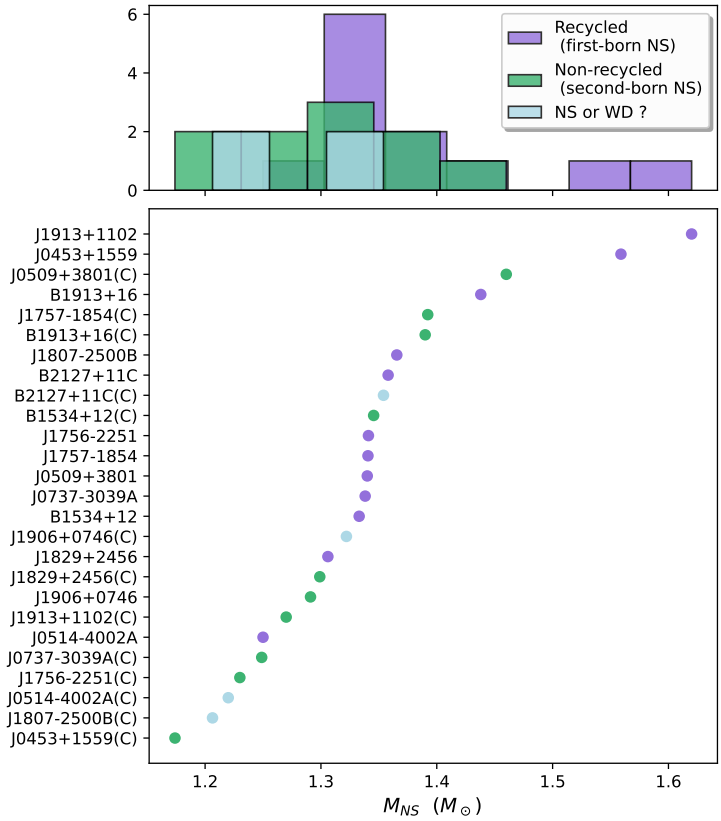

Figure 4.2: Mass diagram of galactic DNS systems where individual masses are well constrained. Recycled (or first-born) pulsars are represented by purple dots, while non-recycled (or second-born) NS's are in green. There are four systems where the companion's nature is not confirmed, so they can potentialy be a massive WD. This are represented with light blue dots. In the top panel we display the mass diagram that confirm the expectation that recycled pulsars are more massive than their companions.

4.3 Spin evolution

Fig. 4.3 shows the $(P, \dot{P})$ diagram of observed galactic DNSs including estimates for their magnetic field (B), as well as characteristic ages ($\tau = P/2\dot{P}$). As noted in the diagram, observable pulsars in DNS systems are generally the old and recycled components, since the accretion process allows them to leave the *death zone* and radiates with lower spin-down rates. Furthermore, these recycled pulsars shows weaker surface magnetic fields ($\sim 10^8$-10^{10} G) when compared with normal pulsars ($\sim 10^{11}$-10^{13} G). Albeit the reason for the field decay is usually associated with the accretion (Bhattacharya and van den Heuvel, 1991; Tauris and Van Den Heuvel, 2006), alternative hypothesis exist, such as an ambipolar diffusion previous to the accretion phase (Cruces et al., 2019).

The spin period of the recycled NS right after the DNS system is born depends on the rate and duration of the recycling process, as well as on the initial orbital separation of

Table 4.1 - Observed intervals of main properties of DNS systems

Properties of recycled (first-born) NSs	
Spin period (P)	3.9 - 185 ms
Period derivative ($\dot{P}$)	(0.027 - 20) $\times$ 10^{-18} s s^{-1}
Surface B-field (B)	(0.29 - 18) $\times$ 10^{9} G
Mass	1.25 - 1.62 $M_{\odot}$
Properties of young (second-born) NSs	
Spin period (P)	144 - 2773 ms
Period derivative ($\dot{P}$)	(0.89 - 20) $\times$ 10^{-15} s s^{-1}
Surface B-field (B)	(2.7 - 5.3) $\times$ 10^{11} G
Mass	1.17 - 1.46 $M_{\odot}$
Orbital properties	
Orbital period (P_{orb})	0.08 - 45 days
Eccentricity (e)	0.064 - 0.97
Merger time (τ_{GW})	46 Myr $\rightarrow \infty$
Systemic velocity (v_{sys})	25 - 240 km s^{-1}

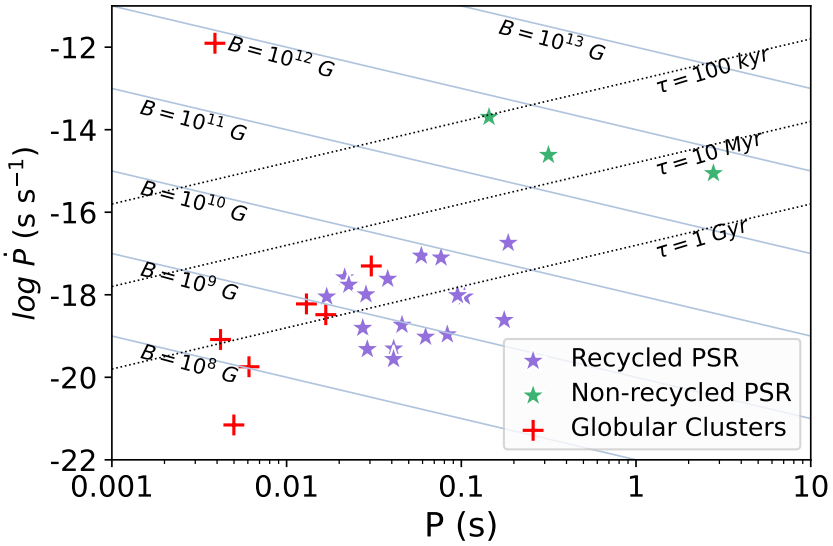

Figure 4.3: $(P, \dot{P})$-diagram of all radio pulsars in DNS systems. Solid blue lines represent constant surface dipole B-fields. Dotted black lines represent constant characteristic ages. The $\dot{P}$ values are not corrected for the Shklovskii effect. For systems in GCs, the $\dot{P}$ must also be corrected for the NS acceleration in the cluster potential.

the system. From the theoretical point of view, a close DNS progenitor system will end with a shorter spin period compared with an initially wider progenitor system. Since the companion star will be less evolved at the onset of mass transfer through its RL, the mass

transfer (recycling) phase will last longer for closer systems. Hence, a positive correlation is expected to emerge between spin and orbital periods. Such correlation is indeed present for observed DNSs as shown from a linear regression in the (logP_b, log P)-plane, Figure 4.4:

$$P = 46\ ms\ (P_b/\text{days})^{0.28}. \tag{4.1}$$

The DNS systems PSR J1811-1736 and PSR J1930-1852 are two good examples of wide orbits with less efficient recycling. In both cases, the spin period is higher than $P > 100\ ms$ and their orbital periods are of 18 and 45 days, respectively. On the other side PSR J1946+2052 has a spin period of 17 milliseconds with an orbital period lower than 2 hours, confirming the tendency.

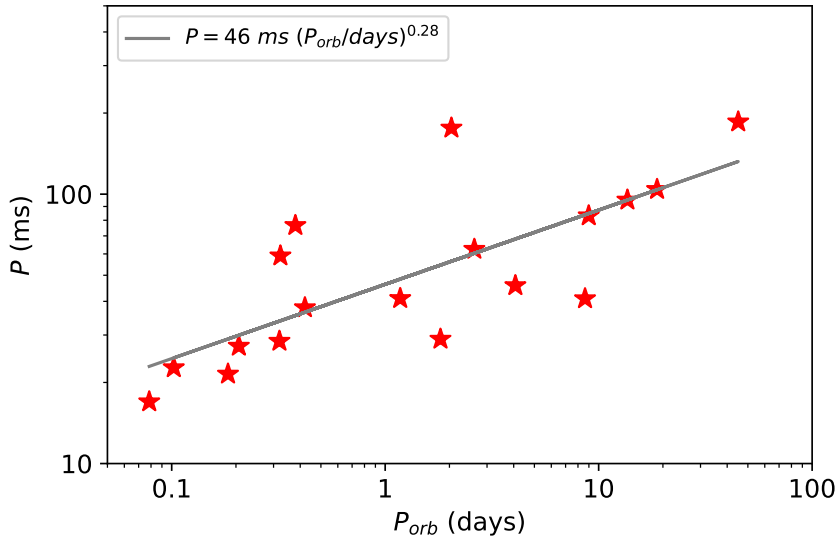

Figure 4.4: Spin period vs. orbital period of all first-born NSs. Observational data are plotted with red stars and a linear fit is given by the grey line, revealing a positive correlation between these quantities, as theoretically expected.

After the birth of a DNS binary, and depending on orbital separation and eccentricity, the system continues evolving while both stars spiral-in due to gravitational radiation reaction. For the closest systems, both components will merge within the Hubble time. Consequently, configurations of Galactic DNSs currently observed does not necessarily reflect their birth conditions, which is difficult to determine because of aspects such as the CE evolution and the imparted kicks. Following the same reasoning, their configurations will also change at the time they merge.

Secular orbital evolution of these systems are described under a quadrupole formalism of GR (Peters, 1964). To the lowest-order, it can be calculated from changes in the elements

of the relative orbit of two point masses resulting from GW damping, where the rates of change are:

$$\left\langle \frac{da}{dt} \right\rangle = -\frac{64}{5} \frac{G^3 M_{tot}^2 \, \mu}{c^5 a^3 (1-e^2)^{7/2}} \left(1 + \frac{73}{24} e^2 + \frac{37}{96} e^4\right), \tag{4.2}$$

$$\left\langle \frac{de}{dt} \right\rangle = -\frac{304}{15} \frac{G^3 M_{tot}^2 \, \mu \, e}{c^5 a^4 (1-e^2)^{5/2}} \left(1 + \frac{121}{304} e^2\right), \tag{4.3}$$

where μ is the reduced mass, M_{tot} the binary total mass and a the orbital separation. From the above equations it is possible to derive an expression for the merger time (τ_{GW}) as a function of the initial values:

$$\tau_{GW}(a_0, e_0) = \frac{12}{19} \frac{C_0^4}{\beta} \int_0^{e_0} \frac{e^{29/19} \left(1 + \frac{121}{304} e^2\right)^{1181/2299}}{(1-e^2)^{3/2}} de, \tag{4.4}$$

with constants given by:

$$C_0 = \frac{a_0 (1 - e_0^2)}{e_0^{12/19}} \left(1 + \frac{121}{304} e_0^2\right)^{-870/2299},$$

and

$$\beta = \frac{64 G^3}{5 c^5} M_{tot}^2 \mu.$$

Furthermore, since their birth, NSs are also believed to spin-down due to plasma currents in the magnetosphere and pulsar winds, usually described under the magnetic dipole model. In this sense, detections of spin of merging DNSs allows to shed light on the magnetic evolution of NSs. The spin evolution can be found from the deceleration equation for the spin angular frequency:

$$\dot{\Omega} = -K \Omega^n, \tag{4.5}$$

where $n = 3$ is the *braking index* for a dipole model, and K is the torque parameter with a numerical approximation of (Spitkovsky, 2006):

$$K = \frac{B^2 \, R^6}{c^3 I} (1 + \sin^2 \alpha), \tag{4.6}$$

where B is the surface magnetic field, R is the NS radius, I is the moment of inertia and α is the misalignment angle between the spin axis and the magnetic dipole moment. Here we followed the work from (Zhu et al., 2018), fixing the value $\alpha = 30^o$ and assuming a fiducial EoS AP4 (Lattimer and Prakash, 2001). The moment of inertia can be adjusted from a sample of analytical solutions of field equations to (Lattimer and Schutz, 2005):

$$I \simeq 0.237 M R^2 \left[1 + 4.2 \left(\frac{M}{M_\odot}\right) \left(\frac{km}{R}\right) + 90 \left(\frac{M}{M_\odot}\right)^4 \left(\frac{km}{R}\right)^4\right]. \tag{4.7}$$

From the mass-radius relation of AP4 EoS, and considering the mass range of recycled pulsars, we found $R = 11.5\ km$ to be a good approximation. By integrating Eq. 4.5, the spin period of a pulsar at merger time is found ($\Omega = 2\pi/P$):

$$P_{GW} = P_0 \left[1 + 2\frac{\dot{P}_0}{P_0}\tau_{GW}\right]^{1/2} . \tag{4.8}$$

This quantity will be important to calculate the *effective spin parameter* to be discussed in Sec. 4.5.2. The generic expression of Eq. 4.8 at any time t can provide a maximum age for the pulsar, at the point where $P = 0$ ms.

4.4 Supernova explosion and kick velocity distributions

Despite of rapidly spinning, NSs are also recognized as fast-moving objects. The first measurements of magnitude and direction of proper motions revealed that pulsars have average velocities at least an order of magnitude higher than their progenitor stars, which are generally of a few tens of km s^{-1}, and are moving outwards the galactic plane (Lyne et al., 1982). Nowadays, it is known that pulsar proper motion ranges between a few to 1500 km s^{-1}, and understand the origin of such spread and high velocities is of key importance to understand their properties and formation mechanisms (Coleman and Burrows, 2022). The disruption of binary progenitors is not sufficient to explain the high observed velocities of some isolated pulsars, making it necessary to investigate for an additional mechanism that speed them up.

The great effort in the development of supercomputing power has made possible to perform 2D and 3D numerical simulations of stellar core collapse and explosion with increasingly details, allowing to probe that asymmetries in mass-ejection caused by hidrodynamic instabilities are capable of transferring momentum to NSs compatible with the observed velocities of isolated pulsars (Janka, 2017), imparting a kick on the newborn NS. As stated in Coleman and Burrows (2022) there are currently 5 theoretical categories for modelling the kicks, roughly associated with the explosion asymmetries. One of the pioneers models invokes an off-centre spinning magnetic dipole and asymmetrical radiation of the nascent relativistic radio pulsar wind, but seems to be no longer supported (Harrison and Tademaru, 1975). Models relying in neutrino radiation on the context of rapid rotation are simplistic, but predict a natural spin-kick correlation (Spruit and Phinney, 1998). Models

on asymmetrical late-time fallback are shown feasible and produces a spin-kick alignment, but such phenomenon may be rare or occur only for a small subset of progenitors (Janka et al., 2022). Models relying on asymmetrical supernova matter ejecta and associated proto-NS recoil are widely employed (Nakamura et al., 2019), and contrasts with the models where kicks arise only from neutrino emission dipole asymmetries (Nagakura et al., 2019). Finally, there are models that consider both asymmetrical neutrino radiation and matter ejection (Burrows et al., 2020).

While the isolated pulsars can show velocities of thousands of kilometers in some cases, with an average in $\sim 400 - 500$ km s^{-1}, evidences points that pulsars in GCs and in DNSs should have received significantly lower kicks. Globular clusters possess scape velocities around 50 km s^{-1}, and consequently no NS would be expected to remain bound to it if imparted kicks were higher. In DNS binaries, the probability to keep the system bound decreases with increasing kick velocities, but it is also true that it depends on the orbital separation before the second SN. Tauris et al. (2017) found that the probability of the system survive to the second SN remains within 50% for large kicks up to 400 km s^{-1}, if the pre-SN system has an orbital period of $0.1 - 1$ days. Furthermore, the magnitude of imparted kick is expected to be proportional to the explosion energy and amount of ejected matter, although to calculate it accurately it is necessary to calculate stellar density structures at the end of Case BB RLO.

Janka (2017) used what is called the *gravitational tug-boat* mechanism to summarize the understanding of NS kicks, deriving a proportionality between the kick velocity ω, the energy of the explosion E_{exp} and a momentum-asymmetry parameter α_{ej} such as the larger the asymmetry, larger the kick. While for the CCSN of a heavy Fe core $E_{exp} \sim 3 \times 10^{50} - 2.5 \times 10^{51}$ erg, and α_{ej} can be as high as 0.33, in ultra-stripped supernovae these quantities are shown to be significantly lower, $E_{exp} \sim 10^{50}$ and $\alpha_{ej} < 0.03$. Additionally, small misalignment angles are also an evidence of small kicks since they are a result of geodetic precession, caused by spin-spin and spin-orbit couplings after the pulsar has its spin tilt respect to the orbital angular momentum vector, with large kicks expected to result in large misalignment's.

Ultra-stripped SNe responsible to form DNSs can come in two flavors, the electron-capture supernova (ECSN) from the collapse of an ONeMg core (Nomoto, 1987), and the Fe core-collapse supernova (Fe CCSN) of light cores. In the first case, the kick is expected

to be smaller than in the second, since the explosion energy is significantly smaller and the involved timescales where it takes place are not long enough to produce strong anisotropies. Notwithstanding, ECSNe are unlike to occur in close binary systems, because the mass window for producing them is restricted to a width of $\sim 0.2\ M_{\odot}$ (Tauris et al., 2015).

Despite of all these hints supporting lower kicks, most recent results shows that even relatively high kicks, of a few hundreds of km s^{-1}, can happen in DNS systems, exposing a possible bimodality as we will show latter.

4.4.1 Systemic velocities

The sudden mass loss in a SN explosion causes the system to receive a recoil velocity relative to the centre-of-mass rest frame of the pre-SN system. In case of an asymmetric explosion, the kick velocity will be added, and considering momentum conservation the systemic velocity after the second SN can be written as (Tauris and Bailes, 1996):

$$v_{sys} = \sqrt{(\Delta p_x)^2 + (\Delta p_y)^2 + (\Delta p_z)^2}/(M_{NS,1} + M_{NS,2}), \tag{4.9}$$

where the change in momentum is given by:

$$\begin{aligned}
\Delta p_x &= M_{NS,2}\omega\cos\theta - \Delta M_{ejec} M_{NS,1}\sqrt{G/(Ma_i)},\\
\Delta p_y &= M_{NS,2}\omega\sin\theta\cos\phi,\\
\Delta p_z &= M_{NS,2}\omega\sin\theta\sin\phi,
\end{aligned}$$

where ΔM_{ejec} is the amount of ejected matter, θ is the kick angle between the kick velocity vector and the pre-SN orbital velocity vector of the exploding star, ϕ is projection of the kick velocity onto a plane perpendicular to the pre-SN velocity vector of the exploding star, a_i is the initial orbital separation and ω is the kick velocity magnitude.

For DNS systems, however, it is not possible to measure the radial velocity component, whereas the transverse component can be estimated by combining the pulsar proper motion with its distance measure. To try reconstruct the kick probability a DNS system receives after the second SN, it is necessary to simulate the systemic velocities, and is only possible when measurements of proper motion are available, which is not always the case. This calculations are still ongoing and will be published in Rocha *et al.* in preparation, but so far they have confirmed high velocities for a few systems.

4.4.2 Relativistic spin precession

General relativity predicts that in pulsar binary systems the spin axis precesses around the rotation axis due to a gravitational spin-orbit coupling, in cases where it is misaligned with the orbital angular momentum vector. The inclination of the pulsed radiation respect to our line-of-sight changes and, as a consequence, the observed pulse profile also changes. This feature can be identified from observation of radiation properties if the system is tight enough. The angular rate of precession is (Bailes, 1988):

$$\Omega_{geod} = \left(\frac{2\pi}{P_b}\right)^{5/3} T_{\odot}^{2/3} m_c \frac{4m_p + 3m_c}{2(m_p + m_c)^{4/3}} \frac{1}{1 - e^2}. \tag{4.10}$$

Due to this effect, for example, the Hulse-Taylor pulsar (PSR B1913+16), will probably move out of our line-of-sight around the year 2025.

Depending on its magnitude, the kicks imparted on newly-born NSs can tilt the orbit, changing the orientation of the pulsar spin vector respect to the total angular momentum vector. The misalignment angle between these two vector is then given by (Kramer, 1998):

$$\delta = tan^{-1}\left(\frac{\omega \sin\theta \sin\phi}{\sqrt{(v_{rel} + \omega\cos\theta)^2 + (\omega \sin\theta \cos\phi)^2}}\right). \tag{4.11}$$

During the recycling process the accretion torque is believed to align the spin axis of the first-born NS with the orbital angular momentum vector. Based on this assumption, it is possible to use the observed misalignment angle to constraint kick properties of the second SN.

4.4.3 Second-born NS masses and kick magnitudes

When we observe the kick velocity magnitude as a function of the second-born NS mass, a positive correlation seems to be present (see Figure 4.5 extracted from Tauris et al., 2017). This relation seems completely plausible when considering the arguments that the explosion energy and the asymmetry of the explosion ejecta are systematically smaller for explosions of lighter cores, leading to small NS masses. The results shows that, although most ultra-stripped SNe are expected to generate small kicks, larger NS kicks can also happen for more ordinary iron cores. A larger sample of systems with measured proper motion is necessary to confirm the apparent correlation.

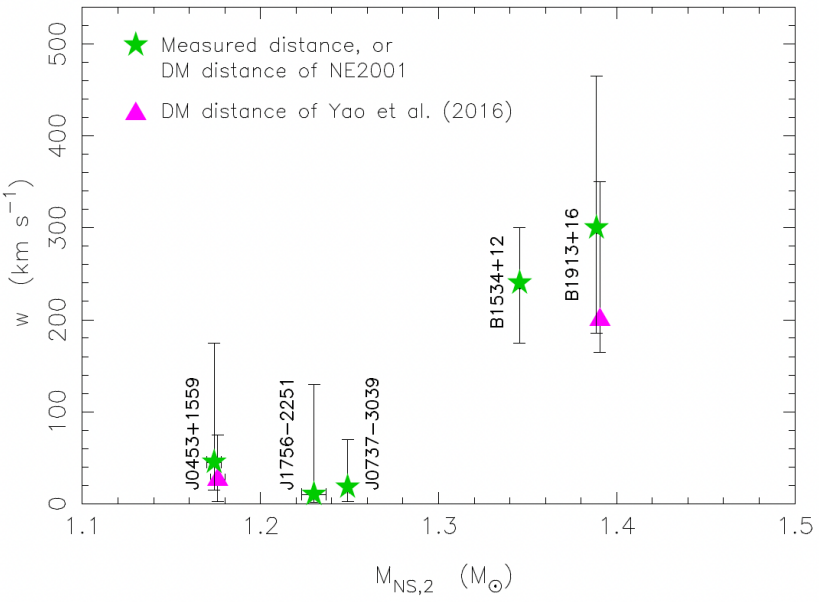

Figure 4.5: Kick velocity as a function of second-born NS mass. For each DNS two distance models were applied. This Figure was extracted from Tauris et al., 2017.

4.4.4 Second-born NS masses and eccentricities

A possible correlation for second-born NS masses and eccentricities emerges from the hypothesis of ($M_{NS,2}$, ω) correlation, since systems that experience larger kicks are more likely to obtain larger eccentricities. The assumption that kicks are isotropically distributed (have no preferred orientation), however, results in a large spread in post-SN eccentricities and can mask such correlation. As seen in Fig 4.6, an average trend still persists on the ($M_{NS,2}$, e)-plane despite of the spread effect.

We have employed both KS and AD hypothesis tests to check whether the group of companion NSs in systems with eccentricity lower than 0.4 (and lower kicks) are drawn from the same distribution of the systems with eccentricities > 0.4, and the resulting p-value is of 5×10^{-4} for the KS test and 2×10^{-5} for the AD test. This result can provide evidences for different supernova mechanisms behind their formation, although further studies are still necessary to investigate if they arise from different ultra-stripped SN flavors, or from an ultra-stripped Fe CCSN group *vs.* a "normal" Fe CCSN. Furthermore, the sample is still very limited and is also possible that as the sample grows, we observe a larger spread through the plane, weakening the correlation.

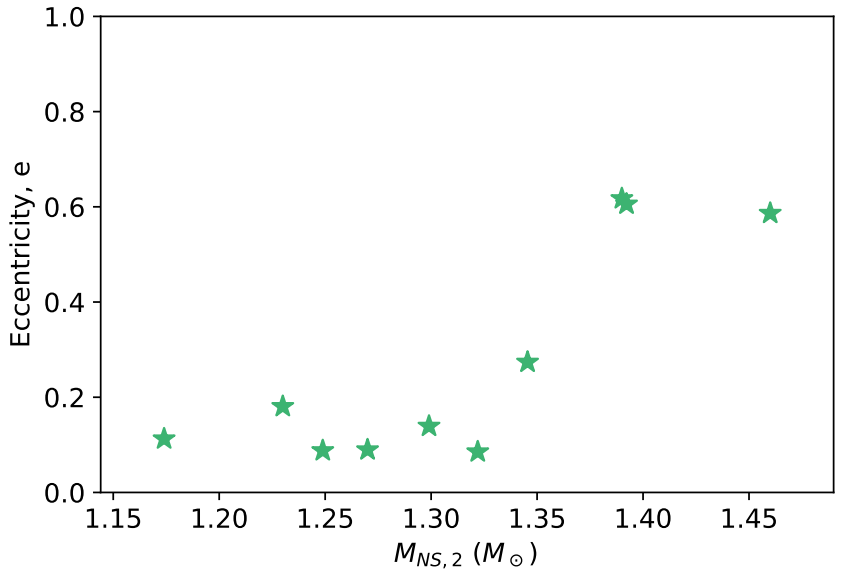

Figure 4.6: Eccentricity as a function of second-born NS mass. An apparent average trend is seen, but is also possible that a large scattering emerges in this diagram as more DNS sources are added, an effect of the isotropic orientation of kick directions.

4.5 Gravitational waves

Gravitational wave (GW) emissions are ripples in the spacetime manifold caused by the movement of massive objects, and were predicted by Einstein's theory of General Relativity (GR). The most intense sources of GW emissions are the merger of compact objects like neutron stars and black holes, releasing a great amount of energy. These components lose energy while orbiting each other, and as a consequence they spiral-in reducing the orbital period further and further. The discovery of PSR B1913+16 (Hulse and Taylor, 1975) provided the first evidence for the existence of this effect, by the observation of orbital decay during time, through the timing of the P_b parameter (Taylor and Weisberg, 1982). This discovery triggered a great interest in the scientific community and placed DNSs as the main target for groundbased interferometric detectors.

Since the produced signals are very weak, detection of GW emissions was a challenging task for decades. The Laser Interferometer Gravitational-Wave Observatory (LIGO) was founded in 1992 by Kip Thorne and Ronald Drever from Caltech and Rainer Weiss from the MIT (Abbott et al., 2009). LIGO consists of two identical interferometers separeted by 3002 kilometers, located in fairly isolated areas of Washington (LIGO Hanford) and Lousiana (LIGO Livingston). The reason behind this large distance is found in their sensitivities. Since these instruments are very sensitive, they can detect the tiniest vibrations on Earth,

from sources that are nearby until those which are thousands of kilometers away, and this can mask the GW signal in each detector. Locating the interferometers far away, it is possible to distinguish between GW signal and local noise. The original instrument was operational from 2002 to 2010 but no detection was made at that time. During these years the team made huge progress in detector engineering and both interferometers were redesigned from 2010 to 2014.

LIGO's interferometers are, in a sense, similiar to Michelson interferometers, invented in the 1880's and used to (un)probe the existence of ether through detection of interference patterns, with an ideal configuration to precisely measure phase changes of a wave traveling along two perpendicular arms with an "L-shape". The GW's cause the manifold to stretch in one direction and compress in a perpendicular direction, and is the reason why the layout shown in Figure 4.7 is choosen. In summary, a powerful laser beam is equally splitted and directed towards both arms, bouncing off mirrors at the end of each arm. An additional mirror is placed in each arm, near the beam splitter and 4 km away from the end mirror, to create a *Fabry Perot cavity*. This causes the laser to bounce between the two mirrors about 300 times before being recombined. When gravitational waves pass through, an interference pattern is observed when the beams are recombined. The recombined laser beams are directed towards photodetectors that measure this interference pattern created by the superposition of the two beams. By analyzing the interference it is possible to determine the characteristics of the gravitational waves and gain insights into the astrophysical events that produced them.

The Virgo interferometer with a 3 km arms, built outside of Pisa, joined the observations of LIGO in 2017 after a period improving its sensitivity (Accadia et al., 2012). Its operation, combined with both Hanford and Livingston detectors is crucial to localize the sources of GW signals because they are determined from the time delay between different observatories. More recently, the KAGRA observatory also started operating. It is constructed in Japan, inside the Kamioka mine where is also located the neutrino detector Super Kamiokande (Akutsu et al., 2018). The underground location and use of cryogenic systems took the detector to another level, minimizing seismic and molecular vibrations that can mask the GW signal.

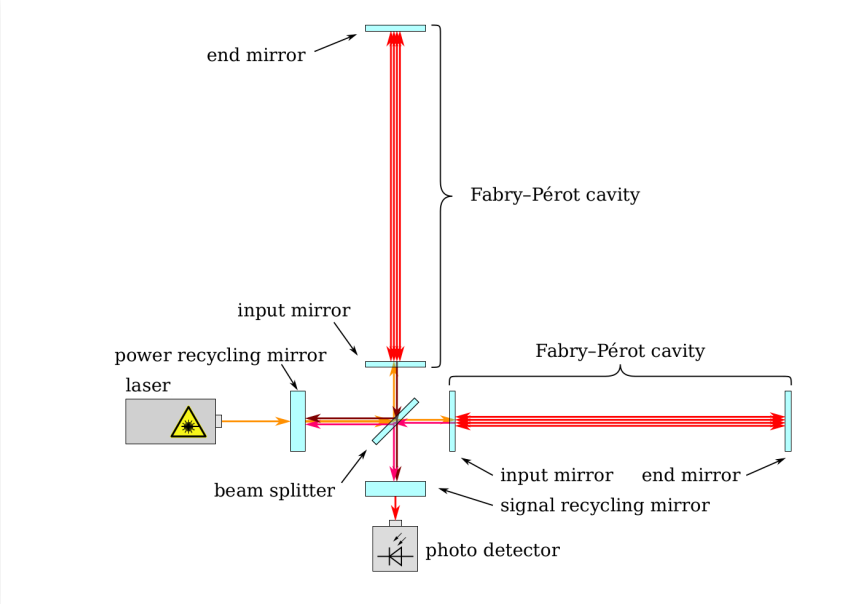

Figure 4.7: Simplified schematic of LIGO detectors. The laser beam is splitted and directed towards each arm, where the beam enters in a Fabry-Pérot cavity and is bounced between the mirrors about 300 times before being recombined. Extracted from Wikipedia in Aphril 2023.

4.5.1 Chirp mass

Parameters that influences the evolution of waveform phase can be precisely constrained given the large number of cycles in the observable waveform (Cutler and Flanagan, 1994). The same does not hold for parameters which affects only wave polarization or amplitude. The best constrained quantity from a GW signal is the called *chirp mass* ($\mathcal{M}$).

To lowest order, it is possible to describe the gravitational radiation from the quadrupole Newtonian formalism of two dimensionless particles in an almost circular orbit (assuming that gravitational damping circularizes the orbit). The angular orbital frequency is then given by:

$$\Omega_b^2 = \frac{GM_{tot}}{a^3}. \tag{4.12}$$

The loss of energy leads to a decrease in a and, consequently, a decrease in the orbital period since $P_b \equiv 2\pi/\Omega_b$. Combining the inspiral rate of the system and Eq. 4.12, the signal frequency ($\nu = 1/P$) is then obtained:

$$\nu^{-11/3}\frac{d\nu}{dt} = \frac{96}{5}\pi^{8/3}\mathcal{M}^{5/3}. \tag{4.13}$$

Therefore, from the observed signal frequency and its derivative is possible to accurately measure the chirp mass, which is a combination of total and reduced (μ) masses of the system, $\mathcal{M} = \mu^{3/5}M_{tot}^{2/5}$, and to determine the rate at which the frequency of the GW

changes over time. These calculations are valid for the source-frame. When detected on Earth, the signal is Doppler shifted due to relative motion, and the detected value will be $\mathcal{M}_{det} = (1+z)\mathcal{M}$, where z is the redshift of the source.

All binaries with the same $\mathcal{M}$ will have the same chirping sweep. Still, post-newtonian corrections to Eq. 4.13 do introduce a dependence on the indivual masses of the system. This quantity is inferred by a matched filtering technique, where the wave's phase evolution is matched with model templates predicted under GR.

4.5.2 Effective spin parameter

Spinning of coalescing compact objects has effects in both phase and amplitude of GW's. From one side, it can increase or decrease the inspiral rate, and from the other, it can lead to orbital precession due to spin-orbit and spin-spin interactions (Kidder et al., 1993). To the leading order, gravitational waveform depends on the spin through the *effective spin parameter* χ_{eff}:

$$\chi_{eff} = \frac{m_1\ \chi_1\ cos(\delta_1) + m_2\ \chi_2\ cos(\delta_2)}{m_1 + m_2}, \tag{4.14}$$

where δ_j are the misalignment angles between the spin vectors and orbital angular momentum vector, and $\chi_j = cI_j\omega_j/Gm_j^2$ are the dimensionless spin magnitudes of the merging objects, $j = [1, 2]$. For simplicity, the spin magnitude of young NSs can assumed to be null since they are much slower than the recycled component. Thus, the only contribution to the effective spin in DNS mergers comes from the final dimensionless spin parameter of the first-born NS computed at the time of merger (χ_f).

While previously thought that the spin axis of recycled NSs where aligned with the orbital angular momentum before the merger, based on the measurement found for the double pulsar PSR J0737-3039A ($\delta < 3.2°$) (Zhu et al., 2018), measurements found for the systems PSR B1534+12 (Fonseca et al., 2014), PSR J1756-2251 (Ferdman et al., 2014) and PSR B1913+16 (Kramer, 1998) revealed the presence of a non-null misalignment angle and ruled out the hypothesis of $\delta_1 = 0°$ for all systems. As we mentioned in Sec. 4.4, these misalignment angles are related with kick magnitudes imparted in the second-born NS responsible for changing the orbital orientation, and which can be significantly high in some systems.

In Table D we included χ_{eff} values for systems where a misalignment angle was found.

The values reported for GW170817 and GW190425 are subject to low-spin priors (constraints the spin to $\chi \leq 0.05$, with uniform distribution)[4], since this range is likely compatible with dimensionless spins of galactic DNSs. Furthermore, χ_{eff} shows a degeneracy with $\mathcal{M}$ and specially with q, being strongly dependent on prior choices. Mass-ratio constraints placed on progenitor systems of GW signals by the low-spin prior are also shown to be in agreement with galactic observations, including even the most asymmetric systems (Abbott et al., 2019, 2020).

4.5.3 First detections of DNS mergers

The first detection of a gravitational wave was made in 2015 by LIGO detectors, from a binary black hole merger named GW150914 (Abbott et al., 2016). However, the most exciting detection came two years latter with the first detection of a compact binary merger, GW170817 (Abbott et al., 2017b), quickly associated with a short GRB emitted from the same sky location 1.7 s after the merger (Goldstein et al., 2017). This started the true era of multimessenger and multiwavelength astronomy. The precise location of the event allowed a follow-up leading to detections in X-ray, ultraviolet, optical, infrared and radio bands. The optical counterpart, AT2017gfo (Coulter et al., 2017), placed NGC 4993 as the host galaxy with a Tully-Fisher distance of ~ 40 Mpc (Freedman et al., 2001), consistent with the inferred GW luminosity distance. The association of the gravitational wave with the sGRB, as well as the observations across the electromagnetic spectrum (Deller et al., 2017; Corsi et al., 2017; Deller et al., 2017), the total and component masses of the system and the offset related to the galaxy center provided strong evidences for the DNS nature of GW170817.

On April 2019, the second gravitational wave signal consistent with the coalescence of a DNS was detected, GW190425 (Abbott et al., 2020). This event is identified as a single-detector since at the time it was detected the LIGO-LHO was offline and the signal-to-noise ratio of Virgo was 2.5, below the threshold of 4.0 for significance estimation. The localization of a GW signal relies on measuring the time delay between observatories, but since GW190425 is a single-detector event was not possible to set straight constraints on the sky map region. As a consequence, a follow-up became challenging and until now there is now firm detection of an electromagnetic counterpart. Nonetheless, it is important to

[4] The high-spin prior assumes uniform distribution for $\chi \leq 0.89$.

note that the event itself is highly significant. While it is not possible to rule out the possibility of one or both components being BH's, due to the absence of sensitivity to probe matter effects, this hypothesis is unlikely. However, the total and chirp masses of this particular system differs significantly from the known Galactic DNS systems as we show in Figure 4.8. This fact may indeed signal the existence of a different formation mechanism for GW190425-like binaries.

To quantitatively compare the GW events with the Galactic distribution, we reproduced the analysis made by LIGO Collaboration (Abbott et al., 2020). In left panel of Fig. 4.8 we have plotted a histogram for the total mass of 10 Galactic systems which are expected to merge within a Hubble time (since these are the potential GW sources), as well as a normal distribution fit for Galactic sources, with a resulting mean at 2.69 $M_\odot$ and a standard deviation of 0.12 $M_\odot$. The total mass of GW170817 falls completely within the Galactic range, while the GW190425 is five standard deviations away from the mean. Finally, in the right panel we show the chirp mass distribution for 9 Galactic systems that will merge within Hubble time and the corresponding fit, with a mean at 1.17 $M_\odot$ and standard deviation of 0.05 $M_\odot$. Here the GW170817 falls again within the Galactic population range, while the GW190425 lies $\gtrsim 5\sigma$ apart of the mean value. If confirmed to be emitted from the merger of two NSs, this behaviour of GW190425 might reveal a population with different characteristics of the GW170817-like ones. Efforts in both galactic DNS and GW searches are of fundamental importance to probe such differences.

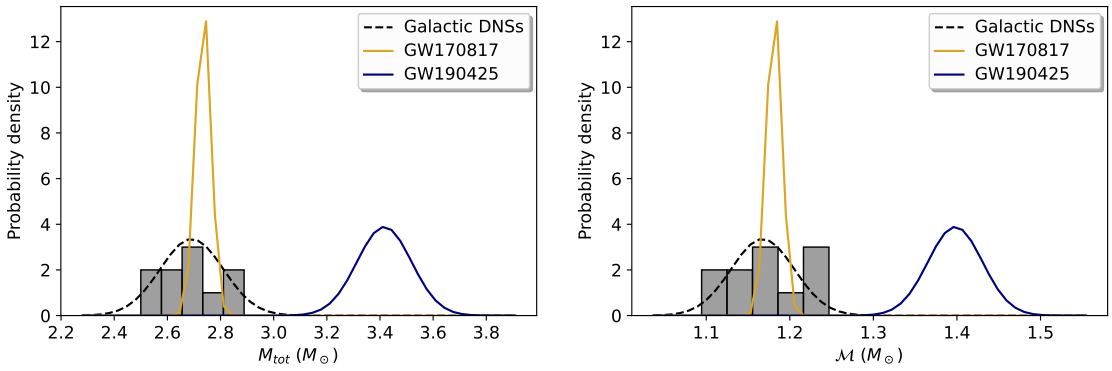

Figure 4.8: Total (left) and chirp (right) mass histograms for all systems that will merge within a Hubble time is shown in grey. The black dashed curve is a normal distribution fit. In both cases is possible the see that GW170817 is consistent with the galactic DNSs, while GW190425 fall 5σ appart from total and chirp masses of galactic systems.

4.6 Conclusions

Gravitational wave observations from the merger of compact objects opened up a new window to explore the physics of neutron stars. However, contrary to expectations, until now only one system is undoubtedly the result of a NS-NS merger, GW170817, while a second event is very likely from a NS-NS merger as well, GW190425, even with the absence of electromagnetic counterpart detected. This scenario completely rule out the merger rate, $\mathcal{R}_{NS-NS}$, initially computed for this sources of GW's. Furthermore, as we shown in Section 2.3.3, the metallicity influences the range of mass for progenitor stars giving origin to NS's. Consequently, it is not known exactly if the same distribution of masses we observe in the local sample will be consistent with the mass distribution of merging NS's. Beyound that, we showed in Figure 4.8 that the event GW190425 has properties quite different from the GW170817, and is not consistent with the total and chirp masses of galactic DNS's. Again, an enlarged sample is of fundamental importance to understand if these GW detections are essentialy different and belongs to distinct populations, or if GW190425 is an outlier and represents an isolated case.

To understand GW detections, set reliable constraints in observables and even improve detector's sensitivity to search for GW events from the merger of DNSs, it is necessary to understand how these systems are initially formed, their properties at birth, how the spiral-in phase occurs and which properties can be detected at merger and even how systems merging within the Hubble time differs from those that will not. Extensive work has and continues being made both theoretically and computationally to simulate the evolution of DNS systems.

The objective of this Chapter is to reunite all available information from galactic DNS's systems, check for patterns previously and extensively discussed in Tauris et al. (2017) and create a catalogue that will be constantly updated with new discoveries. We hope the scientific community can benefit from this initiative, and it helps to construct an trustworthy scenario for formation and evolution of DNS's as well as strengthen GW detections.

Chapter 5

Strange Stars under a *color-flavor-locked* model

Compact stars are described under the theory of GR. As we already mentioned, Karl Schwarzschild was the first to obtain an exact solution for the EFE. Since then, the number of proposed solutions with the most varied applications has been growing. However, the majority of proposed solutions are *toy models* and do not describe real objects since they do not satisfy all conditions for physical acceptability as those described in Sec. 2.4.1

Delgaty and Lake (1998) reviewed the problem and studied exact solutions under the criteria to describe real compact objects. They constructed a catalog with all analytic solutions describing an isolated, static and spherically symmetric perfect fluid. From an initial set of 127 exact solutions, only 16 of them were shown to satisfy the conditions to be considered physically interesting, and out of these, only 9 presented a monotonic decrease of sound speed, a highly desirable - if not mandatory - condition.

Despite of the small number of solutions useful to describe NSs, they provide none information about inner composition of these stars, which is only achieved by modelling the EoSs. To explore the behaviour of matter at supranuclear densities is one of the most complex and challenging problems in modern physics. It requires an interdisciplinary effort between nuclear physics, particle physics and relativistic astrophysics, with a fundamental support from experiments and observations to validate models.

The extreme conditions under which NS are found, with densities several times above the nuclear saturation density ($n = 0.16\ fm^{-3}$), are described under the theory of *Quantum Chromodynamics* (QCD), whose phase diagram is shown in Fig. 5.1. Regions of low densities and high temperatures are accessible through modern experiments like the Large Hadron Collider (LHC) and Relativistic Heavy Ion Collider (RHIC). On the other side, regions with very high densities and high temperatures are described from first-principle

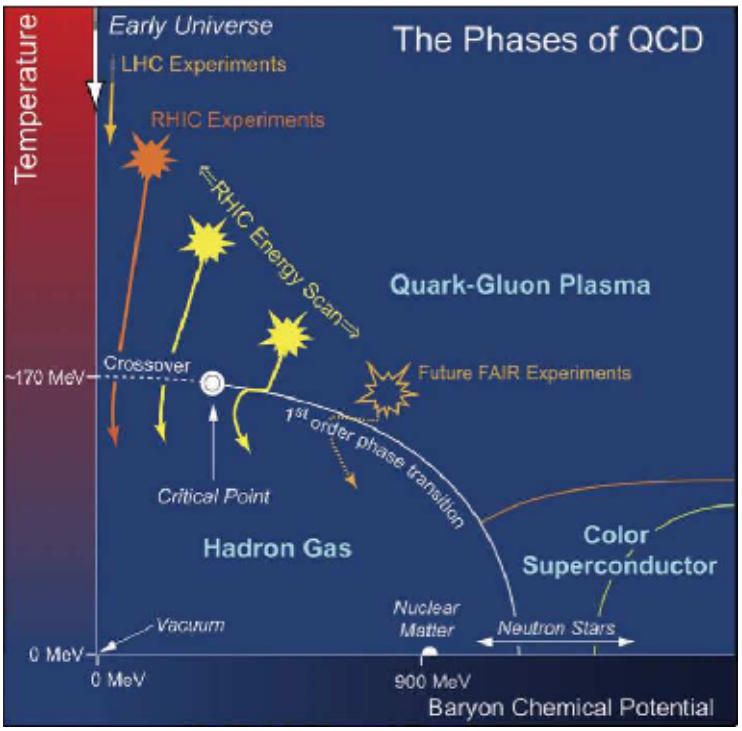

Figure 5.1: Phase diagram of QCD. Neutron Stars are found in a region difficult to access both from experiments and first-principle calculations.

calculations on perturbative QCD. Contra-intuitively, the intermediate region where NS's are located is the most difficult to access both from experiments and first-principle calculations, and this is the reason why a large number of EoSs are proposed in an attempt to describe such objects, and why they have to be submitted to observational constraints to check for consistency.

We present in this Chapter a new class of exact solutions connected with microphysics, providing an EoS which describes the internal structure of a compact star made of strange matter in the *color-flavor-locked* (CFL) phase, a color superconductivity phase arising when Cooper pairing breaks the color gauge symmetry, which we will describe later. The mass-radius relation (an important feature of stellar sequences) for the given equation is analytically constructed, determining a maximum mass.

5.1 Strange matter hypothesis

Gell-Mann (1964) and Zweig (1964) independently suggested that strong interaction could be explained by assuming that hadrons (baryons and mesons) are composed of three fundamental particles, which where named as *quarks*. Despite of challenging the

fundamental nature of hadrons, the existence of quarks raised up the unimaginable idea of fractional charges. One of the quarks should have 2/3 of electrical charge, and the remaining two -1/3.

The evidence for the existence of these constituents came from a series of deep inelastic scattering where the phenomenon of *scaling* was observed. Scaling meant that the scattering cross section (a measure of the probability of a scattering event) did not depend on the energy of the scattering particles, but only on the momentum transfer. This was difficult to explain if protons and neutrons were viewed as indivisible particles, but could be explained if they were actually composed of smaller constituents, such as quarks. Nowadays, the existence of six types of quarks, called *flavors*, are well known: *up* (u), *down* (d), *strange* (s), *charm* (c), *top* (t) and *bottom* (b). Interactions between these quarks are given through the exchange of *gluons* and are described under the theory of QCD.

The MIT bag model, proposed by Chodos et al. (1974), played an important role in the development of the physics of hadrons and of interactions of nucleons. According to it, quarks are confined into a region of space called *bag*, immersed on vacuum which exerts a pressure on the bag ($P_{vac} = -B$), as shown in Figure 5.2. Inside this region the quarks are assumed to be free.

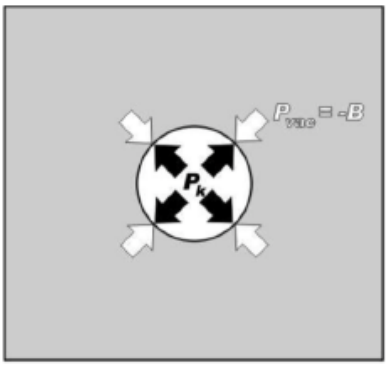

Figure 5.2: MIT bag model. Inside the bag quarks are free, but the bag itself is confined and immersed on a vaccum which exerts a pressure on it.

Witten (1984), was one of the first, following the work of Bodmer (1971) and Terazawa et al. (1978), to boost the proposal that strange quark matter (SQM) could be the true ground state of dense matter, instead of ^{56}Fe nuclei, having a lower energy per baryon than ordinary nuclei. This matter is assumed to be composed of roughly equal numbers of *up*, *down* and *strange* quarks and a small number off electrons to attain charge neutrality. If this hypothesis is proven to be true, NS would actually be *Strange Stars* (SS), possibly

enveloped in thin nuclear crusts.

The emergence of s quarks due to semileptonic decay reduces the Fermi energy of the system and, as a consequence, strange matter is more stable than a matter made of only u and d quarks. The energy per nucleon should obey the relation:

$$\frac{E}{A}|_{u,d,s} < \frac{E}{A}|_{^{56}Fe} < \frac{E}{A}|_{n} < \frac{E}{A}|_{u,d}, \tag{5.1}$$

where n stands for nuclear matter. As a conclusion, the atomic nucleis should be only metastable states.

5.2 Non-interacting quark matter

A thermodynamical potential in the grand canonical ensemble is given by:

$$\Omega = E - \mu N - TS, \tag{5.2}$$

where E is the energy, μ the chemical potential, N the number of particles, T the temperature and S the entropy. The system pressure is $P = -\Omega/V$.

The chemical potential of c, b and t quarks are greater than the chemical potential inside the stars ($\sim 300 - 600$ MeV) and for this reason they are not considered in the discussion. Furthermore, u and d quarks possesses low masses that can be neglected, so the only remaining contribution comes from strange quark mass (m_s). Assuming a degenerate gas of free quarks, the energy density (ρ), numerical density (n_f) and pressure (P_f) of each flavor ($f = u, d, s$) are given by:

$$\begin{aligned} \rho_f &= \frac{3}{\pi^2}\int_0^{k_{F,f}} k^2\sqrt{k^2+m_f^2}\; dk\,, \\ n_f &= \frac{k_{F,f}^3}{\pi^2}\,, \\ P_f &= \frac{3}{\pi^2}\int_0^{k_{F,f}} k^2(\mu_f - \sqrt{k^2+m_f^2})dk. \end{aligned} \tag{5.3}$$

The most relevant processes occurring in the 3-flavor matter are the following:

$$d \to u + e + \bar{\nu}_e \quad and \quad s \to u + e + \bar{\nu}_e, \tag{5.4}$$

$$u + e \to d + \nu_e \quad and \quad u + e \to s + \nu_e, \tag{5.5}$$

and

$$s + u \leftrightarrow d + u. \tag{5.6}$$

Since neutrinos have null chemical potentials, the above process take us to the following conditions:

$$\mu_d = \mu_e + \mu_u, \quad and \quad \mu_s = \mu_e + \mu_u, \tag{5.7}$$

from which we conclude that $\mu_d = \mu_s$. Charge neutrality can be made explicit by:

$$\sum_{f=u,d,s} q_f n_f - n_e = 0, \tag{5.8}$$

where $q_u = \frac{2}{3}$ e $q_d = q_s = -\frac{1}{3}$.

The bag constant, B, is included to guarantee that the confined (hadronic) phase is preferable within a critical temperature, above which the deconfinement becomes energetically advantageous. In the context of compact objects we consider $T = 0$ and high chemical potentials. Pressure and free energy of quark matter are given by:

$$P + B = \sum_f P_f, \tag{5.9}$$

$$\rho = \sum_f \rho_f + B. \tag{5.10}$$

For simplicity, we initially consider $m_s = 0$, and ignore the presence of electrons. These conditions take us to the following solutions:

$$n_f = \frac{\mu_f^3}{\pi^2}, \quad \rho_f = \frac{3\mu_f^4}{4\pi^2} \quad and \quad P_f = \frac{\mu^4}{4\pi^2}, \tag{5.11}$$

and is easy to see that $P_f = \frac{\rho_c}{3}$.

By combining equations (5.9) and (5.10) we are conducted to the EoS of strange quark matter without interactions, also recognized as the MIT EoS:

$$P(\rho) = \frac{1}{3}(\rho - 4B). \tag{5.12}$$

This equation of state does not depend on the number of flavors, and is exact both for the strange quark matter ($m_s \to 0$) and the quark matter made of two flavors ($m_s \to \infty$).

From now on, we include the mass effects to the lowest orders[1]. It is convenient to introduce an average chemical potential $\mu = \frac{1}{3}(\mu_u + \mu_d + \mu_s)$, as well as the μ_e for the electron:

$$\begin{aligned} \mu_u &= \mu - \frac{2}{3}\mu_e, \\ \mu_d = \mu_s &= \mu + \frac{1}{3}\mu_e. \end{aligned} \tag{5.13}$$

[1] Higher order terms contributes minimally to the equation.

directly satisfying Eq. (5.7). The Fermi momentum of each quark assumes the value:

$$k_{F,u} = \mu_u, \quad k_{F,d} = \mu_d \quad and \quad k_{F,s} = \sqrt{\mu_s^2 - m_s^2}. \tag{5.14}$$

For the condition of charge neutrality, Eq. (5.8), we find a relation between the chemical potential of the electron and the mass of quark strange, $\mu_e \approx \frac{m_s^2}{4\mu}$. In this way, it is possible to express the Fermi momentum of each flavor as a function of μ and m_s only. We then arrive to the equations:

$$\sum_f \rho_f = \frac{3}{4\pi^2}(3\mu^4 - \mu^2 m_s^2), \tag{5.15}$$

$$\sum_f P_f = \frac{3}{4\pi^2}(\mu^4 - \mu^2 m_s^2). \tag{5.16}$$

The EoS including the mass of strange quark is now:

$$P = \frac{1}{3}(\rho - 4B) - \frac{\mu^2 m_s^2}{2\pi^2}. \tag{5.17}$$

A detailed approach for these calculations can be found in Schmitt (2010).

5.3 *Interacting quark matter*

There is a consensus nowadays that the *color-flavor-locked* (CFL) phase might be the fundamental state of matter, at least at asymptotic densities. A possible correction to the quark matter EoS is to consider pairing interactions. The binding energy can be included subtracting $3\Delta^2\mu^2/\pi^2$ from the thermodynamical potential. The exact nature of the interaction that generates the gap Δ is irrelevant.

Under the BCS theory, proposed by John Bardeen, Leon Cooper and John Schrieffer, for systems at low temperatures and subject to short-range attractive interaction, there will always be a pairing, taking the system to a low Fermi energy level, justifying the correction for the thermodynamical potential.

The equations for pressure and energy density assume the form:

$$P = \frac{3\mu^4}{4\pi^2} - \frac{3\mu^2 m_s^2}{4\pi^2} + \frac{3}{\pi^2}\Delta^2\mu^2 - B, \tag{5.18}$$

$$\rho = \frac{9\mu^4}{4\pi^2} - \frac{3\mu^2 m_s^2}{4\pi^2} + \frac{3}{\pi^2}\Delta^2\mu^2 + B. \tag{5.19}$$

Finally, the EoS for the strange quark matter at the CFL state results in:

$$P = \frac{\rho}{3} - \frac{4}{3}B + \left(\frac{2\Delta^2}{\pi^2} - \frac{m_s^2}{2\pi^2}\right)\mu^2, \tag{5.20}$$

with:

$$\mu^2 = -\eta + \left(\eta^2 + \frac{4}{9}\pi^2(\rho - B)\right)^{1/2}, \qquad \eta = -\frac{m_s^2}{6} + \frac{2\Delta^2}{3}. \tag{5.21}$$

The term proportional to Δ^2 turns the EoS *stiffer* if compared with the non-interacting case, so the pressure will be higher for a given value of central density. On the other hand, the term proportional to m_s^2 makes the EoS *softer*, but has a less significant contribution. As a consequence, a stiffer equation of state allows the matter to support a higher gravitational force, and consequently the maximum mass for this kind of matter can be higher than for nuclear matter.

5.4 Strange Stars in a CFL phase

Alcock et al. (1986; hereafter referred as AFO), employed the MIT bag model EoS to describe the properties of a SS assuming quarks to be asymptotically free, and neglecting the strange quark mass (m_s), given by Eq. (5.12). Results led to a maximum mass value around 2 $M_\odot$ (Figure 3 in Alcock et al., 1986), for $B = 57\ MeV\ fm^{-3}$, for a strange star in the MIT phase.

Rajagopal and Wilczek (2001) worked in a model of strange matter in the *color flavor locked* (CFL) phase, made of u, d and s quarks with no electrons. They argue that at sufficiently high densities a phase transition may occur between CFL and nuclear matter, so that SS might be composed of CFL matter. Lugones and Horvath (2002) worked on a CFL star model with pairing interactions, since they appears to be relevant for dense phases. The presence of pairing gaps actually *enhance* the possible stability of the quark matter phase (Lugones and Horvath, 2002, 2003).

We made a series expansion of Eq. (5.20) to derive a equation of state that depends only on the energy density ρ and the free parameters η and B, and conserved only up to the first order:

$$P(r) = \frac{1}{3}\rho + \frac{2\eta}{\pi}\rho^{1/2} - \left(\frac{3\eta^2}{\pi^2} + \frac{4B}{3}\right). \tag{5.22}$$

This expansion was made in order to simplify the system of equations, resulting in an easier way to treat them analytically, while remaining essentially identical to the *exact* one. AS

we can see from EQ. 5.21, if we assume $m_s \to 0$ and noninteracting quarks, the MIT bag model EoS is restored.

Following the same procedure as Tolman (1939) and many others in literature, we worked on the construction of exact solutions for the *Einstein Field Equations* (EFE) that describes a uncharged, static and spherically symmetric fluid with anisotropic pressure, i.e., an anisotropic energy-momentum tensor. The idea that the tangential component of pressure differs from the radial component inside compact stars was proposed by Ruderman (Kumar and Bharti, 2022). For fluids under high-density regimes many phenomena can happen leading to pressure anisotropy, as the presence of solid cores, pion-condensation, slow rotation, strong magnetic fields and etc. Even if the system is initially isotropic, processes such as dissipative fluxes will lead to anisotropies.

The set of equations describing the macrophysics of the compact object, yet with spherical symmetry, is now distinct from those given in Eq. (2.18), since the radial (P_r) and tangential (P_t) pressures are different:

$$\begin{aligned} \frac{8\pi G}{c^2}\rho &= \frac{2\lambda'}{r}e^{-2\lambda} + \frac{1-e^{-2\lambda}}{r^2}\,, \\ \frac{8\pi G}{c^4}P_r(r) &= \frac{2\nu'}{r}e^{-2\lambda} - \frac{1-e^{-2\lambda}}{r^2}\,, \\ \frac{8\pi G}{c^4}P_t(r) &= e^{-2\lambda}\left[\nu'' + \nu'^2 - \nu'\lambda' + \frac{\nu'-\lambda'}{r}\right]. \end{aligned} \tag{5.23}$$

In addition, the equation describing the hydrostatic equilibrium of the object is no longer given by the famous TOV, but instead by what is called the *generalized TOV*:

$$-\frac{dP_r}{dr} = \frac{G(\rho c^2 + P_r)(m(r)c^2 + 4\pi r^3 P_r)}{r^2(c^2 - 2Gm(r)/r} + \frac{2(P_r - P_t)}{r} \tag{5.24}$$

To fully resolve the system of EFE describing a SS we assumed: two different *ansatz* (later discussed) for the metric function, a radial pressure given by Eq. 5.22, and inital and boundary conditions to ensure physical acceptability, as described in Sec. 2.4.1.

5.4.1 Thirukkanesh-Ragel ansatz

Using the *ansatz* proposed by Thirukkanesh and Ragel (2012) as follows:

$$e^{-2\lambda} = Z(r) = \left(1 - aCr^2\right)^n, \tag{5.25}$$

where a and C are real constants and n an adjustable integer, we construct the first class of solutions for the system. Energy density profile, pressure profiles and mass-radius diagrams

were constructed for different combinations of free parameters and are shown in Figures (5.3) and (5.4). The product $aC(=\frac{\rho_c}{6})$ was determined in terms of the central density ρ_c, and we assumed $n = 2$.[2] The construction of solutions can be followed with more detail in our published work (Rocha et al., 2020a)

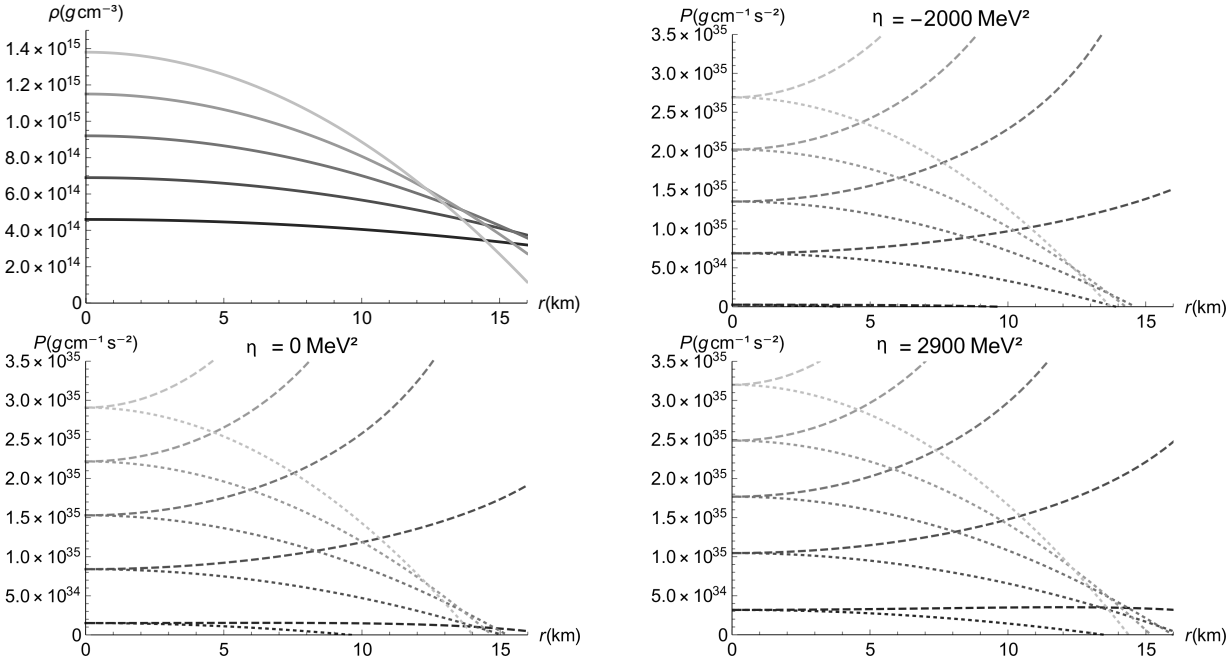

Figure 5.3: Thirukkanesh-Ragel ansatz. The first graph (top-left) is a construction of energy density profiles monotonically decreasing with r, in which low central densities (darkest curves) shows a lower decrease slope. The following three graphics represents pressure profiles, being P_r represented by dotted lines and P_t by dashed lines. For $\eta = -2000$ MeV^2 we set $m_s = 150$ MeV and $\Delta = 50$ MeV; for $\eta = 0$ MeV^2 we have $m_s = \Delta = 0$ MeV; and finally, for $\eta = 2900$ MeV^2 we fixed $m_s = 150$ MeV and $\Delta = 100$ MeV. The surface of a given star is reached when P_r vanish, and at this point the anisotropy factor is maximum.

As required, the energy density is positive at the origin of the star and decrease monotonically with radius. The grey scale represents different values for central densities, being the darkest colors associated with lower densities. The remaining three panels presents radial (dotted) and tangential (dashed) pressures for different values of η. Assuming $m_s = 150\ MeV$ and $\Delta = 50\ MeV$, we have $\eta = -2000\ MeV^2$, while for the same value of m_s but with $\Delta = 100 MeV$, we found $\eta = 2900\ MeV^2$. The result of $\eta = 0$ comes from $m_s = \Delta = 0$, that reproduces the MIT EoS. Bowers and Liang (1974) discussed an additional condition stating that the anisotropy factor ($\delta = P_t - P_r$) must vanish for $r \to 0$, so the gradient of P_r is finite at the origin. This condition is also satisfied in our treatment, as we

[2] The solution for $n = 1$ resulted in constant energy density and radial pressure, violating the criteria of a null radial pressure at the surface.

can see at the figures, despite the fact that tangential pressure is maximum at the surface of the star. The nature of P_t is beyond the scope of our work, but we emphasize that it is not necessarily required that it vanishes at $r = R$. It is important to note that it is the cancellation of the radial pressure at the surface that guarantees that the Schwarzschild matches at this point.

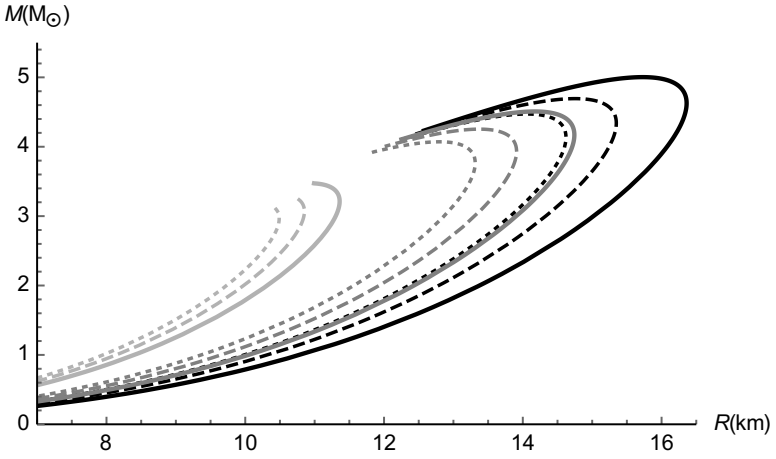

Figure 5.4: Mass-radius relation using Thirukkanesh-Ragel ansatz. Solid lines assumes $\Delta = 100$ MeV and $m_s = 150$ MeV, while the dashed lines assumes $\Delta = m_s = 0$ MeV (resembling the MIT bag model), and for dotted lines $\Delta = 50$ MeV and $m_s = 150$ MeV. From the darkest curves to the lightest ones we set $B = 115$ MeV/fm^3, $B = 70$ MeV/fm^3 and $B = 57.5$ MeV/fm^3.

The M-R relation was constructed for the three η values described before, with combinations of three different values of B, Figure (5.4). Dotted lines assumes $\eta = -2000\ MeV^2$, dashed lines assumes $\eta = 0$ and solid lines were constructed using $\eta = 2900\ MeV^2$. From the lightest to darkest curves (left to right) the bag constant increases, assuming the values of 57.5 $MeV/fm^3, 70\ MeV/fm^3$ and 115 MeV/fm^3, respectively. As can be noted, the radial increase in the tangential pressure component seems to have a huge effect on the total mass supported against gravitational collapse. The results with $B = 57.5\ MeV/fm^3$ support maximum masses up to 3 $M_\odot$, and gives room for the existence of extremely massive NSs.

5.4.2 Sharma-Maharaj ansatz

Sharma and Maharaj (2007) proposed the *ansatz*:

$$e^{-2\lambda} = 1 - \frac{br^2}{(1 + ar^2)}, \tag{5.26}$$

where a and b are positive constants. Parameter b is defined as a function of central density and a is an implicit function of ρ_c, carefully chosen to control the anisotropy in such a way that P_t approaches zero at the same point as P_r (the surface of the star). Figure (5.5) show the energy density profile and pressure profiles for the same values of η and B used in Section 5.4.1.

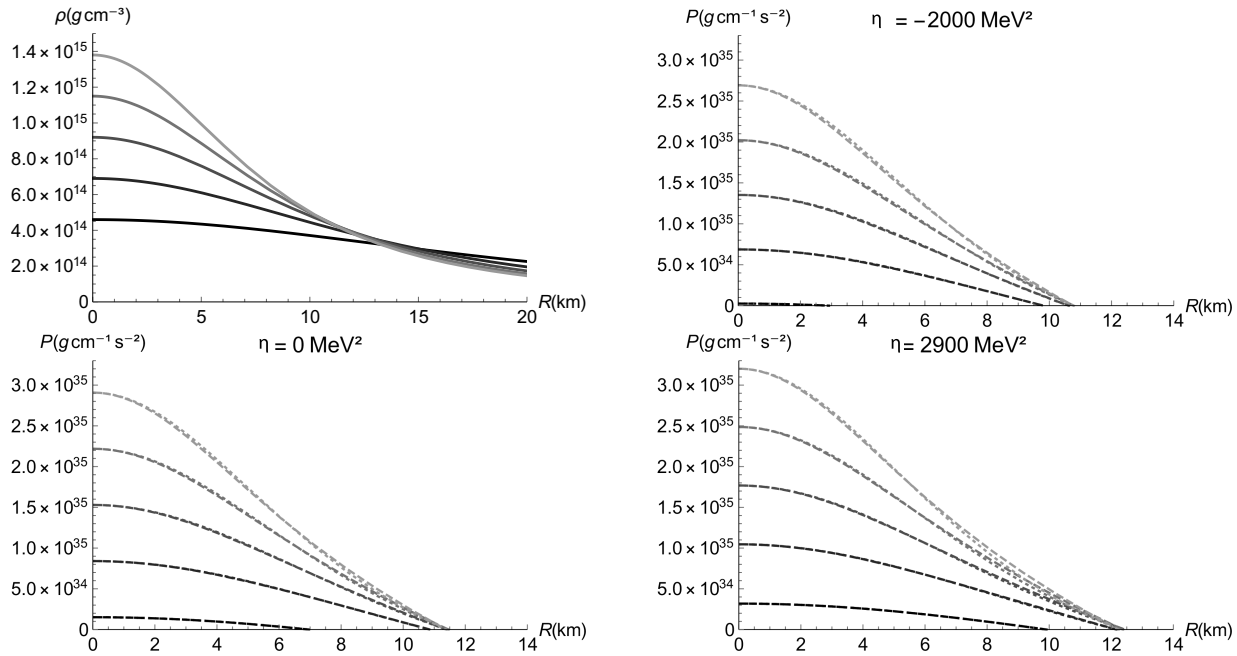

Figure 5.5: Sharma-Maharaj ansatz. The first graph (top-left) is a construction of energy density profiles monotonically decreasing with r, in which low central densities (darker curves) shows a lower decrease slope. The following three graphics represents pressure profiles, with P_r represented by dotted lines and P_t by dashed lines. For $\eta = -2000$ MeV^2 we set $m_s = 150$ MeV and $\Delta = 50$ MeV; for $\eta = 0$ MeV^2 we have $m_s = \Delta = 0$ MeV; and finally, for $\eta = 2900$ MeV^2 we fixed $m_s = 150$ MeV and $\Delta = 100$ MeV. The surface of a given star is reached when P_r vanishes, at this point the anisotropy factor also vanishes.

Energy density still positive at the origin, monotonically decreasing until it reaches the surface of the star. The difference in comparison with the previous treatment is that now we restrict the solution to those where the both pressure components *match* at the surface, i.e., the anisotropy factor (δ) is zero. Solutions with positive and negative δ at the surface are not discarded, but are more difficult to solve and were not treated in our work.

The mass-radius diagram is shown in Figure 5.6 for an unique value of bag constant, $B = 57.5 MeV/fm^3$. Given that this model is *quasi-isotropic*, since anisotropy is very mild, the anisotropy has an almost negligible effect on the total mass supported by stars.

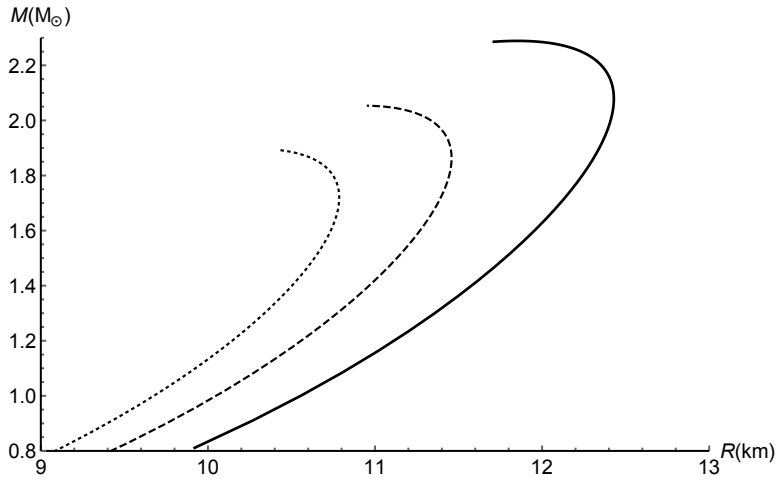

Figure 5.6: Mass-radius relation in Sharma-Maharaj ansatz. Solid lines assumes $\Delta = 100$ MeV and $m_s = 150$ MeV, the dashed lines assumes $\Delta = m_s = 0$ (resembling the MIT bag model), and for dotted lines $\Delta = 50$ MeV and $m_s = 150$ MeV. All of the curves were done for $B = 57.5$ MeV/fm^3.

5.5 Conclusions

In this chapter we worked on the construction of exact solutions under two different *ansatz* for the *Einstein Field Equations*, assuming an EoS in the CFL strange matter phase, and allowing anisotropy in the pressure. The CFL phase at zero temperature is modeled as an electrically neutral and colorless gas of quark Cooper pairs, allowing this matter to be the true ground state of strong interactions for a wide range of the parameters B, m_s and Δ. Most works in literature make use of *toy models* to construct solutions for EFE, so we emphasize that we provided a realistic EoS that completely satisfy all the necessary conditions to represent a compact star. An extended and detailed discussion of our work is found in Rocha et al. (2020b).

Since the inner composition of observed pulsars stills uncertain, discussions in the theoretical side are also of great importance to constrain physical parameters, including the macro ones, like mass and radius. As seen in Section 5.4.1, the presence of significant anisotropy leads to a maximum mass much higher than observed and expected by the scientific community at the moment. The effect of increasing both M_{max} and R_{max} in the presence of anisotropies is expected, as suggested by the work of Bowers and Liang (1974), but detailed discussions about the nature and effects it has on the matter are still necessary.

Models describing microphysics of compact objects are roughly constrained by astrophysical observations and experimental nuclear physics. The SQM hypothesis is beco-

ming favorable in recent times face to last discoveries. While the nuclear matter has difficulties to describe masses as high as $\sim$ 2.6 $M_{\odot}$, and seems impossible that the core-collapse of iron cores lead to formation of stars lighter than 1.17 $M_{\odot}$ (Suwa et al., 2018), the SQM easily accommodates both lightest and heaviest objects. The Central Compact Object recently found within the supernova remnant HESS J1731-347, previously called XMMM J173203.3-344518, has a mass of $m = 0.77^{+0.20}_{-0.17}$ $M_{\odot}$ and a radius of $R = 10.4^{+0.86}_{-0.78}$ km (Doroshenko et al., 2022), and was shown to be consistent with different models describing SS's, including the one we described in this chapter (Horvath et al., 2023). At the same time these models of SS's can account for the less massive component in the GW190814, with $m = 2.59$ $M_{\odot}$.

Chapter 6

Conclusions

At the beginning of the current century a scientific magazine published an article mentioning 11 unanswered questions of Physics whose resolutions could provide a new era in science (Haseltine, 2002). Among them is the behaviour of matter at ultrahigh densities and temperatures, a challenging topic that is directly related with neutron stars physics.

The research conducted in this Thesis aimed to deepen our understanding of neutron stars and their formation processes. Throughout the study, we explored various aspects of neutron star physics, including the analysis of their mass distribution with special interest in their maximum mass, the formation of double neutron star systems, and the construction of a viable model for very massive compact stars. By addressing these objectives, we aimed to contribute to the existing knowledge and uncover new insights into neutron star physics.

The Introduction chapter provided an overview of neutron stars, delving into concepts such as degeneracy pressure, formation scenarios, and the description of relativistic stars under the EFE. In the case of formation scenarios of NS's, we highlighted the break with previous paradigm about the existence of an unique channel, showed the most recent results supporting the birth of massive stars without necessity of accretion (Burrows et al., 2020) and commented on alternative scenarios as the AIC and double-degenerate AIC, as well as the merger of a NS with a WD (Zhong et al., 2023). In the subsection about relativistic stars we also discussed how the mass limit emerges, and its significance in understanding the behavior of neutron stars at ultra-high densities.

In Chapter 2, we conducted a statistical analysis of the mass distribution of neutron stars in galactic binary systems, where we assumed the distribution to follow a mixture of Gaussian components. Firstly, although the frequentist approach is not recommended to analyze the sample of NS masses, we applied Kolmogorov-Smirnov and Anderson-Darling

hypothesis tests to gather any conclusion about the shape of the distribution, and the result ruled out a unimodal shape. Under the Bayesian framework we first presented the result of our model selection to justify the discussion of the bimodal model only. Our findings are in line with previous studies for the location and scale of Gaussian peaks. However, the inferred maximum mass of neutron stars exceeded previous predictions, suggesting the existence of ultra-massive neutron stars. While the result of Shao et al. (2020) points to a maximum mass of $\sim 2.26\ M_{\odot}$, our analysis results in an average value of $2.6\ M_{\odot}$.

A posterior predictive check was conducted to check if the maximum masses derived for the GW170817 by different works are consistent with the maximum mass expected from the galactic population, and the result is negative. Higher values of m_{max} are indeed preferred. We also investigated the absence of a sharp cutoff in the mass distribution, and found that is unlikely that this sharp cutoff is present for large values of m_{max}. Finally, we implemented the model employed in Alsing et al. (2018); Shao et al. (2020) and discovered that the assumption of a uniform distribution for $\cos i$ can be responsible for underestimate the results. The ideal treatment would include the information of i for each binary system.

The threshold we derived for NS masses supports the NS nature of the less massive component of the GW190814, with $m = 2.59\ M_{\odot}$. Furthermore, it is in agreement with the maximum mass inferred for NS with differential rotation. These findings have significant implications for the state of matter at ultra-high densities. Although mass measurements can be subject to systematic errors in some cases and the sample is small, our results shows that it is perfectly possible that extremely massive NSs, with masses up to at least $2.6\ M_{\odot}$, exists. All statistical analysis in Chapter 2 were developed by me.

Chapter 3 was dedicated to the construction of a catalogue of double neutron star systems. An online version will be constantly updated. The goal is to provide a valuable resource that scientific groups around the world can use to investigate the characteristics and evolutionary pathways of these systems, which ultimately merge within the Hubble time. This work can also provides a foundation for future gravitational wave detections. The plots shown at Chapter 3 were made by me, and are an update of the extensive analysis on the formation of DNS systems in Tauris et al. (2017). The webpage available at `https://donutss.onrender.com/` was also developed by me during my visit to the MPIfR Bonn Group.

In Chapter 4, we developed a class of exact solutions to the EFE based on the strange

matter hypothesis, accounting for pressure anisotropies and pairing interactions between quarks, since they are expected to be present for such high-densities. The resulting mass-radius relation supports the existence of neutron stars extremely massive, and gives room for the result we found from the Bayesian analysis of observed systems. I made the analytical calculations for the both cases we discuss. The graphics were jointly constructed by me with the help of my colleague Antônio Bernardo.

Collectively, the findings from this research have significantly advanced our knowledge of neutron stars and their formation processes. The investigation into the mass distribution has revealed insights into the existence of ultra-massive neutron stars and the nature of matter at ultra-high densities. The catalog of double neutron star systems solidifies our understanding of their characteristics and evolutionary paths. Additionally, the anisotropic model for strange stars in the color-flavor locked phase contributes to our understanding of microphysics inside these unique objects.

Moving forward, there are promising avenues for future research. Incorporating new observational data will allow for a more comprehensive analysis of neutron star populations and their mass distribution. Refining the formation models for double neutron star systems will provide a more accurate understanding of their evolution and merger processes. Additionally, investigating other properties and phenomena related to neutron stars will expand our knowledge and open new avenues for exploration.

In conclusion, the research presented in this Thesis has provided significant contributions. Through the analysis of their mass distribution, the examination of double neutron star systems, and the development of an anisotropic model, we have advanced our knowledge of these fascinating celestial objects. The implications of this research extend beyond the realm of astrophysics and have implications for our understanding of ultra-high density matter and the mysteries of the universe. Continued research in this field will undoubtedly lead to further discoveries and advancements in neutron star physics.

Bibliography

Abbott B., Abbott R., Abbott T., Abraham S., Acernese F., Ackley K., Adams C., Adhikari R., Adya V., et al., GW190425: Observation of a compact binary coalescence with total mass $3.4M_{\odot}$, The Astrophysical Journal Letters, 2020, vol. 892, p. L3

Abbott B., Abbott R., Abbott T., Acernese F., Ackley K., Adams C., Adams T., Addesso P., Adhikari R., Adya V., et al., A gravitational-wave standard siren measurement of the Hubble constant, Nature, 2017a, vol. 551, p. 85

Abbott B., Abbott R., Abbott T., Acernese F., Ackley K., Adams C., Adams T., Addesso P., Adhikari R., Adya V., et al., Properties of the binary neutron star merger GW170817, Physical Review X, 2019, vol. 9, p. 011001

Abbott B., Abbott R., Adhikari R., Ajith P., Allen B., Allen G., Amin R., Anderson S., Anderson W., Arain M., et al., LIGO: the laser interferometer gravitational-wave observatory, Reports on Progress in Physics, 2009, vol. 72, p. 076901

Abbott B. P., Abbott R., Abbott T., Abernathy M., Acernese F., Ackley K., Adams C., Adams T., Addesso P., Adhikari R., et al., Properties of the binary black hole merger GW150914, Physical Review Letters, 2016, vol. 116, p. 241102

Abbott B. P., Abbott R., Abbott T., Acernese F., Ackley K., Adams C., Adams T., Addesso P., Adhikari R., Adya V. B., et al., GW170817: observation of gravitational waves from a binary neutron star inspiral, Physical review letters, 2017b, vol. 119, p. 161101

Abbott R., Abbott T., Abraham S., Acernese F., Ackley K., Adams A., Adams C., Adhikari R., Adya V., Affeldt C., et al., Population properties of compact objects from the second

LIGO–Virgo Gravitational-Wave Transient Catalog, The Astrophysical journal letters, 2021, vol. 913, p. L7

Abbott R., Abbott T., Abraham S., Acernese F., Ackley K., Adams C., Adhikari R., Adya V., Affeldt C., Agathos M., et al., GW190814: gravitational waves from the coalescence of a 23 $M_\odot$ black hole with a 2.6 $M_\odot$ compact object, The Astrophysical Journal Letters, 2020, vol. 896, p. L44

Accadia T., Acernese F., Alshourbagy M., Amico P., Antonucci F., Aoudia S., Arnaud N., Arnault C., Arun K., Astone P., et al., Virgo: a laser interferometer to detect gravitational waves, Journal of Instrumentation, 2012, vol. 7, p. P03012

Ai S., Gao H., Zhang B., What constraints on the neutron star maximum mass can one pose from GW170817 observations?, The Astrophysical Journal, 2020, vol. 893, p. 146

Akaike H., A new look at the statistical model identification, IEEE transactions on automatic control, 1974, vol. 19, p. 716

Akutsu T., Ando M., Araki S., Araya A., Arima T., Aritomi N., Asada H., Aso Y., Atsuta S., Awai K., et al., Construction of KAGRA: an underground gravitational-wave observatory, Progress of Theoretical and Experimental Physics, 2018, vol. 2018, p. 013F01

Alcock C., Farhi E., Olinto A., Strange stars, The Astrophysical Journal, 1986, vol. 310, p. 261

Alsing J., Silva H. O., Berti E., Evidence for a maximum mass cut-off in the neutron star mass distribution and constraints on the equation of state, Monthly Notices of the Royal Astronomical Society, 2018, vol. 478, p. 1377

Andersen B. C., Ransom S. M., A Fourier domain "Jerk" search for binary pulsars, The Astrophysical Journal Letters, 2018, vol. 863, p. L13

Antoniadis J., Tauris T. M., Ozel F., Barr E., Champion D. J., Freire P. C., The millisecond pulsar mass distribution: Evidence for bimodality and constraints on the maximum neutron star mass, arXiv preprint arXiv:1605.01665, 2016

Antoniadis J., Van Kerkwijk M., Koester D., Freire P., Wex N., Tauris T., Kramer M., Bassa C., The relativistic pulsar–white dwarf binary PSR J1738+ 0333–I. Mass determination and evolutionary history, Monthly Notices of the Royal Astronomical Society, 2012, vol. 423, p. 3316

Arzoumanian Z., Brazier A., Burke-Spolaor S., Chamberlin S., Chatterjee S., Christy B., Cordes J. M., Cornish N. J., Crawford F., Cromartie H. T., et al., The NANOGrav 11-year data set: high-precision timing of 45 millisecond pulsars, The Astrophysical Journal Supplement Series, 2018, vol. 235, p. 37

Atwood W., Abdo A. A., Ackermann M., Althouse W., Anderson B., Axelsson M., Baldini L., Ballet J., Band D., Barbiellini G., et al., The large area telescope on the Fermi gamma-ray space telescope mission, The Astrophysical Journal, 2009, vol. 697, p. 1071

Baade W., Zwicky F., Cosmic Rays from Super-Novae, Proceedings of the National Academy of Sciences, 1934a, vol. 20, p. 259

Baade W., Zwicky F., On super-novae, Proceedings of the National Academy of Sciences, 1934b, vol. 20, p. 254

Baade W., Zwicky F., Remarks on Super-Novae and Cosmic Rays, Phys. Rev., 1934c, vol. 46, p. 76

Babu G. J., Feigelson E. D., Astrostatistics: Goodness-of-Fit and All That!. In Astronomical Data Analysis Software and Systems XV , vol. 351 of Astronomical Society of the Pacific Conference Series, 2006, p. 127

Bailes M., Geodetic precession in binary pulsars, Astronomy and Astrophysics, 1988, vol. 202, p. 109

Barr E., Freire P., Kramer M., Champion D., Berezina M., Bassa C., Lyne A., Stappers B., A massive millisecond pulsar in an eccentric binary, Monthly Notices of the Royal Astronomical Society, 2017, vol. 465, p. 1711

Baumgarte T. W., Shapiro S. L., Shibata M., On the maximum mass of differentially rotating neutron stars, The Astrophysical Journal, 1999, vol. 528, p. L29

Bayes T., LII. An essay towards solving a problem in the doctrine of chances. By the late Rev. Mr. Bayes, FRS communicated by Mr. Price, in a letter to John Canton, AMFR S, Philosophical transactions of the Royal Society of London, 1763, pp 370–418

Bégin S., A search for fast pulsars in globular clusters, University of British Columbia, 2006, Ph.D. Thesis

Benvenuto O. G., De Vito M. A., Horvath J., Evolutionary trajectories of ultracompact "black widow" pulsars with very low mass companions, The Astrophysical Journal Letters, 2012, vol. 753, p. L33

Berezina M., Champion D., Freire P., Tauris T., Kramer M., Lyne A., Stappers B., Guillemot L., Cognard I., Barr E., et al., The discovery of two mildly recycled binary pulsars in the Northern High Time Resolution Universe pulsar survey, Monthly Notices of the Royal Astronomical Society, 2017, vol. 470, p. 4421

Bernardo J. M., Smith A. F., Bayesian theory. vol. 405, John Wiley & Sons, 2009

Berthereau A., Guillemot L., Freire P., Kramer M., Krishnan V. V., Cognard I., Theureau G., Bailes M., Bernadich M., Lower M., Radio timing constraints on the mass of the binary pulsar PSR J1528-3146, arXiv preprint arXiv:2304.06578, 2023

Bhalerao V. B., van Kerkwijk M. H., Harrison F. A., CONSTRAINTS ON THE COMPACT OBJECT MASS IN THE ECLIPSING HIGH-MASS X-RAY BINARY XMMUÂ J013236.7+303228 IN MÂ 33, The Astrophysical Journal, 2012, vol. 757, p. 10

Bhat N. R., Bailes M., Verbiest J. P., Gravitational-radiation losses from the pulsar–white-dwarf binary PSR J1141–6545, Physical Review D, 2008, vol. 77, p. 124017

Bhattacharya D., van den Heuvel E. P. J., Formation and evolution of binary and millisecond radio pulsars, Physics Reports, 1991, vol. 203, p. 1

Bodmer A., Collapsed nuclei, Physical Review D, 1971, vol. 4, p. 1601

Bonolis L., Stellar structure and compact objects before 1940: Towards relativistic astrophysics, The European Physical Journal H, 2017, pp 1–83

Bowers R. L., Liang E., Anisotropic spheres in general relativity, Astrophysical Journal, Vol. 188, p. 657 (1974), 1974, vol. 188, p. 657

Burrows A., Radice D., Vartanyan D., Nagakura H., Skinner M. A., Dolence J. C., The overarching framework of core-collapse supernova explosions as revealed by 3D FORNAX simulations, MNRAS, 2020, vol. 491, p. 2715

Burrows A., Vartanyan D., Core-collapse supernova explosion theory, Nature, 2021, vol. 589, p. 29

Cameron A., Bailes M., Balakrishnan V., Champion D., Freire P., Kramer M., Wex N., Johnston S., Lyne A., Stappers B., et al., News and views regarding PSR J1757-1854, a highly-relativistic binary pulsar, arXiv preprint arXiv:2203.15995, 2022

Carroll B. W., Ostlie D. A., An introduction to modern astrophysics. Cambridge University Press, 2017

Casares J., Dubus G., Shahbaz T., Zurita C., Charles P., VLT spectroscopy of XTE J2123-058 during quiescence: the masses of the two components, Monthly Notices of the Royal Astronomical Society, 2002, vol. 329, p. 29

Casares J., Hernández J. G., Israelian G., Rebolo R., On the mass of the neutron star in Cyg X-2, Monthly Notices of the Royal Astronomical Society, 2010, vol. 401, p. 2517

Chaisson E., McMillan S., Rice E., Astronomy today. Pearson/Prentice Hall Upper Saddle River, NJ, 2005

Chamel N., Haensel P., Zdunik J. L., Fantina A., On the maximum mass of neutron stars, International Journal of Modern Physics E, 2013, vol. 22, p. 1330018

Chodos A., Jaffe R. L., Johnson K., Thorn C. B., Weisskopf V. F., A New Extended Model of Hadrons, Phys. Rev., 1974, vol. D9, p. 3471

Clark C., Kerr M., Barr E., Bhattacharyya B., Breton R., Bruel P., Camilo F., Chen W., Cromartie H., et al., Neutron star mass estimates from gamma-ray eclipses in spider millisecond pulsar binaries, Nature Astronomy, 2023, pp 1–12

Coleman M. S. B., Burrows A., Kicks and induced spins of neutron stars at birth, MNRAS, 2022, vol. 517, p. 3938

Corongiu A., Krishnan V. V., Freire P., Kramer M., Possenti A., Geyer M., Ridolfi A., Abbate F., Bailes M., Barr E., et al., PSR˜ J1910 −5959 A: A rare gravitational laboratory for testing white dwarf models, arXiv preprint arXiv:2301.04055, 2023

Corsi A., Hallinan G., Mooley K., Frail D. A., Kasliwal M. M., Palliyaguru N. T., Growth Collaboration LIGO/VIRGO G298048: Radio detection of SSS17a at 6 GHz with the VLA, GRB Coordinates Network, 2017, vol. 21815, p. 1

Coulter D. A., Foley R. J., Kilpatrick C. D., Drout M. R., Piro A. L., Shappee B. J., Siebert M. R., Simon J. D., Ulloa N., Kasen D., Madore B. F., Murguia-Berthier A., Pan Y.-C., Prochaska J. X., Ramirez-Ruiz E., Rest A., Rojas-Bravo C., Swope Supernova Survey 2017a (SSS17a), the optical counterpart to a gravitational wave source, Science, 2017, vol. 358, p. 1556

Cromartie H. T., Fonseca E., Ransom S. M., Demorest P. B., Arzoumanian Z., Blumer H., Brook P. R., DeCesar M. E., Dolch T., Ellis J. A., et al., Relativistic Shapiro delay measurements of an extremely massive millisecond pulsar, Nature Astronomy, 2020, vol. 4, p. 72

Cruces M., Reisenegger A., Tauris T. M., On the weak magnetic field of millisecond pulsars: does it decay before accretion?, Monthly Notices of the Royal Astronomical Society, 2019, vol. 490, p. 2013

Cutler C., Flanagan É. E., Gravitational waves from merging compact binaries: How accurately can one extract the binary's parameters from the inspiral waveform\?, Phys. Rev. D, 1994, vol. 49, p. 2658

de Avellar M. G., Horvath J., Exact and quasi-exact models of strange stars, International Journal of Modern Physics D, 2010, vol. 19, p. 1937

Delgaty M. S. R., Lake K., Physical acceptability of isolated, static, spherically symmetric, perfect fluid solutions of Einstein's equations, Computer Physics Communications, 1998, vol. 115, p. 395

Deller A., Archibald A., Brisken W., Chatterjee S., Janssen G., Kaspi V., Lorimer D., Lyne A., McLaughlin M., Ransom S., et al., A parallax distance and mass estimate for the

transitional millisecond pulsar system J1023+ 0038, The Astrophysical Journal Letters, 2012, vol. 756, p. L25

Deller A., Bailes M., Andreoni I., Bannister K., Cooke J., Dobie D., Kaplan D., Lynch C., Murphy T., OzGrav VAST Collaboration. LIGO/Virgo G298048: VLBA upper limits at 8.7GHz for the GW counterpart SSS17a/DLT17ck on August 20-21 UT, GRB Coordinates Network, 2017, vol. 21850, p. 1

Deller A., Bailes M., Andreoni I., Bannister K., Cooke J., Dobie D., Kaplan D., Lynch C., Murphy T., OzGrav Collaboration VAST Collaboration. LIGO/Virgo G298048: VLBA observations of the possible counterpart SSS17a in NGC 4993, GRB Coordinates Network, 2017, vol. 21588, p. 1

Demorest P. B., Pennucci T., Ransom S., Roberts M., Hessels J., A two-solar-mass neutron star measured using Shapiro delay, Nature, 2010, vol. 467, p. 1081

Deng Z.-L., Gao Z.-F., Li X.-D., Shao Y., On the Formation of PSR J1640+2224: A Neutron Star Born Massive?, The Astrophysical Journal, 2020, vol. 892, p. id.4

Dessart L., Burrows A., Ott C., Livne E., Yoon S.-Y., Langer N., Multidimensional simulations of the accretion-induced collapse of white dwarfs to neutron stars, The Astrophysical Journal, 2006, vol. 644, p. 1063

Desvignes G., Caballero R., Lentati L., Verbiest J., Champion D., Stappers B., Janssen G., Lazarus P., Osłowski S., Babak S., et al., High-precision timing of 42 millisecond pulsars with the European Pulsar Timing Array, Monthly Notices of the Royal Astronomical Society, 2016, vol. 458, p. 3341

Doherty C. L., Gil-Pons P., Siess L., Lattanzio J. C., Super-AGB Stars and their role as Electron Capture Supernova progenitors, Publications of the Astronomical Society of Australia, 2017, vol. 34, p. e056

Doherty C. L., Gil-Pons P., Siess L., Lattanzio J. C., Lau H. H. B., Super- and massive AGB stars - IV. Final fates - initial-to-final mass relation, Monthly Notices of the Royal Astronomical Society, 2015, vol. 446, p. 2599

Doroshenko V., Suleimanov V., Pühlhofer G., Santangelo A., A strangely light neutron star within a supernova remnant, Nature Astronomy, 2022, pp 1–8

Eddington A. S., Stars and atoms. vol. 10, Yale University Press, 1927

Eldridge J. J., Tout C. A., The progenitors of core-collapse supernovae, Monthly Notices of the Royal Astronomical Society, 2004, vol. 353, p. 87

Ertl T., Woosley S. E., Sukhbold T., Janka H.-T., The Explosion of Helium Stars Evolved with Mass Loss, The Astrophysical Journal, 2020, vol. 890, p. 51

Falanga M., Bozzo E., Lutovinov A., Bonnet-Bidaud J., Fetisova Y., Puls J., Ephemeris, orbital decay, and masses of ten eclipsing high-mass X-ray binaries, Astronomy & Astrophysics, 2015, vol. 577, p. A130

Ferdman R., Freire P., Perera B., Pol N., Camilo F., Chatterjee S., Cordes J., Crawford F., Hessels J., Kaspi V., et al., Asymmetric mass ratios for bright double neutron-star mergers, Nature, 2020, vol. 583, p. 211

Ferdman R. D., Stairs I. H., Kramer M., Janssen G. H., Bassa C. G., Stappers B. W., Demorest P. B., Cognard I., Desvignes G., Theureau G., et al., PSR J1756- 2251: a pulsar with a low-mass neutron star companion, Monthly Notices of the Royal Astronomical Society, 2014, vol. 443, p. 2183

Ferdman R. D., Stairs I. H., Kramer M., McLaughlin M. A., Lorimer D. R., Nice D. J., Manchester R. N., Hobbs G., Lyne A. G., Camilo F., et al., A Precise Mass Measurement of the Intermediate-Mass Binary Pulsar PSR J1802–2124, The Astrophysical Journal, 2010, vol. 711, p. 764

Finn L. S., Observational constraints on the neutron star mass distribution, Physical Review Letters, 1994, vol. 73, p. 1878

Fonseca E., Cromartie H. T., Pennucci T. T., Ray P. S., Kirichenko A. Y., Ransom S. M., Demorest P. B., Stairs I. H., Arzoumanian Z., Guillemot L., et al., Refined mass and geometric measurements of the high-mass PSR J0740+ 6620, The Astrophysical Journal Letters, 2021, vol. 915, p. L12

Fonseca E., Stairs I. H., Thorsett S. E., A comprehensive study of relativistic gravity using PSR B1534+ 12, The Astrophysical Journal, 2014, vol. 787, p. 82

Fortin M., Bejger M., Haensel P., Zdunik J., Progenitor neutron stars of the lightest and heaviest millisecond pulsars, Astronomy & Astrophysics, 2016, vol. 586, p. A109

Fowler R. H., On dense matter, Monthly Notices of the Royal Astronomical Society, 1926, vol. 87, p. 114

Freedman W. L., Madore B. F., Gibson B. K., Ferrarese L., Kelson D. D., Sakai S., Mould J. R., Kennicutt Robert C. J., Ford H. C., Graham J. A., Huchra J. P., Hughes S. M. G., Illingworth G. D., Macri L. M., Stetson P. B., Final Results from the Hubble Space Telescope Key Project to Measure the Hubble Constant, ApJ, 2001, vol. 553, p. 47

Freire P. C., Wolszczan A., van den Berg M., Hessels J. W., A massive neutron star in the globular cluster M5, The Astrophysical Journal, 2008, vol. 679, p. 1433

Fryer C., Benz W., Herant M., Colgate S. A., What can the accretion-induced collapse of white dwarfs really explain?, The Astrophysical Journal, 1999, vol. 516, p. 892

Gao H., Lei W.-H., Zhu Z.-P., GRB 211211A: a Prolonged Central Engine under a Strong Magnetic Field Environment, ApJ, 2022, vol. 934, p. L12

Gell-Mann M., A schematic model of baryons and mesons, Physics Letters, 1964, vol. 8, p. 214

Geyer M., Krishnan V. V., Freire P., Kramer M., Antoniadis J., Bailes M., Bernadich M., Buchner S., Cameron A., Champion D., et al., Mass measurements and 3D orbital geometry of PSR J1933 −6211, arXiv preprint arXiv:2304.09060, 2023

Gold T., Rotating Neutron Stars as the Origin of the Pulsating Radio Sources, Nature, 1968, vol. 218, p. 731

Goldstein A., Veres P., Burns E., Briggs M. S., Hamburg R., Kocevski D., Wilson-Hodge C. A., Preece R. D., Poolakkil S., Roberts O. J., Hui C. M., Connaughton V., Racusin J., von Kienlin A., Canton T. D., Christensen N., Littenberg T., Siellez K., Blackburn L., Broida J., Bissaldi E., Cleveland W. H., Gibby M. H., Giles M. M., Kippen R. M.,

McBreen S., McEnery J., Meegan C. A., Paciesas W. S., Stanbro M., An Ordinary Short Gamma-Ray Burst with Extraordinary Implications: Fermi-GBM Detection of GRB 170817A, The Astrophysical Journal, 2017, vol. 848, p. L14

Gompertz B. P., Ravasio M. E., Nicholl M., Levan A. J., Metzger B. D., Oates S. R., Lamb G. P., Fong W.-f., Malesani D. B., Rastinejad J. C., et al., The case for a minute-long merger-driven gamma-ray burst from fast-cooling synchrotron emission, Nature Astronomy, 2023, vol. 7, p. 67

Grindlay J., Bailyn C., Birth of millisecond pulsars in globular clusters, Nature, 1988, vol. 336, p. 48

Guo Y., Freire P., Guillemot L., Kramer M., Zhu W., Wex N., McKee J., Deller A., Ding H., Kaplan D., et al., PSR J2222- 0137-I. Improved physical parameters for the system, Astronomy & Astrophysics, 2021, vol. 654, p. A16

Haniewicz H. T., Ferdman R. D., Freire P. C., Champion D. J., Bunting K. A., Lorimer D. R., McLaughlin M. A., Precise mass measurements for the double neutron star system J1829+ 2456, Monthly Notices of the Royal Astronomical Society, 2021, vol. 500, p. 4620

Harrison E. R., Tademaru E., Acceleration of pulsars by asymmetric radiation., ApJ, 1975, vol. 201, p. 447

Haseltine E., The 11 greatest unanswered questions of physics, DISCOVER-NEW YORK-, 2002, vol. 23, p. 36

HASTINGS W., Monte Carlo sampling methods using Markov chains and their applications, Biometrika, 1970, vol. 57, p. 97

Hewish A., Bell S. J., Pilkington J. D., Scott P. F., Collins R. A., Observation of a rapidly pulsating radio source, Nature, 1968, vol. 217, p. 709

Hiramatsu D., Howell D. A., Van Dyk S. D., Goldberg J. A., Maeda K., Moriya T. J., Tominaga N., Nomoto K., Hosseinzadeh G., Arcavi I., et al., The electron-capture origin of supernova 2018zd, Nature Astronomy, 2021, vol. 5, p. 903

Hobbs G., Manchester R., Teoh A., Hobbs M., The ATNF pulsar catalog. In Young Neutron Stars and Their Environments , vol. 218, 2004, p. 139

Horvath J., Bernardo A., Rocha L., Valentim R., Moraes P., de Avellar M., Redback/Black Widow Systems as progenitors of the highest neutron star masses and low-mass Black Holes, SCIENCE CHINA Physics, Mechanics & Astronomy, 2020, vol. 63, p. id.129531

Horvath J., Rocha L., de Sá L., Moraes P., Barão L., de Avellar M., Bernardo A., Bachega R., A light strange star in the remnant HESS J1731-347: minimal consistency checks, arXiv preprint arXiv:2303.10264, 2023

Horvath J. E., Rocha L. S., Bernardo A. L., de Avellar M. G., Valentim R., , 2023 in , Astrophysics in the XXI Century with Compact Stars. World Scientific pp 1–51

Horvath J. E., Valentim R., The Masses of Neutron Stars, Handbook of Supernovae, 2017, p. 1317

Hulse R. A., Taylor J. H., Discovery of a pulsar in a binary system, The Astrophysical Journal, 1975, vol. 195, p. L51

Iaconi R., Reichardt T., Staff J., De Marco O., Passy J.-C., Price D., Wurster J., Herwig F., The effect of a wider initial separation on common envelope binary interaction simulations, Monthly Notices of the Royal Astronomical Society, 2016, vol. 464, p. 4028

Jacoby B. A., Cameron P., Jenet F., Anderson S., Murty R., Kulkarni S., Measurement of orbital decay in the double neutron star binary PSR B2127+ 11C, The Astrophysical Journal Letters, 2006, vol. 644, p. L113

Janka H.-T., Neutron star kicks by the gravitational tug-boat mechanism in asymmetric supernova explosions: progenitor and explosion dependence, The Astrophysical Journal, 2017, vol. 837, p. 84

Janka H.-T., Wongwathanarat A., Kramer M., Supernova Fallback as Origin of Neutron Star Spins and Spin-kick Alignment, ApJ, 2022, vol. 926, p. 9

Janssen G., Stappers B., Kramer M., Nice D., Jessner A., Cognard I., Purver M., Multi-telescope timing of PSR J1518+ 4904, Astronomy & Astrophysics, 2008, vol. 490, p. 753

Joss P., Rappaport S., Observational constraints on the masses of neutron stars, Nature, 1976, vol. 264, p. 219

Kandel D., Romani R. W., Atmospheric circulation on black widow companions, The Astrophysical Journal, 2020, vol. 892, p. 101

Kandel D., Romani R. W., An Optical Study of the Black Widow Population, The Astrophysical Journal, 2022, vol. 942, p. 6

Kandel D., Romani R. W., Filippenko A. V., Brink T. G., Zheng W., Heated Poles on the Companion of Redback PSR J2339–0533, The Astrophysical Journal, 2020, vol. 903, p. 39

Kansabanik D., Bhattacharyya B., Roy J., Stappers B., Unraveling the Eclipse Mechanism of a Binary Millisecond Pulsar Using Broadband Radio Spectra, The Astrophysical Journal, 2021, vol. 920, p. 58

Kasian L. E., Radio observations of two binary pulsars, University of British Columbia, 2012, Ph.D. Thesis

Kass R. E., Raftery A. E., Bayes factors, Journal of the american statistical association, 1995, vol. 90, p. 773

Kennedy M. R., Breton R., Clark C., Mata Sánchez D., Voisin G., Dhillon V., Halpern J., Marsh T., Nieder L., Ray P., et al., Measuring the mass of the black widow PSR J1555-2908, Monthly Notices of the Royal Astronomical Society, 2022, vol. 512, p. 3001

Kidder L. E., Will C. M., Wiseman A. G., Spin effects in the inspiral of coalescing compact binaries, Phys. Rev. D, 1993, vol. 47, p. R4183

Kirichenko A. Y., Karpova A., Zyuzin D., Zharikov S., López E., Shibanov Y. A., Freire P., Fonseca E., Cabrera-Lavers A., Searching for optical companions to four binary millisecond pulsars with the Gran Telescopio Canarias, Monthly Notices of the Royal Astronomical Society, 2020, vol. 492, p. 3032

Kiziltan B., Kottas A., De Yoreo M., Thorsett S. E., The neutron star mass distribution, The Astrophysical Journal, 2013, vol. 778, p. 66

Knight A. H., Ingram A., Middleton M., Drake J., Eclipse mapping of EXO 0748–676: evidence for a massive neutron star, Monthly Notices of the Royal Astronomical Society, 2022, vol. 510, p. 4736

Kramer M., Determination of the geometry of the PSR B1913+ 16 system by geodetic precession, The Astrophysical Journal, 1998, vol. 509, p. 856

Kramer M., Stairs I., Manchester R., Wex N., Deller A., Coles W., Ali M., Burgay M., Camilo F., Cognard I., et al., Strong-field gravity tests with the double pulsar, Physical Review X, 2021, vol. 11, p. 041050

Kumar J., Bharti P., Relativistic models for anisotropic compact stars: A review, New Astronomy Reviews, 2022, p. 101662

Landau L., Origin of stellar energy, Nature, 1938, vol. 141, p. 333

Landau L. D., Zur theorie der energieubertragung ii, Z. Sowjetunion, 1932, vol. 2, p. 46

Lattimer J. M., Prakash M., Neutron Star Structure and the Equation of State, The Astrophysical Journal, 2001, vol. 550, p. 426

Lattimer J. M., Schutz B. F., Constraining the Equation of State with Moment of Inertia Measurements, The Astrophysical Journal, 2005, vol. 629, p. 979

Linares M., Super-Massive Neutron Stars and Compact Binary Millisecond Pulsars, Multifrequency Behaviour of High Energy Cosmic Sources-XIII. 3-8 June 2019. Palermo, 2020, p. 23

Linares M., Shahbaz T., Casares J., Peering into the dark side: Magnesium lines establish a massive neutron star in PSR J2215+ 5135, The Astrophysical Journal, 2018, vol. 859, p. 54

Lugones G., Horvath J., Color-flavor locked strange matter, Physical Review D, 2002, vol. 66, p. 074017

Lugones G., Horvath J. E., High-density QCD pairing in compact star structure, Astronomy & Astrophysics, 2003, vol. 403, p. 173

Lynch R. S., Freire P. C., Ransom S. M., Jacoby B. A., The timing of nine globular cluster pulsars, The Astrophysical Journal, 2012, vol. 745, p. 109

Lyne A. G., Anderson B., Salter M. J., The proper motions of 26 PSR., MNRAS, 1982, vol. 201, p. 503

McKee J., Freire P., Berezina M., Champion D., Cognard I., Graikou E., Guillemot L., Keith M., Kramer M., Lyne A., et al., A precise mass measurement of PSR J2045+ 3633, Monthly Notices of the Royal Astronomical Society, 2020, vol. 499, p. 4082

Margalit B., Berger E., Metzger B. D., Fast radio bursts from magnetars born in binary neutron star mergers and accretion induced collapse, The Astrophysical Journal, 2019, vol. 886, p. 110

Margalit B., Metzger B. D., Constraining the maximum mass of neutron stars from multi-messenger observations of GW170817, The Astrophysical Journal Letters, 2017, vol. 850, p. L19

Martinez J., Stovall K., Freire P., Deneva J., Jenet F., McLaughlin M., Bagchi M., Bates S., Ridolfi A., Pulsar J0453+ 1559: A double neutron star system with a large mass asymmetry, The Astrophysical Journal, 2015, vol. 812, p. 143

Mata Sánchez D., Istrate A. G., Van Kerkwijk M., Breton R., Kaplan D., PSR J1012+ 5307: a millisecond pulsar with an extremely low-mass white dwarf companion, Monthly Notices of the Royal Astronomical Society, 2020, vol. 494, p. 4031

Maxted N. I., Ruiter A. J., Belczynski K., Seitenzahl I. R., Crocker R. M., A supernova remnant associated with a nascent black hole low-mass X-ray binary, arXiv preprint arXiv:2010.15341, 2020

Metropolis N., Rosenbluth A. W., Rosenbluth M. N., Teller A. H., Teller E., Equation of state calculations by fast computing machines, The journal of chemical physics, 1953, vol. 21, p. 1087

Munoz-Darias T., Casares J., Martínez-Pais I., The "K-Correction" for Irradiated Emission Lines in LMXBs: Evidence for a Massive Neutron Star in X1822–371 (V691 CrA), The Astrophysical Journal, 2005, vol. 635, p. 502

Nagakura H., Sumiyoshi K., Yamada S., Possible Early Linear Acceleration of Proto-neutron Stars via Asymmetric Neutrino Emission in Core-collapse Supernovae, ApJ, 2019, vol. 880, p. L28

Nakamura K., Takiwaki T., Kotake K., Long-term simulations of multi-dimensional core-collapse supernovae: Implications for neutron star kicks, PASJ, 2019, vol. 71, p. 98

Nathanail A., Most E. R., Rezzolla L., GW170817 and GW190814: tension on the maximum mass, The Astrophysical Journal Letters, 2021, vol. 908, p. L28

Nättilä J., Miller M., Steiner A., Kajava J., Suleimanov V., Poutanen J., Neutron star mass and radius measurements from atmospheric model fits to X-ray burst cooling tail spectra, Astronomy & Astrophysics, 2017, vol. 608, p. A31

Ng C., Guillemot L., Freire P., Kramer M., Champion D., Cognard I., Theureau G., Barr E., A Shapiro delay detection in the pulsar binary system PSR J1811–2405, Monthly Notices of the Royal Astronomical Society, 2020, vol. 493, p. 1261

Nomoto K., Evolution of 8-10 solar mass stars toward electron capture supernovae. I-Formation of electron-degenerate O+ NE+ MG cores, The Astrophysical Journal, 1984, vol. 277, p. 791

Nomoto K., Evolution of 8–10 M_{sun} Stars toward Electron Capture Supernovae. II. Collapse of an O + NE + MG Core, ApJ, 1987, vol. 322, p. 206

Nomoto K., Kondo Y., Conditions for accretion-induced collapse of white dwarfs, The Astrophysical Journal, 1991, vol. 367, p. L19

Oppenheimer J. R., Volkoff G. M., On massive neutron cores, Physical Review, 1939, vol. 55, p. 374

Özel F., Freire P., Masses, radii, and the equation of state of neutron stars, Annual Review of Astronomy and Astrophysics, 2016, vol. 54, p. 401

Özel F., Psaltis D., Güver T., Baym G., Heinke C., Guillot S., The dense matter equation of state from neutron star radius and mass measurements, The Astrophysical Journal, 2016, vol. 820, p. 28

Pacini F., Energy emission from a neutron star, Nature, 1967, vol. 216, p. 567

Patton R. A., Sukhbold T., Towards a Realistic Explosion Landscape for Binary Population Synthesis, arXiv preprint arXiv:2005.03055, 2020

Paulucci L., Fornazari J., Brasil Neves K., Horvath J., Resource letter and an evaluation of the state-of-the-art of the teaching of Stellar Astrophysics, Revista Brasileira de Ensino de Física, 2022, vol. 44

Pedregosa F., Varoquaux G., Gramfort A., Michel V., Thirion B., Grisel O., Blondel M., Prettenhofer P., Weiss R., Dubourg V., et al., Scikit-learn: Machine learning in Python, the Journal of machine Learning research, 2011, vol. 12, p. 2825

Peters P. C., Gravitational radiation and the motion of two point masses, Physical Review, 1964, vol. 136, p. B1224

Podsiadlowski P., Langer N., Poelarends A., Rappaport S., Heger A., Pfahl E., The effects of binary evolution on the dynamics of core collapse and neutron star kicks, The Astrophysical Journal, 2004, vol. 612, p. 1044

Qian Y.-Z., Wasserburg G., Where, oh where has the r-process gone?, Physics Reports, 2007, vol. 442, p. 237

Rajagopal K., Wilczek F., , 2001 in , At The Frontier of Particle Physics: Handbook of QCD (In 3 Volumes). World Scientific, Singapore pp 2061–2151

Rawls M. L., Orosz J. A., McClintock J. E., Torres M. A., Bailyn C. D., Buxton M. M., Refined neutron star mass determinations for six eclipsing X-ray pulsar binaries, The Astrophysical Journal, 2011, vol. 730, p. 25

Reardon D., Hobbs G., Coles W., Levin Y., Keith M., Bailes M., Bhat N., Burke-Spolaor S., Dai S., Kerr M., et al., Timing analysis for 20 millisecond pulsars in the Parkes Pulsar Timing Array, Monthly Notices of the Royal Astronomical Society, 2016, vol. 455, p. 1751

Reardon D. J., Shannon R. M., Cameron A. D., Goncharov B., Hobbs G., Middleton H., Shamohammadi M., Thyagarajan N., Bailes M., Bhat N., et al., The Parkes pulsar timing array second data release: timing analysis, Monthly Notices of the Royal Astronomical Society, 2021, vol. 507, p. 2137

Rezzolla L., Most E. R., Weih L. R., Using gravitational-wave observations and quasi-universal relations to constrain the maximum mass of neutron stars, The Astrophysical Journal Letters, 2018, vol. 852, p. L25

Rezzolla L., Pizzochero P., Jones D. I., Rea N., Vidaña I., The physics and astrophysics of neutron stars. Springer, Berlin, 2018

Rhoades Jr C. E., Ruffini R., Maximum mass of a neutron star, Physical Review Letters, 1974, vol. 32, p. 324

Ridolfi A., Freire P. C., Gupta Y., Ransom S. M., Upgraded Giant Metrewave Radio Telescope timing of NGC 1851A: a possible millisecond pulsar- neutron star system, Monthly Notices of the Royal Astronomical Society, 2019, vol. 490, p. 3860

Riley T. E., Watts A. L., Bogdanov S., Ray P. S., Ludlam R. M., Guillot S., Arzoumanian Z., Baker C. L., Bilous A. V., Chakrabarty D., et al., A NICER view of PSR J0030+ 0451: millisecond pulsar parameter estimation, The Astrophysical Journal Letters, 2019, vol. 887, p. L21

Riley T. E., Watts A. L., Ray P. S., Bogdanov S., Guillot S., Morsink S. M., Bilous A. V., Arzoumanian Z., Choudhury D., Deneva J. S., et al., A NICER view of the massive pulsar PSR J0740+ 6620 informed by radio timing and XMM-Newton spectroscopy, The Astrophysical Journal Letters, 2021, vol. 918, p. L27

Rocha L., Bernardo A., De Avellar M., Horvath J., Exact Solutions for Compact Stars with CFL Quark Matter, International Journal of Modern Physics D, 2020a, vol. 29, p. id. 2050044

Rocha L., Bernardo A., De Avellar M., Horvath J., Exact solutions for compact stars with CFL quark matter, International Journal of Modern Physics D, 2020b, vol. 29, p. 2050044

Rocha L. S., Bernardo A., Horvath J. E., Valentim R., de Avellar M. G., The distribution of neutron star masses, Astronomische Nachrichten, 2019, vol. 340, p. 957

Romani R. W., Filippenko A. V., Silverman J. M., Cenko S. B., Greiner J., Rau A., Elliott J., Pletsch H. J., PSR J1311–3430: a heavyweight neutron star with a flyweight helium companion, The Astrophysical Journal Letters, 2012, vol. 760, p. L36

Romani R. W., Kandel D., Filippenko A. V., Brink T. G., Zheng W., PSR J0952-0607: The Fastest and Heaviest Known Galactic Neutron Star, The Astrophysical Journal Letters, 2022, vol. 934, p. L18

Ruiter A., Ferrario L., Belczynski K., Seitenzahl I., Crocker R., Karakas A., On the formation of neutron stars via accretion-induced collapse in binaries, Monthly Notices of the Royal Astronomical Society, 2019, vol. 484, p. 698

Ruiz M., Shapiro S. L., Tsokaros A., GW170817, general relativistic magnetohydrodynamic simulations, and the neutron star maximum mass, Physical Review D, 2018, vol. 97, p. 021501

Rutherford E., LXXIX. The scattering of α and β particles by matter and the structure of the atom, The London, Edinburgh, and Dublin Philosophical Magazine and Journal of Science, 1911, vol. 21, p. 669

Safarzadeh M., Ramirez-Ruiz E., Andrews J. J., Macias P., Fragos T., Scannapieco E., r-process Enrichment of the Ultra-faint Dwarf Galaxies by Fast-merging Double-neutron Stars, ApJ, 2019, vol. 872, p. 105

Schmitt A., Dense matter in compact stars: A pedagogical introduction. vol. 811, Springer, 2010

Schutz B., A first course in general relativity. Cambridge university press, 2009

Schwab J., Podsiadlowski P., Rappaport S., Further evidence for the bimodal distribution of neutron-star masses, The Astrophysical Journal, 2010, vol. 719, p. 722

Schwarz G., Estimating the dimension of a model, The annals of statistics, 1978, pp 461–464

Serylak M., Krishnan V. V., Freire P., Tauris T., Kramer M., Geyer M., Parthasarathy A., Bailes M., i Bernadich M., Buchner S., et al., The eccentric millisecond pulsar, PSR J0955- 6150-I. Pulse profile analysis, mass measurements, and constraints on binary evolution, Astronomy & Astrophysics, 2022, vol. 665, p. A53

Shahbaz T., Linares M., Breton R., Properties of the redback millisecond pulsar binary 3FGL J0212. 1+ 5320, Monthly Notices of the Royal Astronomical Society, 2017, vol. 472, p. 4287

Shamohammadi M., Bailes M., Freire P. C., Parthasarathy A., Reardon D. J., Shannon R. M., Krishnan V. V., Bernadich M. i., Cameron A., Champion D., et al., Searches for

Shapiro delay in seven binary pulsars using the MeerKAT telescope, Monthly Notices of the Royal Astronomical Society, 2022

Shao D.-S., Tang S.-P., Sheng X., Jiang J.-L., Wang Y.-Z., Jin Z.-P., Fan Y.-Z., Wei D.-M., Estimating the maximum gravitational mass of nonrotating neutron stars from the GW170817/GRB 170817A/AT2017gfo observation, Physical Review D, 2020, vol. 101, p. 063029

Sharma R., Maharaj S., A class of relativistic stars with a linear equation of state, Monthly Notices of the Royal Astronomical Society, 2007, vol. 375, p. 1265

Sharma S., Markov chain Monte Carlo methods for Bayesian data analysis in astronomy, Annual Review of Astronomy and Astrophysics, 2017, vol. 55, p. 213

Shibata M., Zhou E., Kiuchi K., Fujibayashi S., Constraint on the maximum mass of neutron stars using GW170817 event, Physical Review D, 2019, vol. 100, p. 023015

Shklovskii I., Possible Causes of the Secular Increase in Pulsar Periods., Soviet Astronomy, 1970, vol. 13, p. 562

Siess L., Evolution of massive AGB stars. II. model properties at non-solar metallicity and the fate of Super-AGB stars, Astronomy & Astrophysics, 2007, vol. 473, p. 893

Spitkovsky A., Time-dependent Force-free Pulsar Magnetospheres: Axisymmetric and Oblique Rotators, The Astrophysical Journal, 2006, vol. 648, p. L51

Spruit H., Phinney E. S., Birth kicks as the origin of pulsar rotation, Nature, 1998, vol. 393, p. 139

Stairs I. H., Testing general relativity with pulsar timing, Living Reviews in Relativity, 2003, vol. 6, p. 5

Steeghs D., Jonker P., On the Mass of the Neutron Star in V395 Carinae/2S 0921–630, The Astrophysical Journal Letters, 2007, vol. 669, p. L85

Stovall K., Freire P., Antoniadis J., Bagchi M., Deneva J., Garver-Daniels N., Martinez J., McLaughlin M., Arzoumanian Z., Blumer H., et al., PSR J2234+ 0611: a new laboratory for Stellar evolution, The Astrophysical Journal, 2019, vol. 870, p. 74

Strader J., Swihart S., Chomiuk L., Bahramian A., Britt C., Cheung C., Dage K., Halpern J., Li K.-L., Mignani R. P., et al., Optical spectroscopy and demographics of redback millisecond pulsar binaries, The Astrophysical Journal, 2019, vol. 872, p. 42

Sukhbold T., Ertl T., Woosley S., Brown J. M., Janka H.-T., Core-collapse supernovae from 9 to 120 solar masses based on neutrino-powered explosions, The Astrophysical Journal, 2016, vol. 821, p. 38

Suwa Y., Yoshida T., Shibata M., Umeda H., Takahashi K., On the minimum mass of neutron stars, Monthly Notices of the Royal Astronomical Society, 2018, vol. 481, p. 3305

Sweatman M. B., Zodiacal Dating Prehistoric Artworks, Mediterranean Archaeology and Archaeometry, 2017, vol. 17

Tauris T., Kramer M., Freire P., Wex N., Janka H.-T., Langer N., Podsiadlowski P., Bozzo E., Chaty S., Kruckow M., et al., Formation of double neutron star systems, The Astrophysical Journal, 2017, vol. 846, p. 170

Tauris T., Van Den Heuvel E., Formation and evolution of compact stellar X-ray sources, Compact stellar X-ray sources, 2006, vol. 39, p. 623

Tauris T. M., Bailes M., , 1996 Technical report The origin of millisecond pulsar velocities. SCAN-9702124

Tauris T. M., Langer N., Podsiadlowski P., Ultra-stripped supernovae: progenitors and fate, MNRAS, 2015, vol. 451, p. 2123

Taylor J. H., Weisberg J. M., A new test of general relativity-Gravitational radiation and the binary pulsar PSR 1913+ 16, The Astrophysical Journal, 1982, vol. 253, p. 908

Team S., et al.,, 2020 Stan modeling language users guide and reference manual.

Terazawa H., Akama K., Chikashige Y., How to liberate quarks from chromodynamical confinement, Progress of Theoretical Physics, 1978, vol. 60, p. 1521

Thirukkanesh S., Ragel F., Exact anisotropic sphere with polytropic equation of state, PRAMANA-Journal of physics, 2012, vol. 78, p. 687

Thorsett S. E., Chakrabarty D., Neutron star mass measurements. I. Radio pulsars, The Astrophysical Journal, 1999, vol. 512, p. 288

Tian W., Leahy D., 20 Pairs of Real Pulsar/Supernova Remnant Associations. In Symposium-International Astronomical Union , vol. 218, 2004, p. 137

Timmes F., Woosley S., Weaver T. A., The Neutron Star and Black Hole Initial Mass Function, The Astrophysical Journal, 1996, vol. 457, p. 834

Tolman R. C., Static solutions of Einstein's field equations for spheres of fluid, Physical Review, 1939, vol. 55, p. 364

Ugliano M., Janka H.-T., Marek A., Arcones A., Progenitor-explosion connection and remnant birth masses for neutrino-driven supernovae of iron-core progenitors, The Astrophysical Journal, 2012, vol. 757, p. 69

Valentim R., Rangel E., Horvath J. E., On the mass distribution of neutron stars, Monthly Notices of the Royal Astronomical Society, 2011, vol. 414, p. 1427

van den Heuvel E., X-ray binaries and their descendants: binary radio pulsars; evidence for three classes of neutron stars?, arXiv preprint astro-ph/0407451, 2004

van den Heuvel E. P., High-Mass X-ray Binaries: progenitors of double compact objects, Proceedings of the International Astronomical Union, 2018, vol. 14, p. 1

Van Kerkwijk M., Breton R., Kulkarni S., Evidence for a Massive Neutron Star from a Radial-velocity Study of the Companion to the Black-widow Pulsar PSR B1957+ 20, The Astrophysical Journal, 2011, vol. 728, p. 95

Van Leeuwen J., Kasian L., Stairs I. H., Lorimer D., Camilo F., Chatterjee S., Cognard I., Desvignes G., Freire P., Janssen G., et al., The binary companion of young, relativistic pulsar J1906+ 0746, The Astrophysical Journal, 2015, vol. 798, p. 118

Voisin G., Cognard I., Freire P. C., Wex N., Guillemot L., Desvignes G., Kramer M., Theureau G., An improved test of the strong equivalence principle with the pulsar in a triple star system, Astronomy & Astrophysics, 2020, vol. 638, p. A24

Wang B., Liu D., The formation of neutron star systems through accretion-induced collapse in white-dwarf binaries, arXiv preprint arXiv:2005.01880, 2020

Weber F., Pulsars as astrophysical laboratories for nuclear and particle physics. CRC Press, 1999

Weisberg J. M., Nice D. J., Taylor J. H., Timing measurements of the relativistic binary pulsar PSR B1913+ 16, The Astrophysical Journal, 2010, vol. 722, p. 1030

Welther B. L., The discovery of Sirius B: a case of strategy or serendipity?, Journal of the American Association of Variable Star Observers (JAAVSO), 1987, vol. 16, p. 34

Witten E., Cosmic separation of phases, Phys. Rev. D, 1984, vol. 30, p. 272

Wolfram S., Mathematica Edition: Version 12.2; Wolfram Research, Inc.: Champaign, IL, USA, 2020

Woosley S., Sukhbold T., Janka H.-T., The Birth Function for Black Holes and Neutron Stars in Close Binaries, The Astrophysical Journal, 2020, vol. 896, p. 56

Ye C., Fishbach M., Inferring the Neutron Star Maximum Mass and Lower Mass Gap in Neutron Star–Black Hole Systems with Spin, The Astrophysical Journal, 2022, vol. 937, p. 73

Zhang C., Wang J., Zhao Y., Yin H., Song L., Menezes D., Wickramasinghe D., Ferrario L., Chardonnet P., Study of measured pulsar masses and their possible conclusions, Astronomy & Astrophysics, 2011, vol. 527, p. A83

Zhong S.-Q., Li L., Dai Z.-G., GRB 211211A: A Neutron Star–White Dwarf Merger?, The Astrophysical Journal Letters, 2023, vol. 947, p. L21

Zhu W., Freire P., Knispel B., Allen B., Stappers B., Lyne A., Chatterjee S., Cordes J., Crawford F., Deneva J., et al., Mass measurements for two binary pulsars discovered in the PALFA survey, The Astrophysical Journal, 2019, vol. 881, p. 165

Zhu X., Thrane E., Osłowski S., Levin Y., Lasky P. D., Inferring the population properties of binary neutron stars with gravitational-wave measurements of spin, Phys. Rev. D, 2018, vol. 98, p. 043002

Zweig G., AN su3 MODEL FOR STRONG INTERACTION SYMMETRY AND ITS BREAKING II*, 1964

Appendix

Appendix A

Sample of neutron stars masses in galactic binary system

Table A.1 - Neutron Star mass measurements for 112 NS binary systems displayed at Fig. 3.1 with 1σ uncertainties.

Object	**Type**	**Mass**($M_\odot$)	**Reference**
2S 0921-630	X-ray/Optical	$1.44^{+0.10}_{-0.10}$	Steeghs and Jonker (2007)
4U 1538-522	X-ray/Optical	$1.02^{+0.17}_{-0.17}$	Falanga et al. (2015)
4U 1608-52	X-ray/Optical	$1.57^{+0.30}_{-0.29}$	Özel et al. (2016)
4U 1700-377	X-ray/Optical	$1.96^{+0.19}_{-0.19}$	Falanga et al. (2015)
4U 1702-429	X-ray/Optical	$1.90^{+0.30}_{-0.30}$	Nättilä et al. (2017)
4U 1724-307	X-ray/Optical	$1.81^{+0.25}_{-0.37}$	Özel et al. (2016)
4U 1820-30	X-ray/Optical	$1.77^{+0.25}_{-0.28}$	Özel et al. (2016)
4U 1822-371	X-ray/Optical	$1.96^{+0.36}_{-0.35}$	Munoz-Darias et al. (2005)
B1957+20	X-ray/Optical	$2.40^{+0.12}_{-0.12}$	Van Kerkwijk et al. (2011)
Cen X-3	X-ray/Optical	$1.57^{+0.16}_{-0.16}$	Rawls et al. (2011)
Cyg X-2	X-ray/Optical	$1.71^{+0.21}_{-0.21}$	Casares et al. (2010)
EXO 0748-676	X-ray/Optical	$2.01^{+0.21}_{-0.21}$	Knight et al. (2022)
EXO 1722-363	X-ray/Optical	$1.91^{+0.45}_{-0.45}$	Falanga et al. (2015)
EXO 1745-248	X-ray/Optical	$1.65^{+0.21}_{-0.31}$	Özel et al. (2016)
Her X-1	X-ray/Optical	$1.073^{+0.358}_{-0.358}$	Rawls et al. (2011)
J01326.7+303228	X-ray/Optical	$2.0^{+0.40}_{-0.40}$	Bhalerao et al. (2012)
J0212.1+5320	X-ray/Optical	$1.85^{+0.32}_{-0.26}$	Shahbaz et al. (2017)
J0427.9-6704	X-ray/Optical	$1.86^{+0.11}_{-0.11}$	Strader et al. (2019)
J0846.0+2820	X-ray/Optical	$1.96^{+0.41}_{-0.41}$	Strader et al. (2019)
J0952-0607	X-ray/Optical	$2.35^{+0.17}_{-0.17}$	Romani et al. (2022)
J1301+0833	X-ray/Optical	$1.60^{+0.22}_{-0.25}$	Kandel and Romani (2022)
J1311-3430	X-ray/Optical	$2.22^{+0.10}_{-0.10}$	Kandel and Romani (2022)
J1417.7-4407	X-ray/Optical	$1.62^{+0.43}_{-0.17}$	Strader et al. (2019)
J1555-2908	X-ray/Optical	$1.67^{+0.07}_{-0.05}$	Kennedy et al. (2022)
J1653-0158	X-ray/Optical	$2.15^{+0.16}_{-0.16}$	Kandel and Romani (2022)
J1723-2837	X-ray/Optical	$1.22^{+0.26}_{-0.20}$	Strader et al. (2019)

To be continued...

Tabela A.1 – ...continued

Object	Type	Mass($M_\odot$)	Reference
J1810+1744	X-ray/Optical	$2.11^{+0.04}_{-0.04}$	Kandel and Romani (2022)
J2039.6-5618	X-ray/Optical	$2.04^{+0.37}_{-0.25}$	Strader et al. (2019)
J2129-0429	X-ray/Optical	$1.74^{+0.18}_{-0.18}$	Strader et al. (2019)
J2215+5135	X-ray/Optical	$2.27^{+0.17}_{-0.15}$	Linares et al. (2018)
J2339-0533	X-ray/Optical	$1.47^{+0.09}_{-0.09}$	Kandel et al. (2020)
KS 1731-260	X-ray/Optical	$1.61^{+0.35}_{-0.37}$	Özel et al. (2016)
LMC X-4	X-ray/Optical	$1.57^{+0.11}_{-0.11}$	Falanga et al. (2015)
OAO 1657-415	X-ray/Optical	$1.74^{+0.30}_{-0.30}$	Falanga et al. (2015)
SAX J1748.9-2021	X-ray/Optical	$1.81^{+0.25}_{-0.37}$	Özel et al. (2016)
SAX J1802.7-2017	X-ray/Optical	$1.57^{+0.25}_{-0.25}$	Falanga et al. (2015)
SMC X-1	X-ray/Optical	$1.21^{+0.12}_{-0.12}$	Falanga et al. (2015)
Vela X-1	X-ray/Optical	$2.12^{+0.16}_{-0.16}$	Falanga et al. (2015)
XTE J1855-026	X-ray/Optical	$1.41^{+0.24}_{-0.24}$	Falanga et al. (2015)
XTE J2123-058	X-ray/Optical	$1.53^{+0.30}_{-0.42}$	Casares et al. (2002)
B1534+12	DNS	$1.3332^{+0.0010}_{-0.0010}$	Fonseca et al. (2014)
B1534+12Cp	DNS	$1.3452^{+0.0010}_{-0.0010}$	Fonseca et al. (2014)
B1913+16	DNS	$1.4398^{+0.0002}_{-0.0002}$	Weisberg et al. (2010)
B1913+16Cp	DNS	$1.3886^{+0.0002}_{-0.0002}$	Weisberg et al. (2010)
B2127-11C	DNS	$1.358^{+0.010}_{-0.010}$	Jacoby et al. (2006)
B2127-11CCp	DNS	$1.354^{+0.010}_{-0.010}$	Jacoby et al. (2006)
J0453+1559	DNS	$1.559^{+0.004}_{-0.004}$	Martinez et al. (2015)
J0453+1559Cp	DNS	$1.174^{+0.004}_{-0.004}$	Martinez et al. (2015)
J0509+3801	DNS	$1.34^{+0.08}_{-0.08}$	Lynch et al. (2012)
J0509+3801Cp	DNS	$1.46^{+0.08}_{-0.08}$	Lynch et al. (2012)
J0514-4002A	DNS	$1.25^{+0.05}_{-0.05}$	Ridolfi et al. (2019)
J0514-4002ACp	DNS	$1.22^{+0.05}_{-0.05}$	Ridolfi et al. (2019)
J0737-3039A	DNS	$1.338185^{+0.000012}_{-0.000014}$	Kramer et al. (2021)
J0737-3039B	DNS	$1.248868^{+0.000013}_{-0.000011}$	Kramer et al. (2021)
J1518+4904	DNS	$0.72^{+0.51}_{-0.58}$	Janssen et al. (2008)
J1518+4904Cp	DNS	$2.00^{+0.58}_{-0.51}$	Janssen et al. (2008)
J1756-2251	DNS	$1.341^{+0.007}_{-0.007}$	Ferdman et al. (2014)
J1756-2251Cp	DNS	$1.230^{+0.007}_{-0.007}$	Ferdman et al. (2014)
J1757-1854	DNS	$1.3406^{+0.0005}_{-0.0005}$	Cameron et al. (2022)
J1757-1854Cp	DNS	$1.3922^{+0.0005}_{-0.0005}$	Cameron et al. (2022)
J1807-2500B	DNS	$1.3655^{+0.0021}_{-0.0021}$	Lynch et al. (2012)
J1807-2500BCp	DNS	$1.2064^{+0.0020}_{-0.0020}$	Lynch et al. (2012)
J1829+2456	DNS	$1.306^{+0.007}_{-0.007}$	Haniewicz et al. (2021)
J1829+2456Cp	DNS	$1.299^{+0.007}_{-0.007}$	Haniewicz et al. (2021)
J1906+0746	DNS	$1.291^{+0.011}_{-0.011}$	Van Leeuwen et al. (2015)
J1906+0746Cp	DNS	$1.322^{+0.011}_{-0.011}$	Van Leeuwen et al. (2015)
J1913+1102	DNS	$1.62^{+0.03}_{-0.03}$	Ferdman et al. (2020)
J1913+1102Cp	DNS	$1.27^{+0.03}_{-0.03}$	Ferdman et al. (2020)
B1516+02B	NS-WD	$2.08^{+0.19}_{-0.19}$	Freire et al. (2008)
B1802-07	NS-WD	$1.26^{+0.08}_{-0.17}$	Thorsett and Chakrabarty (1999)
B1855+09	NS-WD	$1.54^{+0.13}_{-0.13}$	Reardon et al. (2021)

To be continued...

Tabela A.1 – ...continued

Object	Type	Mass($M_\odot$)	Reference
B2303+46	NS-WD	$1.38^{+0.06}_{-0.10}$	Thorsett and Chakrabarty (1999)
J0024-7204H	NS-WD	$1.48^{+0.03}_{-0.06}$	Kiziltan et al. (2013)
J0337+1715	NS-WD	$1.4401^{+0.0015}_{-0.0015}$	Voisin et al. (2020)
J0348+0432	NS-WD	$2.01^{+0.04}_{-0.04}$	Antoniadis et al. (2016)
J0437-4715	NS-WD	$1.44^{+0.07}_{-0.07}$	Reardon et al. (2016)
J0621+1002	NS-WD	$1.53^{+0.10}_{-0.20}$	Kasian (2012)
J0740+6620	NS-WD	$2.08^{+0.07}_{-0.07}$	Fonseca et al. (2021)
J0751+1807	NS-WD	$1.64^{+0.15}_{-0.15}$	Desvignes et al. (2016)
J0955-6150	NS-WD	$1.71^{+0.02}_{-0.02}$	Serylak et al. (2022)
J1012+5307	NS-WD	$1.72^{+0.16}_{-0.16}$	Mata Sánchez et al. (2020)
J1017-7156	NS-WD	$2.0^{+0.8}_{-0.8}$	Reardon et al. (2021)
J1022-1001	NS-WD	$1.4^{+0.5}_{-0.5}$	Reardon et al. (2021)
J1125-6014	NS-WD	$1.68^{+0.16}_{-0.16}$	Shamohammadi et al. (2022)
J1141-6545	NS-WD	$1.27^{+0.01}_{-0.01}$	Bhat et al. (2008)
J1528-3146	NS-WD	$1.61^{+0.14}_{-0.13}$	Berthereau et al. (2023)
J1600-3053	NS-WD	$2.4^{+0.5}_{-0.5}$	Reardon et al. (2021)
J1614-2230	NS-WD	$1.94^{+0.03}_{-0.03}$	Shamohammadi et al. (2022)
J1713+0747	NS-WD	$1.28^{+0.08}_{-0.08}$	Reardon et al. (2021)
J1738+0333	NS-WD	$1.47^{+0.07}_{-0.06}$	Antoniadis et al. (2012)
J1741+1351	NS-WD	$1.14^{+0.43}_{-0.25}$	Kirichenko et al. (2020)
J1748-2021B	NS-WD	$2.74^{+0.21}_{-0.21}$	Freire et al. (2008)
J1748-2446am	NS-WD	$1.649^{+0.037}_{-0.11}$	Andersen and Ransom (2018)
J1748-2446I	NS-WD	$1.91^{+0.02}_{-0.10}$	Kiziltan et al. (2013)
J1748-2446J	NS-WD	$1.79^{+0.02}_{-0.10}$	Kiziltan et al. (2013)
J1750-37A	NS-WD	$1.26^{+0.39}_{-0.36}$	Freire et al. (2008)
J1802-2124	NS-WD	$1.24^{+0.11}_{-0.11}$	Ferdman et al. (2010)
J1811-2405	NS-WD	$2.0^{+0.80}_{-0.50}$	Ng et al. (2020)
J1824-2452C	NS-WD	$1.31^{+0.04}_{-0.47}$	Bégin (2006)
J1909-3744	NS-WD	$1.45^{+0.03}_{-0.03}$	Shamohammadi et al. (2022)
J1910-5958A	NS-WD	$1.55^{+0.07}_{-0.07}$	Corongiu et al. (2023)
J1918-0642	NS-WD	$1.29^{+0.10}_{-0.09}$	Arzoumanian et al. (2018)
J1933-6211	NS-WD	$1.4^{+0.25}_{-0.25}$	Geyer et al. (2023)
J1946+3417	NS-WD	$1.828^{+0.022}_{-0.022}$	Barr et al. (2017)
J1949+3106	NS-WD	$1.34^{+0.16}_{-0.16}$	Zhu et al. (2019)
J1950+2414	NS-WD	$1.496^{+0.023}_{-0.023}$	Zhu et al. (2019)
J2043+1711	NS-WD	$1.38^{+0.12}_{-0.13}$	Arzoumanian et al. (2018)
J2045+3633	NS-WD	$1.251^{+0.021}_{-0.021}$	McKee et al. (2020)
J2053+4650	NS-WD	$1.40^{+0.21}_{-0.18}$	Berezina et al. (2017)
J2222-0137	NS-WD	$1.831^{+0.010}_{-0.010}$	Guo et al. (2021)
J2234+0611	NS-WD	$1.353^{+0.014}_{-0.017}$	Stovall et al. (2019)
J0045-7319	NS-MS	$1.58^{+0.34}_{-0.34}$	Thorsett and Chakrabarty (1999)
J1023+0038	NS-MS	$1.71^{+0.16}_{-0.16}$	Deller et al. (2012)
J1903+0327	NS-MS	$1.667^{+0.010}_{-0.021}$	Arzoumanian et al. (2018)

Appendix B

Modeling, constraints and *a priori* choices

One of the most important features of a Bayesian analysis is that they fully account for measurement uncertainties. As can be noted in Fig. 3.1 and Table A.1, some measurements are highly precise, while others are linked to large errors due to measurement methods. To proceed with the analysis, in the case of asymmetric uncertainties we took the average value for the uncertainty. For example, for PSR 4U 1724-307 with a reported mass of $m = 1.81^{+0.25}_{-0.37}\ M_{\odot}$, we assumed $m = 1.81 \pm 0.31\ M_{\odot}$. Each data was modeled as a Gaussian distribution, $P(d^i|m_p^i) = \mathcal{N}(m_i, u_i)$. We have checked that this procedure of "symmetrizing" the error bars introduces a negligible difference in the final results.

We implemented the MCMC algorithm with `pystan` (Team et al., 2020). To improve efficiency, avoid computational errors and streamline the algorithm convergence, we can set some constraints when defining model parameters. With this purpose we considered: the mean of first peak to be limited by $1 < \mu_1 < 2.5$; the mean of second peak to lie above the mean of first peak $\mu_1 < \mu_2 < 2.5$; standard deviations to be positive $\{\sigma_1, \sigma_2\} > 0$. *A priori* distributions where chosen to be $r_j \sim Beta(2, 2)$, $\mu_j \sim \mathcal{N}(1.75, 1)$ and $\sigma_j \sim \mathcal{N}(0, 2)$, with $j = 1, 2$ for both components. $Beta(\alpha, \beta)$ distribution is a family of continuous probability distributions parametrized by the shape parameters $\alpha, \beta > 0$, and is defined in the interval $[0, 1]$, satisfying that $\sum_j r_j = 1$, being the analogue of the Dirichlet distribution in the case $n = 2$. The lower truncation, m_{min} was fixed at zero. We made an attempt to include an analysis regarding the minimum of the distribution, however, the choice of an a priori that does not bias the results proved to be a little more tricky. We runned 4 parallel chains, with 10000 iterations each. The model already converges for this amount of iterations, so it is not necessary to increase the number.

A priori choices are often criticized because they are quite subjective and represents the

previous knowledge an individual have about the subject. This means that *a priori* choices can change from analysis to analysis, as well as it is updated if new evidences emerges. Highly informative priors are generally avoided since they might strongly influence final results, while non-informative priors can lead to a divergence in the calculations. Since our data carries significant information about r_i, μ_i and σ_i, their priors are not substantial and change it will not affect the results, contrary to what happens with the parameter m_{max}. The data set has not enough information about the truncation point, other than the masses of the most massive observed objects. Since the posterior distribution is a balance between likelihood and *a priori* distributions, the distribution set for m_{max} plays a significant role when marginalizing it.

We analyzed different m_{max} priors to check their influence on posterior probability, with some results shown in Table B.1. When adopting a Uniform *a priori*, the marginal posterior distribution showed a flat behaviour, without preferred values, and for this reason we choose to adopt a Gaussian distribution with a "non-negligible" standard deviation to avoid bias (a standard deviation equal to 1 had a similar behaviour of using Uniform distributions). Since the interval of values we are dealing with is small, it is more challenging to choose a balance to determine the *a priori*.

We started with a *a priori* set to $\mathcal{N}(2.15, 0.5)$, and even so the results tell us that the most likely m_{max} is around 2.5 $M_\odot$, as seen at the second column of the table. It is clear that results of the maximum mass show a tendency to increase as we increase the mean value of the *a priori*, a consequence of the low content of information in the likelihood, but the weight attributed to it is not too large, or in the case of $\mathcal{N}(2.15, 0.5)$ we would expect the mean posterior value to be closer to 2.15 $M_\odot$. Since the mass threshold is, until now, not expected to go beyound 2.7 $M_\odot$, we adopt $\mathcal{N}(2.35, 0.5)$ as the *a priori* in our analysis.

Table B.1 - Comparison of marginalized posterior distribution of m_{max} for different *a priori* distributions. The first column indicates the prior, the second is the mean value of marginalized parameter, the third column is the standard deviation and the fourth and fifth indicate the highest probability density which can be seen as an interval of the most likely values.

a priori	mean	sd	HPD 3%	HPD 97%
$\mathcal{N}(2.15, 0.5)$	2.495	0.356	1.855	3.128
$\mathcal{N}(2.25, 0.5)$	2.551	0.368	1.896	3.237
$\mathcal{N}(2.35, 0.5)$	2.597	0.381	1.913	3.303
$\mathcal{N}(2.45, 0.5)$	2.672	0.390	1.947	3.379
$\mathcal{N}(2.55, 0.5)$	2.727	0.398	2.022	3.501
$\mathcal{N}(2.65, 0.5)$	2.793	0.412	2.029	3.553

Appendix C

Mass inferences

As we discussed in Sections 3.1 and 3.3.2.4, with exception of systems where strong relativistic effects are present, determine the mass of pulsars can be a challenging task. In cases where the companion is optically bright, geometrical constraints can be set, that helps to infer the mass, but they can still be subject to systematic errors. The orbital inclination angle is the most sensitive parameter and exerts a large influence in the inference of pulsar mass.

The work of Alsing et al. (2018) and Shao et al. (2020) constructed likelihood functions describe by equations 3.30 and 3.31 to sample the individual pulsar mass for sytems where only the total mass or the mass ratio are provided, in addition to the mass function. The main assumption in their modelling is to consider the orbital inclination angle to assume any value between $0° - 90°$. Four of these systems were expected from observations to have masses above 2 $M_\odot$, and in Sec. 3.3.2.4 we checked the impact they have on the marginal distribution of m_{max}.

In the following we described how the observations lead to mass values we listed in Table 3.6, so we can see how the mass sampled in their model is inconsistent with observations.

C.1 PSR B1957+20

A Black-Widow system. Light curve analysis of the companion results in a radial-velocity amplitude of $K_2 = 353 \pm 4$ km s^{-1} that combined with the pulsar's mass function gives a minimum companion mass of $m_{c,min} = 0.022\ M_\odot$. The mass ratio and inclination angle best fits are $q = 69.2 \pm 0.8$ and $i = 65^o \pm 2^o$, and combined gives a best-fit pulsar mass of $m = 2.40 \pm 0.12\ M_\odot$ (Van Kerkwijk et al., 2011). Although light curve modeling

relies in a few assumptions, a lower limit to the pulsar mass is found to be 1.66 $M_\odot$.

C.2 PSR J1311-3430

Until recently this black-widow system had a light-curve based mass of $m = 2.63^{+0.3}_{-0.2}\ M_\odot$ (Romani et al., 2012), but constraints on i were poor. Kandel and Romani (2022) presents an analyisis of heating models for the light curve, from where they derive NS masses. Their preferred model results in $i = 68.7° \pm 2.1°$. With a radial velocity amplitude of $K_2 = 641.2 \pm 3.6$ and a companion mass of $m_c = 0.012 \pm 0.006$, the pulsar mass is inferred to be $m = 2.22 \pm 0.10$.

C.3 PSR B1516+02B

Placed in the globular cluster NGC 5904 with a companion that is either a WD or a low-mass MS star. The binary system has a mass of $2.29 \pm 0.17\ M_\odot$ and leads to a pulsar best-fit in $m = 2.08 \pm 0.19\ M_\odot$ (Freire et al., 2008). There is a 90% probability that the pulsar is more massive than 1.82 $M_\odot$, and a 0.77% probability that the inclination angle is low enough for m to fall between $1.20 - 1.44\ M_\odot$.

C.4 PSR J1748-2021B

Massive binary system with $m_t = 2.92 \pm 0.20\ M_\odot$ obtained from a precise $\dot{\omega}$ and assuming it is fully relativistic (Freire et al., 2008). The probability that the pulsar mass lies between 1.20 and 1.44 $M_\odot$ is only 0.10%, requiring a very low orbital inclination. The median mass of companion star is at 0.142 with lower and upper 1σ limits at 0.124 and 0.228 $M_\odot$, respectively, indicating that it can be a WD or an unevolved MS star and implies a pulsar mass of 2.74 $M_\odot$.

Appendix D

Orbital properties of DNS systems

Properties of 27 DNS systems including unconfirmed candidates, and 2 GW events from the mergers of DNS's

Pulsar	Type	P (ms)	$\dot{P}$ (10^{-18})	P_b (days)	e	f ($M_\odot$)	M_{tot} ($M_\odot$)	M_p ($M_\odot$)	M_c ($M_\odot$)	$\mathcal{M}$	δ (deg)	χ_f	χ_{eff}	τ_{gw} (Gyr)
J0453+1559	recycled	45.8	0.18616	4.072	0.113	0.1960	2.734(4)	1.559(5)	1.174(4)	1.1754	-	0.0005	-	1453
J0509+3801	recycled	76.5	7.931	0.379	0.586	0.0642	2.805(3)	1.34(8)	1.46(8)	1.2174	-	0.0030	-	0.576
J0737-3039A	recycled	22.7	1.74	0.102	0.088	0.2910	2.587052(8)	1.338185(+12/-14)	1.248868(+13/-11)	1.1253	< 3.2	0.0185	0.0096	0.086
J0737-3039B	young	2773.5	880	-——-	-——-	0.356	-——-	1.248868(+13/-11)	1.338185(+12/-14)	-——-	130±1	0	-——-	-——-
J1018-1523	recycled	83.2	0.109	8.984	0.228	0.2381	2.3(3)	[1.4]	¿1.16	-	-	-	-	13620
J1325-6253	recycled	28.97	0.048	1.816	0.064	0.1415	2.57(6)	< 1.59	> 0.98	-	-	-	-	190
J1411+2551	recycled	62.5	0.0956	2.616	0.170	0.1224	2.538(22)	< 1.62	> 0.92	-	-	-	-	466
J1518+4904	recycled	40.9	0.0275	8.634	0.249	0.1160	2.7183(7)	< 1.42	> 1.29	-	-	-	-	9974
B1534+12	recycled	37.9	2.422622	0.421	0.274	0.3146	2.678463(4)	1.3330(2)	1.3455(2)	1.1659	27±3	0.0038	0.0017	2.734
J1753-2240	recycled	95.1	0.97	13.637	0.304	0.0343	-	[1.4]	> 0.49	-	-	-	-	28847
J1755-2550*	young	315.2	2433.7	9.696	0.089	0.0212	-	[1.3]	> 0.39	-	-	-	-	15917
J1756-2251	recycled	28.5	1.017502	0.320	0.181	0.2201	2.56999(6)	1.341(7)	1.230(7)	1.1178	< 34	0.0081	0.0042	1.656
J1757-1854	recycled	21.5	2.627335	0.184	0.606	0.3579	2.73295(9)	1.3406(5)	1.3922(5)	1.1893	-	0.0185	-	0.076
J1759+5036	recycled	176	0.243	2.043	0.308	0.0818	2.62(3)	< 1.79	> 0.84	-	-	-	-	181
J1811-1736	recycled	104.2	0.901	18.779	0.828	0.1281	2.57(10)	< 1.74	> 0.93	-	-	-	-	1863
J1829+2456	recycled	41	0.04944	1.176	0.139	0.2942	2.60551(19)	1.306(4)	1.299(4)	1.1339	-	0.0054	-	55
J1906+0746*	young	144.1	20280	0.166	0.085	0.1116	2.6134(3)	1.291(11)	1.322(11)	1.1373	-	0.0001	-	0.308
J1913+1102	recycled	27.3	0.15672	0.206	0.089	0.1363	2.8887(6)	1.62(3)	1.27(3)	1.2468		0.0151	-	0.470
B1913+16	recycled	59	8.8	0.323	0.617	0.1321	2.828378(7)	1.438(1)	1.390(1)	1.2307	18 ±6	0.0041	0.0020	0.301
J1930-1852	recycled	185.5	18.001	45.06	0.399	0.3469	2.59(4)	< 1.32	> 1.3	-	-	-	-	534482
J1946+2052	recycled	16.9	0.9	0.078	0.064	0.2682	2.50(4)	< 1.31	> 1.18	-	-	-	-	0.046
J0514-4002A*	GC	4.99	0.0007	18.785	0.888	0.1454	2.4730(6)	1.25(5)	1.22(5)	1.0750	-	0.0447	-	508
J1748-2021B*	GC	16.8	−0.32913	20.55	0.57	0.0002	2.92(15)	< 3.24	> 0.11	-	-	-	-	26907
J1807-2500B	GC	4.2	0.0823245	9.957	0.747	0.2620	2.57190(73)	1.3655(21)	1.2064(20)	1.1169	-	0.0033	-	1044
J1823-3021G	GC	6.1	−0.018	1.54	0.38	0.0123	2.65(7)	< 2.4	> 0.44	-	-	-	-	70
J1835-3259A	GC	3.9	−1244100	9.246	0.968	0.0233	-	[1.4]	> 0.76	1.0788	-	-	-	1.322
B2127+11C	GC	30.5	4.98789	0.335	0.681	0.1525	2.71279(13)	1.358(10)	1.354(10)	1.1805	-	0.0091	-	0.217
J2140-2311B	GC	12.99	−0.6	6.22	0.879	0.2067	2.53(8)	≥ 1.43	≤ 1.10	-	-	-	-	32
GW170817⋆	GW	-	-	-	-	-	2.73(+4/-1)	1.46(+12/-10)	1.27(9)	1.186(1)	-	-	0.00(+2/-1)	-
GW190425⋆	GW	-	-	-	-	-	3.3(+1/-1)	1.60 - 1.87	1.46 - 1.69	1.44(2)	-	-	0.012(1)	-

$\dot{P}$ values are not corrected for Shklovskii effect (Shklovskii, 1970).

⋆ Values obtained under low spin prior ($\chi_{eff} < 0.05$).

* DNS nature not confirmed - can be a WD+NS binary.

The maximum mass of neutron stars may be higher than expected: an inference from binary systems

L.S. Rocha,[1,*] R.R.A. Bachega,[1,†] J.E. Horvath,[1,‡] and P.H.R.S. Moraes[1]

[1] *Universidade de São Paulo (USP), Instituto de Astronomia, Geofísica e Ciências Atmosféricas, Rua do Matão 1226, Cidade Universitária, 05508-090 São Paulo, SP, Brazil*

We have analyzed in this work the updated sample of neutron star masses derived from the study of a variety of 96 binary systems containing at least one neutron star using Bayesian methods. After updating the multimodality of the distributions found in previous works, we determined the maximum mass implied by the sample using a robust truncation technique, with the result $m_{max} \sim 2.5 - 2.6\, M_\odot$. We have checked that this mass is actually consistent by generating synthetic data and employing a Posterior Predictive Check. A comparison with seven published m_{max} values inferred from the remnant of the NS-NS merger GW170817 was performed and the tension between the latter and the obtained m_{max} value quantified. Finally, we performed a Local Outlier Factor test and verified that the result for m_{max} encompasses the highest individual mass determinations with the possible exception of PSR J1748-2021B. The conclusion is that the whole distribution already points toward a high value of m_{max}, while several lower values derived from the NS-NS merger event are disfavored and incompatible with the higher binary system masses. A large m_{max} naturally accommodates the lower mass component of the event GW190814 as a neutron star.

I. INTRODUCTION

The upper limit of the mass of a neutron star (NS) is one of the biggest unsolved problems in Astrophysics. Within General Relativity, the solutions of the hydrostatic equilibrium Tolman-Oppenheimer-Volkoff equation reach a critical value $M_{\rm max}$ for the mass of such objects, above which the structure collapses. This value $M_{\rm max}$ depends on the equation of state describing the matter inside the star [1, 2], although effects such as rotation [3, 4] and anisotropy [5] can increase the mass value. Rhoades and Ruffini [6] established an "absolute" upper limit of $M_{\rm max} = 3.2\ M_\odot$ without the necessity of introducing the real equation of state, although ignoring effects of rotation and exotic behavior [7].

Observational information would help to shed light on the composition issue [8, 9], but after 50 years of the discovery of pulsars the actual value of M_{max} is still subject to discussion. Recent fundamental advances in observational techniques, namely the detection of gravitational wave (GW) mergers in which at least one member is a NS and accurate timing detecting the Shapiro delay among the most important, have improved the situation to a point in which the issue can be studied thoroughly.

Statistical analysis of the observed mass distribution of NSs has been employed over the years to address its features [10–13]. More recently, the application of Markov Chain Monte Carlo (MCMC) methods [14] to analyze the distributions became viable and common. Previous studies have concluded that an unique evolutionary channel to form these compact objects is heavily disfavored, since observed mass distribution shows a high variation that cannot be accommodated by a single scale [15–17], although the lack of a firm conclusion about the preference of two or more scales is still present [18, 19] and the maximum mass still undetermined.

An additional source became possible with the detection of GWs emitted by the merger of two NSs, accompanied by electromagnetic counterparts [20]. Since the detailed dynamics of coalescence depends on the behavior of matter [21], a connection of the observations with M_{max} was worked out (see below). The recent detection of the event GW190814 [22] led to considerable discussion on the maximum mass due to the fact that the smaller component with $\sim 2.6\ M_\odot$ falls in the "gap" between observed NSs and black holes. If confirmed as a NS it would require a $M_{\rm max} \gtrsim 2.5\ M_\odot$, while the analysis of GW170817 remnant was consistent with a lower $M_{\rm max}$ [23]. In the present article, we perform an extended analysis of the mass distribution of observed NSs in binary systems, using advanced statistic techniques like MCMC and related tools, to extract information about the maximum mass parameter and confront our results with the inferences obtained by several groups on the maximum mass through the observation of GW signal observed from the GW170817 event, using the Posterior Predictive Check (PPC) method [24]. As a complementary analysis, we look for anomalous mass points (or *outliers*) in NS sample, which may not belong to the distribution, using the Local Outlier Factor (LOF) algorithm [25]. The purpose of the later is to check if the evidence in the existence of very massive NSs is statistically robust. We elaborate on these analysis below.

In the following we name as $m_{\rm max}$ the value derived from the distribution, i.e., a statistical inferred value, while the value M_{max} is a physical threshold, which ultimately would coincide with the former for a large sample if properly analyzed.

*Electronic address: livia.silva.rocha@usp.br
†Electronic address: rrhavia@if.usp.br
‡Electronic address: foton@iag.usp.br

International Journal of Modern Physics D
Vol. 29, No. 7 (2020) 2050044 (17 pages)

DOI: 10.1142/S0218271820500443

Exact solutions for compact stars with CFL quark matter

L. S. Rocha*, A. Bernardo*, M. G. B. De Avellar†,‡
and J. E. Horvath*,§

*Instituto de Astronomia, Geofísica e Ciências Amosféricas
Universidade de São Paulo, São Paulo - SP 05508-090, Brazil

†Instituto Tecnológico da Aeronáutica
Praça Marechal Eduardo Gomes, 50 – Vila das Acácias
São José dos Campos – SP 12228-900, Brazil

‡Universidade Federal de São Paulo
Unidade José Alencar – Rua São Nicolau
210 – Centro – 09913-030 – Diadema SP, Brazil
§foton@iag.usp.br

Received 16 January 2020
Revised 1 March 2020
Accepted 13 March 2020
Published 8 June 2020

The search for the true ground state of the dense matter remains open since Bodmer, Terazawa and others raised the possibility of stable quark matter, boosted by Witten's *strange matter* hypothesis in 1984. Within this proposal, the strange matter is assumed to be composed of *strange* quarks in addition to the usual *up*s and *down*s, having an energy per baryon lower than the strangeless counterpart, and even lower than that of nuclear matter. In this sense, neutron stars should actually be strange stars. Later work showed that a paired, symmetric in flavor, color-flavor locked (CFL) state would be preferred to the one without any pairing for a wide range of the parameters (gap Δ, strange quark mass m_s and bag constant B). We use an approximate, yet very accurate, CFL equation-of-state (EoS) that generalizes the MIT bag model to obtain two families of exact solutions for the static Einstein Field Equations (EFE) constructing families of anisotropic compact relativistic objects. In this fashion, we provide exact useful solutions directly connected with microphysics.

Keywords: Strange stars; exact solutions; compact objects.

1. Introduction

Immediately after Einstein's General Relativity Theory was published, Karl Schwarzschild managed to obtain the first exact solution of Einstein's field equations. The number of different exact solutions (with various applications) has been